
Adaptive shaping of laser beams for high-harmonic generation applications

Benjamin Heath

College of Science
Department of Physics

Primary supervisor
Dr Kevin O'Keeffe



**Prifysgol Abertawe
Swansea University**

Submitted on the 8th of August 2022 for the fulfilment of the
requirements for the Degree of Doctor of Philosophy in Physics

Declaration

This work has not previously been accepted in substance for any degree and is not being concurrently submitted in candidature for any degree.

Signed:  Dated: 08/08/2022

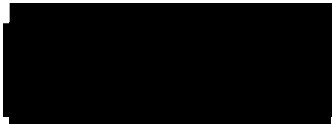
This thesis is the result of my own investigations, except where otherwise stated. Other sources are acknowledged by footnotes giving explicit references. A bibliography is appended.

Signed:  Dated: 08/08/2022

I hereby give consent for my thesis, if accepted, to be available for photocopying and for inter-library loan, and for the title and summary to be made available to outside organisations.

Signed:  Dated: 08/08/2022

The University's ethical procedures have been followed and, where appropriate, that ethical approval has been granted.

Signed:  Dated: 08/08/2022

Abstract

This thesis explores the use of adaptive optics to create tailored laser profiles to drive the process of high-order harmonic generation (HHG).

A deformable mirror controlled by a genetic, simulated-annealing algorithm (SA), and a genetic-annealing hybrid algorithm (HA) have been used to create super-Gaussian intensity profiles of orders ranging from $P = 1$ to $P = 2$ using a low-powered He-Ne laser. Between these three algorithms it was found that there is a compromise between the algorithm performance and reliability, and the algorithm complexity.

Simulated super-Gaussian beam-shaping with a phase-only SLM has been performed with a SA and HA algorithm and compared to a known π -shift method. The HA has shown an improvement in super-Gaussian quality for high orders, $P \approx 2.6$.

Simulations of HHG driven by super-Gaussian driver fields have been made using both the simple dipole model and the strong field approximation. It has been shown that HHG beam divergence decreases with increased order P . The fringe visibility has also been calculated as a measure of coherence.

Acknowledgements

I cannot give enough thanks for the guidance and patience of Dr Kevin O’Keeffe, and the adapted support he has given to me throughout the COVID epidemic.

I would also like to thank: Dr Adam Wyatt for his support and explanation of the codes for the strong field approximation, Dr Will Bryan for his enthusiastic support as my academic advisor, and for the insightful discussions with my second and third supervisors Dr Ken Meissner and Dr Emma Springate. Post-viva I give my additional thanks to the viva examination panel: Dr Amelle Zaïr, Dr James Bateman and Dr Sophie Schirmer.

Finally I would like to thank my personal and extensive support network for their continued encouragement over the last four (or more) years!

To my family,

Barbara Heath
Nina Mills
Sheila Lemon

Jayne Nemes
Dawn Mills
Sam Kelly

David Nemes
Colin Mills

the additional staff at Swansea who made the whole experience run smoothly,

Sara Fenn
Rhys Clements

Gill Oliver
Hugh Thomas

Carolyn Martin
Jon Woodman-Ralph

and my friends,

Adam Sayner
Cari Powell
Fr David Matthews
Huw Strachan
John Hunt
Matthew Pollard
Rebecca Hill
Siwan Evans

Alex Claymore
Connor Hayward
Elliot London
Jack Holligan
Karol Szuba-Jabonski
Owain Meredith
Robert Clayton
Tom La Vallin

Ashley Pellai
Curtis Jones
Gemma Cattermole
Joe Strong
Lynn Winterson
Phil John
Siddharth Pandey
William Murphy

with a special thanks to chaos personified, Sam Offler.

For Oliver Heath

The impact of COVID-19

Originally it was planned that a significant portion of the PhD would be spent developing beam shaping experiments at the Rutherford Appleton Laboratory. Experiments would have been tested at Swansea University before using the Artemis HHG beamline. This was prevented by the COVID-19 restrictions. As a compromise HHG simulations of experiments have been made instead in chapter 6.

Conference contribution

Photon 2020, Institute of Physics. Oral presentation: “Generation of super-Gaussian transverse laser profiles using a hybrid simulated annealing-genetic algorithm”, *Active and Adaptive Optics*.

Contents

Declaration	i
Abstract	ii
Acknowledgements	iii
The Impact of Covid-19	v
Conference proceeding	v
List of Figures	viii
List of Tables	xv
Abbreviations	xvii
1 Introduction	1
1.1 Ultrafast lasers	1
1.2 Beam shaping for high-powered lasers	5
1.3 Thesis overview and author contribution	8
2 Background content	9
2.1 Beam characterisation	9
2.1.1 Super-Gaussians	10
2.1.2 Image Moments	11
2.2 Beam propagation	11
2.2.1 Fresnel and Fraunhofer diffraction	12
2.2.2 The angular spectrum method	14
2.2.3 The Hankel transform	16
2.2.4 Propagation through a lens	18
2.3 Three-step model of high-harmonic generation	25
2.3.1 TSM introduction	25
2.3.2 Electron displacement	27
2.3.3 The cutoff energy	29
2.3.4 Long and short trajectories	30
2.3.5 Phase matching	31
3 Optimisation algorithms	33
3.1 The motivation to use optimisation algorithms	33
3.2 The genetic algorithm	35
3.2.1 Introduction	35
3.2.2 Fitness	37
3.2.3 Selection	38
3.2.4 Crossover	39

3.2.5	Mutation and evolutionary pressure	40
3.2.6	Elitism	41
3.3	The simulated annealing algorithm	42
3.3.1	Introduction	42
3.3.2	Acceptance probability	42
3.4	The hybrid algorithm	44
3.5	Test problem	44
3.5.1	Algorithm implementation	44
3.6	Results and discussion	46
4	Beam shaping with a deformable mirror	49
4.1	The deformable mirror	49
4.2	Applications of deformable mirrors with optimisation algorithms . . .	52
4.3	Experimental setup	54
4.4	Genetic algorithm implementation	56
4.5	Simulated annealing algorithm implementation	60
4.5.1	Genetic simulated annealing hybrid implementation	60
4.6	Pre-optimised beam profile	62
4.7	Algorithm results	62
4.7.1	Transverse beam profiles	62
4.7.2	Achieved orders and algorithm robustness	65
4.7.3	Algorithm convergence and run-time	67
4.7.4	Hybrid algorithm runtime improvement	69
4.8	Discussion	70
5	Beam shaping with a spatial light modulator	71
5.1	The spatial light modulator	71
5.2	Beam steering and shaping with a single SLM	72
5.3	Spatial light modulators for HHG	74
5.4	SLM simulation setup	75
5.4.1	π -shift shaping method	75
5.4.2	Algorithm shaping method	76
5.5	SLM shaping results	80
5.6	Other SLM shaping considerations	81
5.7	Dual element adaptive optics	82
5.7.1	Dual deformable mirrors	82
5.7.2	One deformable mirror and one spatial light modulator	82
5.7.3	Dual spatial light modulators	83
5.7.4	Dual element shaping with a Gerchberg Saxton algorithm	83

6	Driving HHG with tailored fields	86
6.1	The Lewenstein model of HHG	86
6.1.1	Ionization	89
6.1.2	Propagation	89
6.1.3	Recombination	91
6.1.4	HHG spectra	91
6.1.5	SFA benchmarking	92
6.2	The simple dipole model	93
6.3	HHG model beamline	95
6.4	Beam shaping for HHG	97
6.4.1	Calculating divergence using the SFA and SDM	98
6.4.2	Dual adaptive optics for HHG	102
6.4.3	Spatial coherence and fringe visibility	102
6.5	Discussion	105
7	Conclusion	107
7.1	Summary of thesis	107
7.2	Results	107
7.3	Future work	108
	Appendix	110
A1:	Zernike polynomials	110
A2:	Stationary phase approximation	112
	Bibliography	114

List of Figures

1.1	“Historical progress of the ultrashort pulse technology. E_L : laser electric field; V_{atom} : atomic potential; MPI: multiphoton ionisation; REMPI: resonance enhanced multiphoton ionisation; LOPT: lowest-order perturbation theory; SFA: strong field approximation; and E_{IR} : electric field of the infrared (IR) laser at the moment of ionisation t_i ”. Figure from [15].	4
2.1	Super-Gaussian distributions for $P = 1, 2, 3$	10
2.2	Diagram of propagation from an initial plane (x, y) at point P_1 to point P_2 with plane coordinates (p, q) separated by distance z	12
2.3	Visualisation of the angular spectrum of plane waves between fields $U(x, y, 0)$ and $U(x, y, z)$	14
2.4	a) The transverse intensity profile of a super-Gaussian (blue, $p = 2$) with a random phase profile (green, $\phi \propto r^{0.3}$) at $z = 0$. b) Propagated beam about $z = 0$ using the 1D Hankel transform and the 2D angular spectrum method.	18
2.5	Propagation between the back and front focal plane of a lens.	18
2.6	Phase and group velocities of a propagating wave.	20
2.7	Geometry of light passing through a lens with spherical surfaces, R_1 and R_2 , and thickness, d . Refractive indices are n_1 outside and n_2 inside the lens. $S_{o,i}$ denote object and image distances relative to surfaces R_1 and R_2	22
2.8	Geometry to calculate the propagation time $T(r)$ of a plane wave from A to focal point F.	22
2.9	a) Pulse and wave front behaviour behind a lens of radius $r = 40$ mm, focal length 150 mm, refractive index $n = 1.50799$, $\lambda(dn/d\lambda) = -0.1375$ for wavelength $\lambda = 249$ nm. b) Pulse and wave front behaviour about the focal plane at $x = 0$. The propagation time difference, 4.81 ps, before the focus shows a loop structure where the pulse has partially passed through $x = 0$ while the remainder of the pulse lags behind [62].	24
2.10	A Gaussian driver IR field (red) generates high-harmonics (blue) in a thin gas target.	25

2.11	A laser field (blue) distorts the atomic potential (green) such that the electron can undergo tunnel ionisation (magenta). The electron (yellow) then propagates in the continuum (red) until it recombines with its parent ion (black), releasing an XUV photon (dashed black).	26
2.12	Ionisation regimes defined by the Keldysh parameter, γ . The atomic Coulomb potential is shown in green, the electron in yellow, and I_p denotes the ionisation potential. a) illustrates multi-photon ionisation for $\gamma \gg 1$, b) illustrates tunnel ionisation for $\gamma < 1$ and c) illustrates over-the-barrier ionisation for $\gamma \ll 1$ [70].	27
2.13	Classical electron trajectories for different ionisation (birth) times within the electric field as described by equation 2.3.7. Long trajectory paths are in blue, short trajectory paths are in green, the cutoff trajectory is in magenta, and electrons that cannot return to their parent ion are in orange.	28
2.14	Kinetic energy of an electron on re-collision with their parent ion plotted against the birth and recombination times as separated by the dashed line. The long and short trajectory components are in blue and green respectively.	30
2.15	Phase accumulated by an electron in the continuum between birth and recombination times, T_b and T_r . [21, 33].	31
3.1	a) $y = x^2$, a simple function. b) $y = x \sin(x)$, a function with multiple local maxima. c) a more complicated function with a multi-dimensional search space as generated by the Matlab ‘peaks’ function.	34
3.2	Genetic algorithm terminology example for a 1D function.	36
3.3	Genetic algorithm flow chart. Yellow boxes indicate the start and end of the algorithm. Green boxes indicate GA processes. Blue boxes indicate all other processes. White boxes indicate decisions.	37
3.4	Visual representation of the roulette wheel selection method. A random number is chosen between 0 and the total sum of every individual’s fitness, $\sum f_N$. The individual corresponding to the interval of the random number is chosen to survive.	39
3.5	Illustration of crossover schemes, represented by 8-bit chromosomes for: a) single-point crossover, b) double-point crossover, and c) uniform crossover.	40
3.6	8-bit single loci mutation example.	41
3.7	Simulated annealing flow chart. Yellow boxes indicate the start and end of the algorithm. Green boxes indicate SA processes. Blue box indicates non-SA process. White boxes indicate decisions.	43

3.8	1D test function with many local maxima. The search space index is over a 12-bit binary range. The zoomed in portion of the function between the global maxima and 2 nd maxima have been highlighted in the green box.	45
3.9	Global (blue) and global or 2 nd maxima (green) found by the random search, genetic, simulated-annealing and hybrid algorithms after 10 000 runs at 1500 iterations per run.	47
3.10	Fitness values over 1500 iterations of the random search, genetic, simulated annealing and hybrid algorithms.	48
4.1	Cross-section illustrated examples of two deformable mirror architectures. a) a flexible membrane deformable mirror, b) a segmented deformable mirror. Actuators (black) are moved by their coupled coils (yellow) to manipulate the mirror surface (magenta).	50
4.2	ALPAO DM69 square-actuator layout. Aperture diameter, D = 10.5 mm. DM specification is stated in table 4.1.	51
4.3	Schematic of shaping beamline, including the He-Ne laser, neutral-density filters (ND), a telescope-lens pair (TLP), deformable mirror (DM), ×10 objective, and a CCD camera mounted to a computer-controlled translation stage. The angle of incidence of the beam onto the DM was $\approx 3^\circ$	55
4.4	Power transmission through an iris as a function of iris diameter. The integrated signal at each iris position was the average taken over 50 camera exposures. The resulting signal errors were small and not visible within this figure. The beam diameter extracted from the fit was (6.12 ± 0.12) mm.	55
4.5	Contour plots of the 2D fitting process. a) the large static ROI. The location of the first moment is shown in magenta. b) the small ROI centred on the first moment. c) a 2D Gaussian fit. d) the 2D Gaussian fit from c) overlapping the data from b).	56
4.6	Flow chart of the genetic algorithm used to perform spatial shaping of a laser. Yellow boxes indicate the start and end of the algorithm. Green boxes indicate algorithm processes. Blue boxes indicates non-algorithm processes. White boxes indicate decisions.	59
4.7	Flow chart of the simulated annealing algorithm used to perform spatial shaping of a laser. Yellow boxes indicate the start and end of the algorithm. Green boxes indicate algorithm processes. Blue boxes indicates non-algorithm processes. White boxes indicate decisions.	61

4.8	Pre-optimised transverse beam profiles from a He-Ne, on 200×200 pixel grids. a) beam profile. b) \log_{10} scale beam profile.	62
4.9	Amplitudes of Zernike modes at the back focal plane of a focusing lens before optimisation (blue), then after a genetic (green), simulated annealing (magenta) and hybrid algorithm (yellow), as well as a static flat mirror (red), for a target $P = 1$ Gaussian profile. Piston, tip, and tilt modes are not displayed.	63
4.10	Super-Gaussian transverse profiles achieved with a genetic (GA), simulated annealing (SA), and a hybrid algorithm (HA), using a deformable mirror. P denotes the target order. Image size of 200×200 pixels. Columns a, c, and f show the normalised CCD images, with data lineouts along the X and Y first moments in red and lineouts along the same location from the 2D fitted super-Gaussian profiles in white. Columns b, d and e show the CCD images on a log scale to highlight the scattered light outside the beam centre.	64
4.11	Super-Gaussian orders, intensity maintained within beam centre, and widths and amplitudes measured from three runs of the GA, HA and SA.	66
4.12	Convergence rates of the best result found over 1000 iterations for the GA, SA and HA, for super-Gaussian orders $P = 1.1, 1.5, 1.9$	68
4.13	Runtime of the GA, SA, and HA, averaged over 100 iterations, sending identical initial surfaces to the deformable mirror per iteration. The HA performance for $T = 3$ and $T = 4$ per iteration are shown. The CCD capture time, 2D least-squares fitting time, and deformable mirror settling time are also included.	69
4.14	Super-Gaussian order, signal maintained within beam centre, and widths and amplitudes measured from three runs of the $T = 1, 2, 3, 4$ temperatures per iteration hybrid algorithm, for target order $P = 1.5$	69
5.1	Schematic illustration of the operating principle of a phase-only LC-SLM. The reflective pixels are coloured magenta, the liquid crystals are represented by black ovals, the transparent window is in light blue, and the incoming and outgoing beams are coloured green and dark blue respectively.	72
5.2	Illustration of a linear phase shift producing a tilt in the wave front equal to θ . The optical period, pixel width and path difference is given by L , p and d respectively.	73

5.3	Super-Gaussian generation from π -phase shifts. a) initial Gaussian in black, example phase shift shown in magenta. Intensity profiles at the detector plane for imprinted phase shift widths of $0.800 w_G$, $0.925 w_G$ and $1.400 w_G$ where w_G is the initial Gaussian width are shown in b), c) and d) respectively in green, with fitted super-Gaussian profiles in blue.	77
5.4	a) Fitted super-Gaussian orders with fitting errors. b) Beam intensity maintained within the beam centre.	78
5.5	a) Super-Gaussian target order from π -shift method in blue, SA achieved order in green, for multiple n -values. b) Fitness values for SA iterations for multiple n -values.	79
5.6	a) Gaussian profile in black, SA imprinted phase solution in magenta for a target super-Gaussian $P = 2.62$. b) Intensity profile at the detector plane in green with the fitted super-Gaussian in blue with fitted order $P = 2.26 \pm 0.09$, and phase profile in magenta. c) Super-Gaussian orders achieved by the SA, HA and π -shift method, plotted relative to the order from π -shift method.	80
5.7	a) Target intensity profile at the focus, $P = 2$, with a flat transverse phase. b) Back propagated field from the target to the SLM plane. Intensity profile in blue, phase profile in red. The magenta, cyan, green and black lines ("limits") outline the four regions where the beam will be truncated and propagated forwards to the focal plane. c) Fitted super-Gaussian orders and percentage of beam intensity within the focus ROI about the beam centre for each of the four truncated fields. d) Intensity profile at the focus for fields propagated between truncated limits 1 (magenta) and 4 (black).	81
5.8	Flowchart describing the Gerchberg-Saxton algorithm between two planes. The angular spectrum method (ASM) is used to propagate between these planes separated by $z = 500$ mm. Constraints are made by replacing the acquired with the target intensity profiles at each plane. The algorithm finishes after n iterations.	84
5.9	Dual element shaping results from a Gerchberg-Saxton (GS) algorithm. a) The input Gaussian and phase required at the first shaping element. b) The target and GS intensity profile at the second shaping element. c) The target intensity and phase at the focus. The GS field (green and blue) is propagated from the second shaping element with the GS intensity and the ideal phase.	85

6.1	Single atom HHG spectra calculated using the SFA for argon for multiple peak driver intensities, I_{\max} . The dotted lines show the cutoff energies calculated from the three step model and each spectrum has been vertically offset for clarity. The driver wavelength is 800 nm with a pulse duration of 40 fs FWHM.	92
6.2	a) Intensity-normalised far-field harmonic spectra calculated using the SFA. The peak intensity is $I_{\max} = 2 \times 10^{14} \text{ Wcm}^{-2}$, the Gaussian pulse width is 40 [fs] FWHM, the transverse IR driver is a Gaussian of waist size 120 μm , the driver wavelength is 800 nm, and the source-detector distance is 3 m. b) Results of the SFA from Catoire et al. for the same parameters [75].	93
6.3	Schematic of a typical harmonic beamline including an AO system. An IR driving pulse is shaped by an adaptive optics system and focused to a gas target where harmonics are generated. An aluminium foil only allows the XUV beam through to a grating. A detector such as a CCD then measures these harmonics further along the beamline.	96
6.4	An illustration of harmonic generation at the gas target for a single infinitesimal plane. The harmonic spectrum is simulated at the generation plane by calculating the dipole over the Gaussian pulse (green) in time, the transverse profile as a function of radial distance in space. The field is then propagated in the z -direction down the beamline.	96
6.5	Variation of the harmonic size with super-Gaussian order using the denominator in equation 6.2.6 from the simple dipole model. $q' = \sqrt[2P]{q_{\text{eff}}}$, $q'' = \frac{d}{d(2P)} \sqrt[2P]{q_{\text{eff}}}$ (with a peak at $P = 1.835$), and $q_{\text{eff}} = 6.99$	98
6.6	Intensity distribution at the far field for multiple driver beam super-Gaussian orders about $q = 23$ calculated from the SFA.	98
6.7	The second moments calculated from the simple dipole model (SDM) and the strong field approximation (SFA) at propagation distance $z = 3 \text{ m}$ from the source, for $q = 25$. The SDM fitting parameters can be found in table 6.2 and the driver beam parameters are given in table 6.1.	99
6.8	Second moments against harmonic order for super-Gaussian order $P = 1, 2, 3$, for a) the strong field approximation, and b) the simple dipole model. The driver beam parameters are given in table 6.1 and the propagation distance is 3 m. The cutoff harmonic is at $q = 33$	100

6.9	Log scale radial transverse intensity profile for harmonic $q = 23$ against super-Gaussian order, P , calculated from the simple dipole model (SDM). SDM parameters are given in table 6.2. a) long and short trajectory contributions, b) short trajectory only, c) long trajectory only. The intensity profiles have been normalised for each super-Gaussian order. The driver beam parameters are given in table 6.1 and the propagation distance is 3 m.	101
6.10	Radial transverse intensity profile for harmonic $q = 23$ against super-Gaussian order, P , calculated from the strong field approximation. The red dashed lines are the second moments from the long and short trajectory contributions from the simple dipole model (SDM), the black dashed lines are the Gaussian-equivalent beam size using equation 6.2.6, the magenta dashed lines are the second moments from the short-only trajectory contributions using the SDM.	101
6.11	Second moments for harmonics 21 through 43 using the ideal super-Gaussian, $P = 2$, and the field field generated by a Gerchberg-Saxton algorithm. Propagation distance from the generation plane is $z = 3$ m.	102
6.12	Fringe visibility against slit-slit distance for different super-Gaussian orders, P . a) and b) show the results for a single-shot exposure for $q = 23$ and $q = 27$ respectfully. c) and d) show the results for an exposure averaged over 10 laser shots at the detector plane for $q = 23$ and $q = 27$ respectfully.	106
7.1	Z_n^m Zernike polynomials up to the 5 th order. From [179].	111
7.2	Stationary phase approximation example for very slowly oscillating $g(x)$ and quickly oscillating $f(x)$. $d(f(x)g(x)) / d(x) \approx 0$ about $x = 0$. $f(x) = Re\{\exp[2\pi ix^2]\}$, $g(x) = \cos(x/5)$	113

List of Tables

1.1	Common laser types [10].	2
3.1	Genetic algorithm terminology.	36
3.2	Parameters of the genetic algorithm (GA), simulated annealing algorithm (SA) and hybrid algorithm (HA) for solving the 1D test function.	46
3.3	Summary of performance and complexity for the random search algorithm (RSA), genetic algorithm (GA), simulated annealing algorithm (SA) and hybrid algorithm (HA).	47
4.1	ALPAO DM69 Specifications.	51
4.2	Parameters used in genetic algorithm.	58
4.3	Beam shaping simulated annealing parameters.	60
5.1	SLM simulated annealing (SA) and hybrid algorithm (HA) parameters. Some SA parameters as used by Fayyaz et al. [116].	78
6.1	HHG simulation parameters [165, 173].	96
6.2	Simple dipole estimated parameters.	99
7.1	Common names for Zernike modes.	111

Abbreviations

AO	Adaptive optic
ASM	Angular spectrum method
CCD	Charge-coupled device
CPA	Chirped pulse amplification
CW	Continuous wave
DM	Deformable mirror
XUV	Extreme ultraviolet
\mathcal{F}	Fourier transform
FWHM	Full width half maximum
GA	Genetic algorithm
GS	Gerchberg-Saxton
HT	Hankel transform
He-Ne	Helium-Neon
HHG	High-order harmonic generation
IR	Infrared
MCF	Mutual coherence function
ND	Neutral-density
OT	Optical tweezer
PSO	Particle-swarm optimisation
PSF	Point-spread function
\Re	Real
ROI	Region of interest
SA	Simulated-annealing algorithm
SLM	Spatial light modulator
STORM	Stochastic Optical Reconstruction Microscopy
SFA	Strong field approximation
TSM	Three step model
TDSE	Time dependent Schödinger equation
Ti:Sa	Titanium-sapphire
WFS	Wavefront sensor

Chapter 1

Introduction

"Try not to think too much about it."

Joe Strong

In this thesis beam shaping techniques for applications to high-order harmonic generation (HHG) are investigated. In chapter 6 simulations have been made of HHG driven by super-Gaussian laser profiles of increasing order, and it is shown that increasing this order decreases the HHG beam divergence. Practically this means that smaller volumes of interest could be irradiated and with a higher brightness. The HHG process produces an extreme ultraviolet beam with pulses on the attosecond timescale. This introduction starts with a brief overview of the technology leading up to and including HHG, followed by an overview of beam shaping techniques for high powered laser systems.

1.1 Ultrafast lasers

The laser is arguably one of the greatest technological achievements. In a non-exhaustive list modern laser technology has allowed for: high precision materials processing and micromachining [1], fast motion tracking and remote sensing methods (lidar) [2], precision length measurements, image and bar-code scanning, data storage [3], medical techniques such as cornea correction [4], and advances in both macroscopic and subatomic research [5]. In the current era it is hard to imagine life without laser devices. For this reason it may be surprising to learn that the first

Table 1.1: Common laser types [10].

Laser (continuous wave)	Medium	λ (nm)	Power
HeCd	Gas	325	<100 mW
Kr ion	Gas	531	0.1 - 10 W
HeNe	Gas	633	100 mW
Dye	Liquid	400 - 500	1 - 100 W
GaAIAs	Semiconductor	780	1 - 100 W
Nd:YAG	Solid state	1064	100 W
CO ₂	Gas	10600	100 W
Laser (pulsed)	Medium	λ (nm)	Pulse duration
Excimer KrCl	Gas	222	250 ns
Excimer XeF	Gas	351	1 - 30 ns
Ruby	Solid state	694	20 ns - 1 ms
Alexandrite	Solid state	720 - 800	0.1 ms
GaAS	Semiconductor	904	15 fs
Ti:sapphire	Solid state	700 - 1000	10 - 100 fs
Er:YAG	Solid state	2940	10 ns

laser demonstration was initially rejected for publication in May 1960 [6–8]. In the initial paper by Theodore Maiman, a high-powered flash lamp was shone on a silver coated ruby rod to create a substantial amplification of light. Despite the initial rejection Maimans’ report was accepted by Nature in the August of the same year. At that time the applications of lasers were not yet realised. At present there are many varieties of laser devices commercially available over a wide spectral range as displayed in table 1.1. To emphasise the scale and importance of laser applicability an article from 2017 stated that the ‘photonics technology produced in the United Kingdom contributes £12.9 billion to the country’s economy annually’ [9].

In science it is often required to observe and measure objects or systems of interest as they evolve over time to provide a deeper understanding of how nature behaves and to predict the outcome of future events. The required temporal resolution of measurements is problem dependent. In 1878 a debate was raised as to whether a running horse was ever completely aloft [11]. This debate arose because the human

eye has a perception rate of around 60 events per second which is not enough to definitively answer this question. The added difficulty was that the best commercial cameras at the time could only develop a single image on the order of minutes. The solution demonstrated by Eadweard Muybridge was to align 12 cameras that were triggered to each take a single image over a fraction of a second. After development the filmstrip of images showed the dynamics of the running horse with all four legs clearly off the ground [12]. The forefront of fast imaging has since moved on and one current area of interest in science is to probe the dynamics of molecular and sub-atomic systems where sub-nanometer spatial and sub-femtosecond temporal resolutions are required.

One way to probe the dynamics of small structures is through the use of pulsed laser systems. The first breakthrough into sub-nanosecond pulses was demonstrated in the 1960s by Hellwarth and McClung using a Q-switching technique which utilised electrically switched Kerr cell shutters in a ruby laser [13]. Q-switching is achieved by putting a variable attenuator inside the optical resonator. When this attenuator is functioning light leaving the gain medium does not return, which prevents lasing but allows energy to accumulate in the gain medium. Switching off the attenuator releases an intense light pulse, and then this process is repeated [14]. Typical pulses that can be produced only by Q-switching are on the order of 10s of nanoseconds. Q-switching paved the way for science in the non-linear light-matter interaction regime [15].

Following Q-switching techniques, mode-locking was introduced where a fixed phase relationship is induced between the longitudinal modes of the resonant cavity. If these modes are correctly in phase the output from the laser is typically zero except for a short pulse where constructive interference occurs [16]. The train of pulses are generated on the order of 100s of femtoseconds [13, 17, 18]. To amplify short pulses in the non-linear intensity regime the use of chirped pulse amplification (CPA) is required to avoid damage to the medium used to amplify the laser. In CPA an ultra-short laser pulse is stretched temporally by a grating pair on the order of

10^{3-4} times its initial duration. The stretched pulse is then amplified before re-compression [19–23]. The advancements in pulse length over time is shown in figure 1.1.

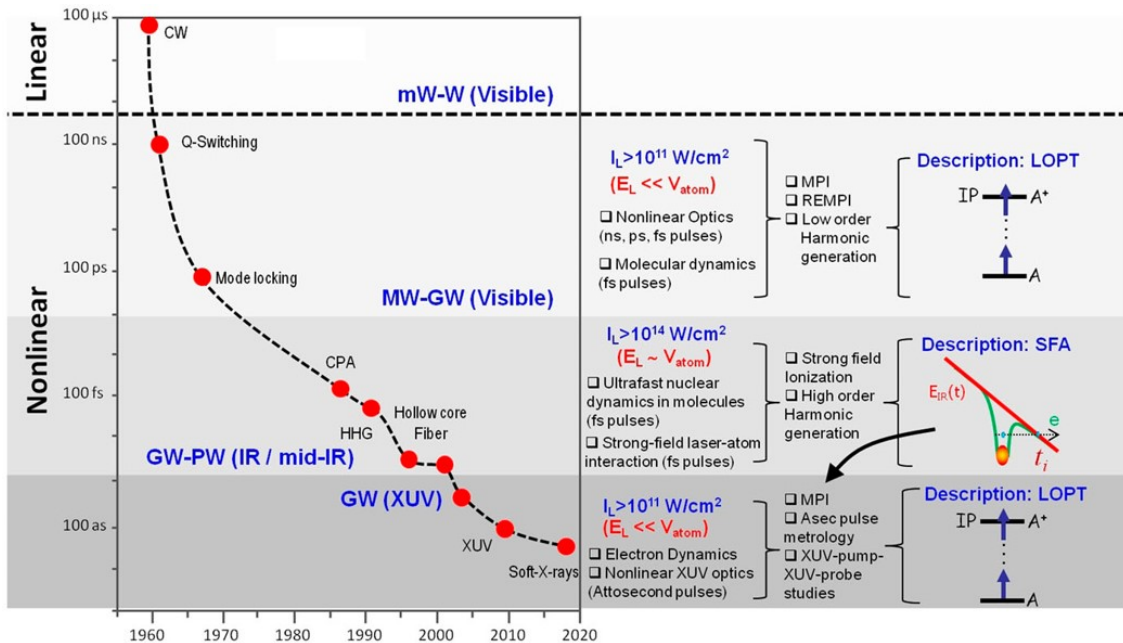


Figure 1.1: “Historical progress of the ultrashort pulse technology. E_L : laser electric field; V_{atom} : atomic potential; MPI: multiphoton ionisation; REMPI: resonance enhanced multiphoton ionisation; LOPT: lowest-order perturbation theory; SFA: strong field approximation; and E_{IR} : electric field of the infrared (IR) laser at the moment of ionisation t_i ”. Figure from [15].

Coherent sources of extreme-ultraviolet (XUV) radiation with pulses on the attosecond time scale are ideal for probing the dynamics of the molecular and sub-atomic scales [15, 24, 25]. Synchrotrons and free electron lasers (FELs) are excellent sources of incredibly bright XUV radiation, however the kilometre-scale size and build costs (in the millions or even billions of pounds) strictly limit access to these sites [3, 26]. At XUV wavelengths the difficulty to obtain lasing stems from the required pump power which scales with λ^{-4} [27]. Compact ‘table top’ sources of coherent XUV radiation offer an attractive alternative for many different types of experiments that can be performed at a relatively low spectral brightness [3]. High-order harmonic generation (HHG) is a relatively new technique in ultrafast optics which emerged in the late 1970s [28]. In a typical HHG setup an intense femtosecond titanium-sapphire laser is focused on to an atomic or molecular gas [8]. Prof. Paul

Corkum rationalised the HHG process with a three-step model where an electron is ionised in an intense laser field, it then propagates before recombining and releasing an XUV photon [29,30]. The HHG process occurs at the extremum of the oscillating driving field where electrons are liberated in ultra-short bunches much shorter than the optical period. A driver laser of wavelength 800 nm has an optical period of 2.7 fs, therefore the typical accelerated electron recombines and releases a photon after no more than a few hundred attoseconds [31,32].

One application of HHG is for diffractive imaging [26,33]. The smallest structure of size d that can be imaged is given by $d = K\lambda/A$, where K is a numerical constant that depends on the spatial coherence of the illumination of the object plane and A is the aperture of the optical system. The short wavelengths and high spatial coherence of HHG is therefore ideal for high resolution microscopy. The imaging of biological samples with HHG is of particular interest due to the K-shell absorption edges of oxygen and carbon at 2.3 nm and 4.4 nm respectively. Within this window water is transparent, which leads to contrast differences throughout different tissue types [26,33].

Another application of HHG is in ultrafast holography. In 2007 Tobey et al. demonstrated femtosecond time-resolved holography using the highly coherent XUV light generated by HHG [34]. Using interferometric imaging techniques this study used HHG XUV light to probe the femtosecond dynamics of electrons at a metal surface.

1.2 Beam shaping for high-powered lasers

In this section beam shaping techniques and applications are discussed. The motivation in this thesis is to tailor the driver beams for driving HHG.

The ability to manipulate the spatial or temporal structure of a laser beam has applications such as micromachining, fibre optics [35], and beam steering [36]. Using beam steering techniques ‘optical tweezing’ was the shared subject of the 2018 Nobel

prize [37–39]. This particular application is discussed further in section 5.2.

One of the most common applications of beam shaping is the removal of often undesirable spatial or temporal structures called aberrations. Aberrations present on a beam can reduce the overall beam quality and lower properties such as the maximum intensity. There are several ways to mathematically describe beam aberrations. Within this thesis the Zernike coefficients will be used as described in appendix A1. Common causes of aberrations include, but are not limited to, misalignment of optical components, the surface quality of optical components, thermal effects, turbulence in the propagating medium, doping inhomogeneities in amplifying crystals and non-linear effects [40].

Recent advancements in engineering have lead to the development of adaptive optics (AOs) which offer more versatility than static optics for tailored beam shaping. In this thesis beam shaping using a deformable mirror is investigated experimentally and its application to HHG investigated via a simulation.

An experiment from 2015 performed by Sun et al. combined two adaptive optics in to one optics system. Namely these were a deformable mirror (DM) and a spatial light modulator (SLM). Sun et al. demonstrated decoupled spatial and temporal control to compensate for effects such as propagation time difference (PTD) where there is slippage between slippage between pulse-fronts and wavefronts of a pulsed beam through a medium [41]. This is discussed further in section 2.2.4.

Numerical methods such as learning algorithms are often used to control AO devices for beam shaping, such as in [40, 42–44] where deformable mirrors were used to either minimise beam aberrations or to shape Gaussian beams into super-Gaussian intensity profiles. At present there are hundreds of learning algorithms that can be used for numerical optimisation. One of the focuses of this thesis is to show the performance of beam shaping using AOs controlled by a genetic, and a simulated algorithm which are amongst the most common used to control AO devices, as well as a hybrid algorithm made by this author.

The high damage threshold of modern AOs such as reflective DMs make these

devices ideal for use in high powered laser systems. Many experiments now commonly use DMs to optimise the driving laser used HHG. Most of these experiments focus on removing Zernike aberrations to increase the maximum driver beam intensity [42, 45, 46]. Optimising HHG flux is of great interest due to the inefficiency of HHG which is on the order of 10^{-6} to 10^{-8} for photon energies in the range of 50 – 100 eV using typical titanium-sapphire lasers. In the keV range the efficiency drops to $\approx 10^{-15}$ [47]. Due to the non-linearity of HHG the process is extremely sensitive to changes in both the driver beam intensity and phase profile.

In HHG driver beam shaping can be applied to ensure as much of the transverse intensity profile is above the threshold for generating high-harmonics. If the power is increased to maintain the same maximum beam intensity this will increase the number of XUV sources, and therefore the XUV photon flux. This is of interest for applications such as diffractive imaging experiments. Super-Gaussians profiles could offer such sought-after properties. For a fixed width these profiles become more flat-top-like at the expense of lowering the maximum intensity of the beam. Super-Gaussians of order $1 < P < 2$ and width w in the form $I(r) \propto \exp[-2(r^2/w^2)^P]$ have been shown to be achievable using adaptive optics. This thesis builds on the work of [43, 44] to create super-Gaussians with a single DM to profiles of user-defined orders. In a recent experiment by Treacher et al. a single SLM was used to create a super-Gaussian profile for driving HHG to optimise for brightness [48]. Within this thesis a numerical simulation is made of this shaping method and compared with an SLM controlled by a learning algorithm to show what improvements may be possible experimentally.

A shaping experiment performed by Constant et al. used a two-optical-path (TOP) mirror to generate flattop beams profiles for HHG [49]. The disadvantage with this technique is that a TOP mirror cannot compensate for beam aberrations, and the user is limited to only one type of beam shaping. Work presented in this thesis is towards being able to use adaptive optics that can make arbitrary beam shapes for driving HHG.

1.3 Thesis overview and author contribution

This thesis comprises of two main themes: the creation of tailored transverse beam profiles using optimisation routines, and the simulation of HHG using such profiles.

Chapter 2 covers some of the basic concepts and tools used throughout the thesis. These include the definition of the super-Gaussian, imaging moments, beam propagation methods, and a classical model of high-order harmonic generation.

In chapter 3 the performance of multiple learning algorithms are compared for finding the maximum of a known one-dimensional function. This leads into chapter 4 where the generic, simulated-annealing, and hybrid algorithms are used experimentally to control a deformable mirror with the goal of shaping the Gaussian transverse profile of a helium-neon laser into super-Gaussians of orders, $P = 1$ through $P = 2$.

In chapter 5 beam shaping simulations are performed with a phase-only spatial light modulator (SLM). The performance of a learning algorithm to control the SLM is compared with a known π -shift method for super-Gaussian generation [49, 50].

In chapter 6 the effects of super-Gaussian spatial shaping on HHG are investigated through simulations using both the strong field approximation and the simple dipole model. Investigations have been made for harmonic beam divergence and fringe visibility.

All simulated and experimental learning algorithms were made in MATLAB[®] by this author. Experiments with the deformable mirror were performed by this author. The codes for the strong field approximation were created by Dr Adam Wyatt and adapted by this author as described in chapter 6 to use custom driver beam profiles.

Chapter 2

Background content

"What is the physics equivalent of an exorcism?" - This author

"Fixing it."

Jack Holligan

This chapter covers several topics and techniques used throughout this thesis, including the super-Gaussian definition and image moments. This chapter then leads in to beam propagation using the Fresnel, Fraunhofer, and angular spectrum method. A discussion is then made about the effects of a pulsed laser through a lens. Finally, the classical model of high-order harmonic generation is given which is expanded on in chapter 6 with beam shaping applications.

2.1 Beam characterisation

A recurring topic within this thesis is spatially shaping beams into transverse super-Gaussian profiles. The conventional definition of a super-Gaussian is given in section 2.1.1. This is used in the fitting routines of learning algorithms, and the creation of target transverse profiles in all other simulations. The learning algorithms will aim to optimise the shape of transverse laser profiles to match the target super-Gaussian orders.

The method of first moments is used to calculate the beam centroid in the shaping experiment with a single deformable mirror. The learning algorithms use the location of the beam centroid to create a small 2D region of interest to perform a super-Gaussian fit. The width of an arbitrary intensity profile can be calculated

using the second moment. The second moments are used to estimate HHG beam divergences in chapter 6.

2.1.1 Super-Gaussians

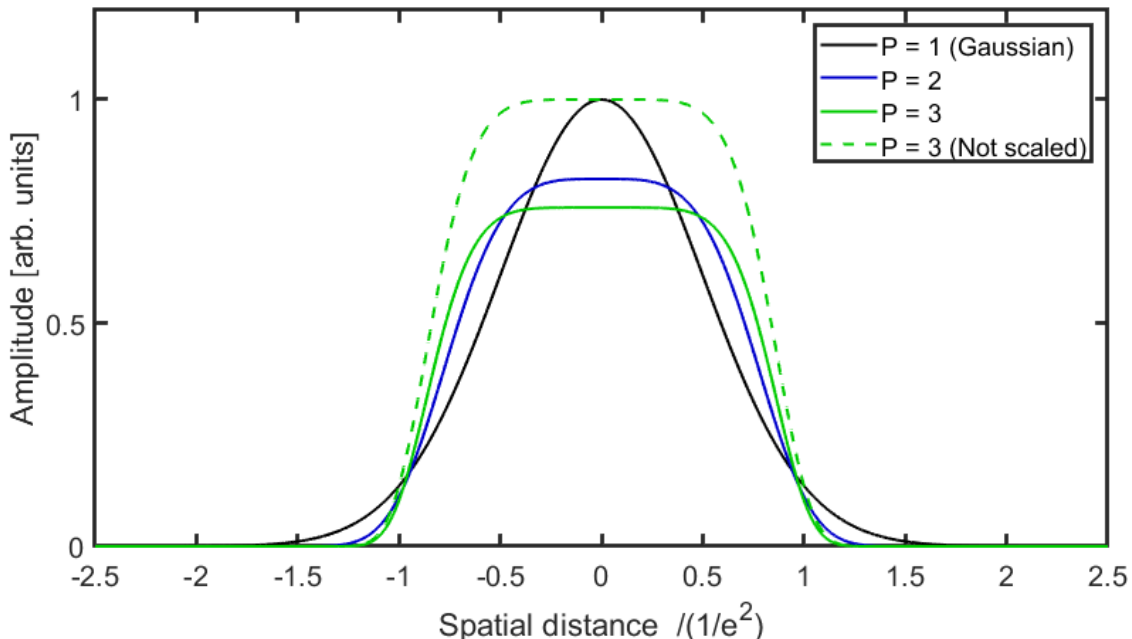


Figure 2.1: Super-Gaussian distributions for $P = 1, 2, 3$.

Super-Gaussians are higher order Gaussians where the region about the peak flattens as the order is increased. The shape of a super-Gaussian is given by [48, 51, 52],

$$G(r) = G_0 \exp \left[-2 \left(\frac{r^2}{w^2} \right)^P \right] + c, \quad (2.1.1)$$

where G_0 is the amplitude, r is the transverse position, w is the $1/e^2$ radius, $P > 1$ is the super-Gaussian order, and c is the vertical offset. For $P = 1$ equation 2.1.1 is reduced to a Gaussian profile. The amplitude scaling parameter, G_0 , is,

$$G_0(P, w) = \frac{(P/2) 2^{2/(P/2)}}{2\pi w^2 \Gamma(2/(P/2))}, \quad (2.1.2)$$

where the gamma function $\Gamma(z) = \int_0^\infty x^{z-1} \exp[-x] dx$, $\Re(z) > 0$. For higher super-Gaussian orders G_0 decreases for constant w to maintain the same integrated inten-

sity. Example profiles are shown in figure 2.1 for $P = 1, 2, 3$.

2.1.2 Image Moments

Given an image of pixels with intensity values, $I(x, y, z)$, the first moment is a measurement of the centre of gravity given by,

$$\langle x \rangle = \frac{\iint x I(x, y, z) dx dy}{\iint I(x, y, z) dx dy}. \quad (2.1.3)$$

This is also known as the expectation value of x or the location of the beam centroid.

Following this the beam variance is calculated by,

$$\sigma_x^2(z) = \frac{\iint (x - \langle x \rangle)^2 I(x, y, z) dx dy}{\iint I(x, y, z) dx dy}. \quad (2.1.4)$$

For any arbitrary beam the second moment can be used to measure the beam radius.

The second moment is given by,

$$W_x(z) \equiv 2\sigma_x(z). \quad (2.1.5)$$

The same treatment is made for $\langle y \rangle$, σ_y^2 , and W_y [53–57].

2.2 Beam propagation

For the purposes of modelling light it is necessary to be able to propagate fields between different planes [48, 58–60]. This section discusses multiple different methods of propagation. We start with Fresnel and Fraunhofer diffraction and build on these to introduce the angular spectrum method (ASM). The ASM is used in chapter 6 to propagate between two adaptive optic elements in the near-field. The Hankel transform is then described as it is a convenient alternative to the standard Fourier transform given that the HHG simulations in chapter 6 use cylindrical symmetry.

The Fourier transform property of a lens is then described as a way to propagate between the back and front-focal plane. This is used in chapters 5 and 6 to propagate between the adaptive optic element(s) and the focus of the driver beam.

Figure 2.2 shows an example geometry of propagation field $U(x, y)$ to $U(p, q)$ separated by distance z . The relationship between these planes from the Huygens-Fresnel principal is:

$$U(p, q) = \frac{z}{i\lambda} \iint U(x, y) \frac{\exp[ikr_{12}]}{r_{12}^2} dx dy, \quad (2.2.1)$$

where $k = 2\pi/\lambda$ is the wave number and the optical path length is,

$$r_{12} = \sqrt{z^2 + (p - x)^2 + (q - y)^2}. \quad (2.2.2)$$

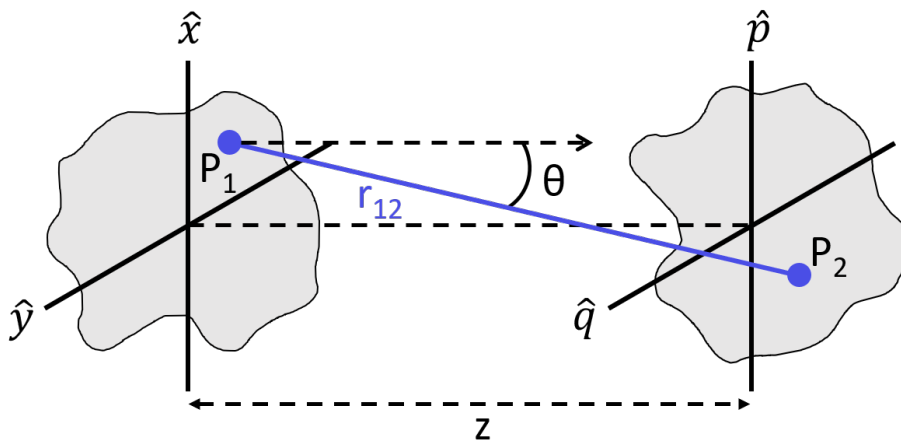


Figure 2.2: Diagram of propagation from an initial plane (x, y) at point P_1 to point P_2 with plane coordinates (p, q) separated by distance z .

2.2.1 Fresnel and Fraunhofer diffraction

The Fresnel number determines which of the Fresnel or Fraunhofer approximations can be suitably utilised and is defined as,

$$F = \frac{D^2}{z\lambda}, \quad (2.2.3)$$

where D is the aperture radius at the initial plane. In the near field $F \geq 1$ is in the Fresnel diffraction regime and in the far field $F \ll 1$ is in the Fraunhofer diffraction regime.

In the Fresnel regime only small angles are considered such that $z \approx r_{12}$. This approximation is not appropriate for r_{12} in the exponent as the exponent has a wavelength dependence. By factoring out z in equation 2.2.2 a binomial expansion can be performed such that,

$$r_{12} \approx z \left[1 + \frac{1}{2z} \left((p-x)^2 + (q-y)^2 \right) \right]. \quad (2.2.4)$$

Substituting 2.2.4 into 2.2.1 obtains,

$$U(p, q) = \frac{\exp[ikz]}{i\lambda z} \times \iint U(x, y) \exp \left[\frac{ik}{2z} \left((p-x)^2 + (q-y)^2 \right) \right] dx dy, \quad (2.2.5)$$

$$= \frac{\exp[ikz]}{i\lambda z} \exp \left[\frac{ik}{2z} (p^2 + q^2) \right] \iint \left(U(x, y) \exp \left[\frac{ik}{2z} (x^2 + y^2) \right] \right) \times \exp \left[-i \frac{k}{z} (xp + yq) \right] dx dy. \quad (2.2.6)$$

From equation 2.2.6 the Fresnel diffraction pattern is calculated by multiplying some pre-integral factors and the Fourier transform of $U(x, y)$ multiplied by a quadratic term. Using the definition of the Fourier transform,

$$G(x'') = \int g(x') \exp[-2\pi i f'_x x'] dx, \quad (2.2.7)$$

for spatial frequency $f'_{x'}$, the Fresnel approximation takes the form,

$$U(p, q) = \frac{\exp[ikz]}{i\lambda z} \exp \left[\frac{ik}{2z} (p^2 + q^2) \right] \mathcal{F} \left\{ U(x, y) \exp \left[\frac{ik}{2z} (x^2 + y^2) \right] \right\}. \quad (2.2.8)$$

In the Fraunhofer regime z is sufficiently large such that,

$$\frac{k}{2} (x^2 + y^2) \ll z, \quad (2.2.9)$$

Using 2.2.9 the quadratic factor in equation 2.2.2 is neglected. This yields the Fraunhofer approximation,

$$U(p, q) = \frac{\exp[ikz]}{i\lambda z} \exp\left[\frac{ik}{2z}(p^2 + q^2)\right] \mathcal{F}\{U(x, y)\}. \quad (2.2.10)$$

2.2.2 The angular spectrum method

An alternative to the Fresnel and Fraunhofer propagation method is the angular spectrum method (ASM) which can be used to propagate to both the near and far field. The ASM does not make the approximations from equations 2.2.4 and 2.2.9. A convenient property of the ASM is that the resolution between two planes are identical. However the drawback of this is aliasing due to under sampling. For sufficient sampling intervals $\Delta(x, y) \geq z\lambda/L_{(x,y)}$, where $L_{(x,y)}$ are the lengths of the 2D grid in directions x and y . Figure 2.3 displays a visualisation of this technique where the angular spectrum (a decomposition into multiple plane waves) is calculated at $U(x, y, 0)$. These plane waves are then each propagated z -distance away where the contributions from all plane waves are superimposed to find the total propagated field, $U(x, y, z)$.

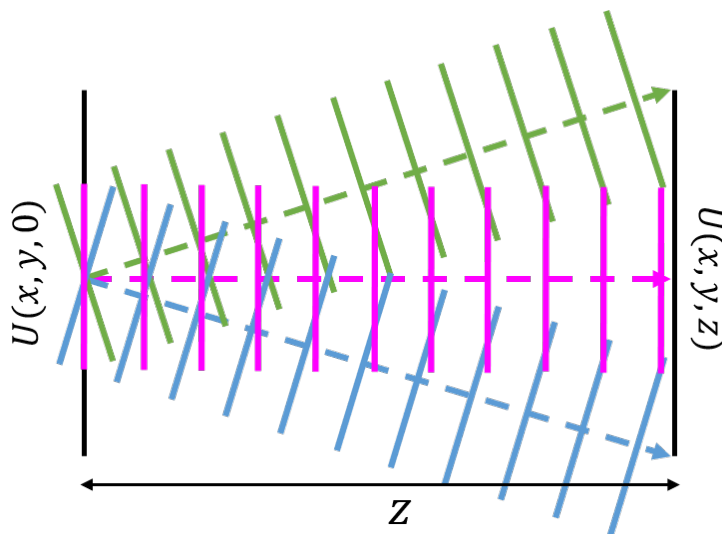


Figure 2.3: Visualisation of the angular spectrum of plane waves between fields $U(x, y, 0)$ and $U(x, y, z)$.

The initial plane $U(x, y, 0)$ can be written as a sum of plane waves U_p of the form,

$$U_p(x, y) = \exp[i\mathbf{k}\cdot\mathbf{r}], \quad (2.2.11)$$

$$= \exp[2\pi i(f_{px}x + f_{py}y)], \quad (2.2.12)$$

where $f_{p(x,y)}$ are spatial frequencies. It follows that,

$$U(x, y, 0) = \iint \hat{U}(f_x, f_y) \exp[(2\pi i(f_x x + f_y y))] df_x df_y. \quad (2.2.13)$$

The angular spectrum, $\hat{U}(f_x, f_y)$ is the Fourier transform of $U(x, y, 0)$ such that,

$$\hat{U}(f_x, f_y) = \frac{1}{2\pi} \iint U(x, y, 0) \exp[(-2\pi i(f_x x + f_y y))] dx dy. \quad (2.2.14)$$

Propagating in three dimensions,

$$\exp[i\mathbf{k}\cdot\mathbf{r}] = \exp[i(k_x x + k_y y + k_z z)], \quad (2.2.15)$$

$$|\mathbf{k}| = k = \sqrt{k_x^2 + k_y^2 + k_z^2}. \quad (2.2.16)$$

For spatial frequencies, $f_{(x,y)} = k_{(x,y)}/2\pi$, wave vector component k_z can be written as,

$$k_z = 2\pi \sqrt{\frac{1}{\lambda^2} - f_x^2 - f_y^2}. \quad (2.2.17)$$

For $z > 0$,

$$\exp[i\mathbf{k}\cdot\mathbf{r}] = \exp \left[2\pi i \left(f_x x + f_y y + z \sqrt{\frac{1}{\lambda^2} - f_x^2 - f_y^2} \right) \right], \quad (2.2.18)$$

Substituting equations 2.2.18 into 2.2.13 the ASM yields,

$$\begin{aligned} U(x, y, z) &= \iint \hat{U}(f_x, f_y) \\ &\times \exp \left[2\pi i \left(f_x x + f_y y + z \sqrt{\frac{1}{\lambda^2} - f_x^2 - f_y^2} \right) \right] df_x df_y, \end{aligned} \quad (2.2.19)$$

$$= \mathcal{F}^{-1} \left\{ \mathcal{F}\{(U, x, y, 0)\} \exp \left[2\pi i \left(f_x x + f_y y + z \sqrt{\frac{1}{\lambda^2} - f_x^2 - f_y^2} \right) \right] \right\} (x, y). \quad (2.2.20)$$

The ASM is also known as the double Fourier transform method due to the presence of the two transforms in equation 2.2.20.

2.2.3 The Hankel transform

Expanding on the angular spectrum method, if the field to be propagated is cylindrically symmetrical then it is convenient to apply a Hankel transform (HT) instead of a standard Fourier transform. Using a rectangular coordinate system the Fourier transform of an arbitrary electric field $\epsilon(x, y)$ is given by,

$$E(f_X, f_Y) = \iint_{-\infty}^{\infty} \epsilon(x, y) \exp[-i2\pi(f_X x + f_Y y)] dx dy. \quad (2.2.21)$$

To switch to a polar coordinate system the following variables are transformed such that,

$$\begin{aligned} x &= r \cos(\theta) & r &= \sqrt{x^2 + y^2} \\ y &= r \sin(\theta) & \theta &= \arctan(y/x) \\ f_X &= \rho \cos(\theta) & \rho &= \sqrt{f_X^2 + f_Y^2} \\ f_Y &= \rho \sin(\theta) & \phi &= \arctan(f_Y/f_X). \end{aligned} \quad (2.2.22)$$

If the electric field is cylindrically symmetric then the electric field can be written as a function that is only dependent on r such that,

$$\epsilon(r, \theta) = \epsilon'(r). \quad (2.2.23)$$

Substituting equations 2.2.22 and 2.2.23 in to 2.2.21 the Fourier transform is written as,

$$E'(\rho, \phi) = \int_0^{2\pi} d\theta \int_0^{\infty} \epsilon'(r) \exp[-i2\pi r \rho (\cos(\theta)\cos(\phi) + \sin(\theta)\sin(\phi))] r dr. \quad (2.2.24)$$

Here we can use the trigonometric identity,

$$\cos(\theta - \phi) = \cos(\theta)\cos(\phi) + \sin(\theta)\sin(\phi), \quad (2.2.25)$$

such that equation 2.2.24 becomes,

$$E'(\rho, \phi) = \int_0^{2\pi} d\theta \exp[-i2\pi r \rho (\cos(\theta - \phi))] \int_0^\infty \epsilon'(r) r dr. \quad (2.2.26)$$

In this form we can use the Bessel function identity,

$$J_0(a) = \frac{1}{2\pi} \int_0^{2\pi} \exp[-ia \cos(\theta - \phi)] d\theta, \quad (2.2.27)$$

where J_0 is the zeroth order Bessel function of the first kind. Further details are in appendix A2. Substituting this into equation 2.2.24 the dependence on ϕ disappears.

We are then left with,

$$E'(\rho, \phi) = E'(\rho) = 2\pi \int_0^\infty \epsilon'(r) J_0(2\pi r \rho) r dr, \quad (2.2.28)$$

which is the one dimensional HT [61]. The Hankel transform as denoted by H has analogous properties to the Fourier transform so it follows that,

$$g_R(r) = HH^{-1}(g_R(r)) = HH(g_R(r)) = H^{-1}H(g_R r). \quad (2.2.29)$$

Using the same treatment as above, the inverse HT is,

$$\epsilon'(r) = 2\pi \int_0^\infty E'(\rho) J_0(2\pi r \rho) \rho d\rho. \quad (2.2.30)$$

The ability to represent and propagate the electric field in one dimension is computationally advantageous as it removes the necessity to calculate over an $N \times N$ grid. The HT propagation tool was bench marked against a two dimensional angular spectrum and figure 2.4 shows that they are in good agreement.

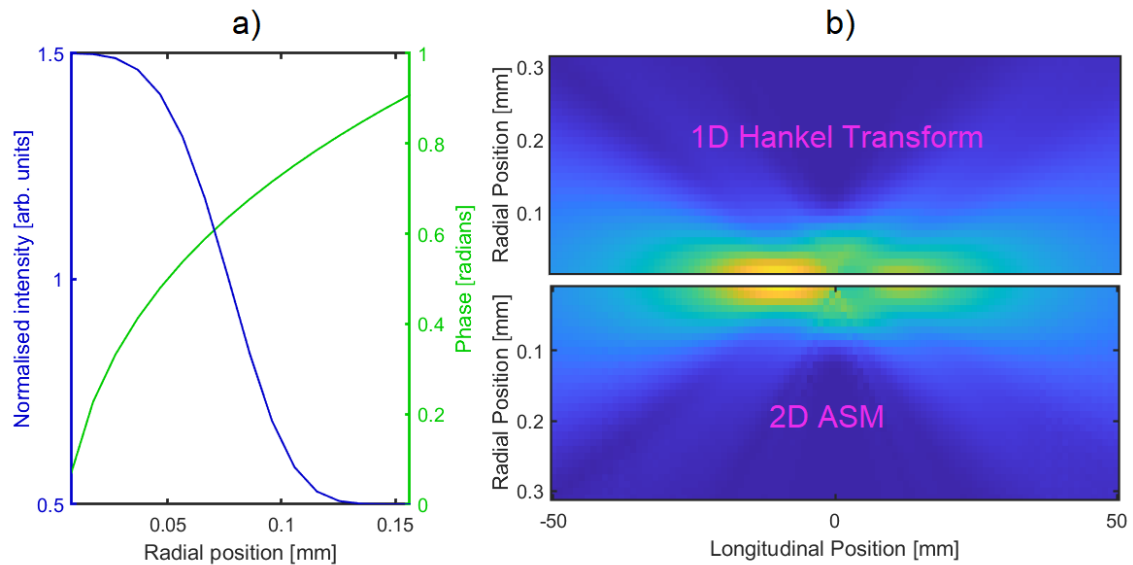


Figure 2.4: a) The transverse intensity profile of a super-Gaussian (blue, $p = 2$) with a random phase profile (green, $\phi \propto r^{0.3}$) at $z = 0$. b) Propagated beam about $z = 0$ using the 1D Hankel transform and the 2D angular spectrum method.

2.2.4 Propagation through a lens

The ideal thin lens

The geometry of a thin lens setup is displayed in figure 2.5. At $z = 0$ an initial field is multiplied by the quadratic phase function of the lens such that,

$$U_{\text{initial}} = U(x, y, 0) \exp \left[-\frac{ik}{2f}(x^2 + y^2) \right]. \quad (2.2.31)$$

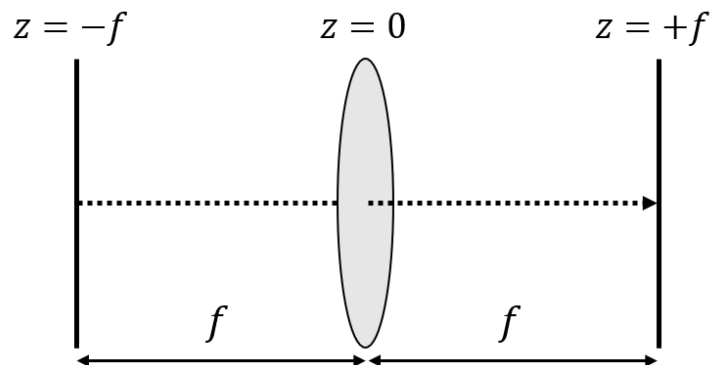


Figure 2.5: Propagation between the back and front focal plane of a lens.

Propagating using the Fresnel regime to plane $z = f$,

$$U(x, y, f) = \exp \left[\frac{ik}{2f}(x^2 + y^2) \right] \mathcal{F}\{U(x, y, 0)\} \left(\frac{x}{\lambda f}, \frac{y}{\lambda f} \right). \quad (2.2.32)$$

Using the ASM the relationship between the $z = -f$ and $U(x, y, 0)$ just before the lens is,

$$\begin{aligned} \mathcal{F}\{U(x, y, 0)\} \left(\frac{k_x}{2\pi}, \frac{k_y}{2\pi} \right) &= \mathcal{F}\{U(x, y, -f)\} \left(\frac{k_x}{2\pi}, \frac{k_y}{2\pi} \right) \exp \left[if \sqrt{k^2 - k_x^2 - k_y^2} \right], \\ \mathcal{F}\{U(x, y, 0)\} \left(\frac{k_x}{2\pi}, \frac{k_y}{2\pi} \right) &\approx \mathcal{F}\{U(x, y, -f)\} \left(\frac{k_x}{2\pi}, \frac{k_y}{2\pi} \right) \exp \left[-if \left(\frac{k_x^2 + k_y^2}{2k} \right) \right]. \end{aligned} \quad (2.2.33)$$

By substituting $k_x = 2\pi x/\lambda f = kx/f$ we obtain, 2.2.33,

$$\mathcal{F}\{U(x, y, 0)\} \left(\frac{x}{\lambda f}, \frac{y}{\lambda f} \right) = \mathcal{F}\{U(x, y, -f)\} \left(\frac{x}{\lambda f}, \frac{y}{\lambda f} \right) \exp \left[-\frac{ik}{2f}(x^2 + y^2) \right]. \quad (2.2.34)$$

From equations 2.2.32 and 2.2.34 the relationship between the front and back focal planes are an exact Fourier transform given by,

$$\mathcal{F}\{U(x, y, f)\} = \mathcal{F}\{U(x, y, -f)\} \left(\frac{x}{\lambda f}, \frac{y}{\lambda f} \right). \quad (2.2.35)$$

Pulsed beam through a lens

The pulsed driving beam for HHG can acquire phase front and wavefront distortions when propagating through a lens. This section describes the effect of the propagation time difference as a consequence of a pulsed laser propagating through a lens. In principle, adaptive optics can be used to correct for such effects.

The pulse and phase fronts of a pulsed laser propagate at the group, v_g , and phase, v_p , velocities respectively as shown in figure 2.6. These velocities are given

by,

$$v_g = \frac{c}{n - \left(\lambda \frac{dn}{d\lambda}\right)}, \quad (2.2.36)$$

$$v_p = \frac{c}{n}, \quad (2.2.37)$$

where n is the refractive index $n = c/v$ [62].

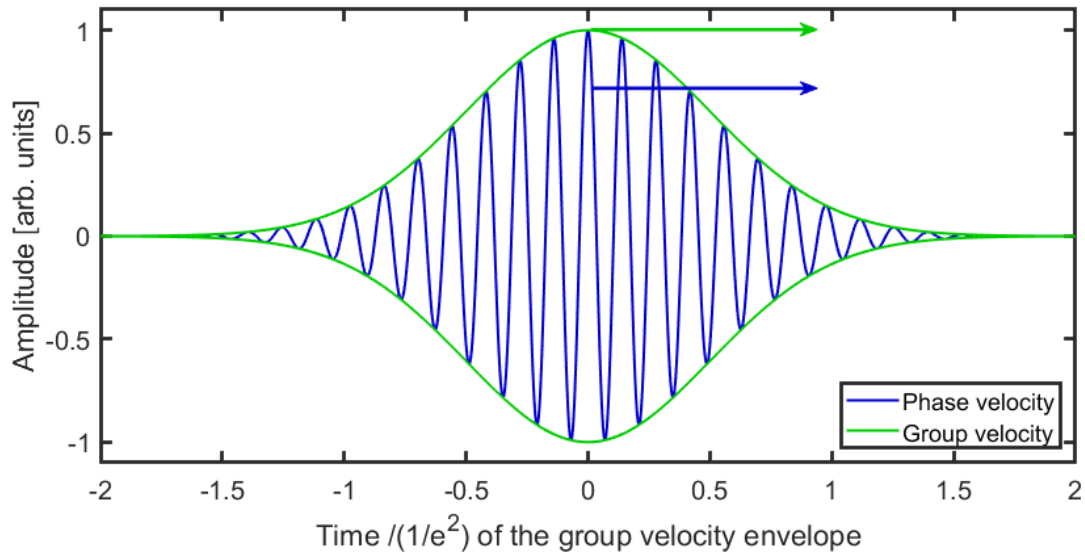


Figure 2.6: Phase and group velocities of a propagating wave.

Through a lens of thickness L the propagation time difference (PTD) is given by,

$$\text{PTD} = L \left(\frac{1}{v_p} - \frac{1}{v_g} \right), \quad (2.2.38)$$

$$= L \left(\frac{n}{c} - \frac{n}{c} \left(1 - \frac{\lambda}{n} \frac{dn}{d\lambda} \right) \right). \quad (2.2.39)$$

The PTD varies with the transverse variation of the thickness of the lens. Pulse broadening occurs due to group velocity dispersion (GVD) and is given by [62],

$$\text{GVD} = \frac{\lambda^3}{2\pi c^2} \frac{d^2 n}{d\lambda^2}. \quad (2.2.40)$$

From the geometry in figure 2.7,

$$\frac{n_1}{S_{i2}} + \frac{n_1}{S_{o1}} = (n_2 - n_1) \left(\frac{1}{R_1} - \frac{1}{R_2} \right) + \frac{n_2 d}{(S_{i1} + d)S_{i1}}, \quad (2.2.41)$$

where n_1 and n_2 are refractive indices outside and inside the lens, $R_{1,2}$ are the curvatures of the lens for each surface, $S_{i,o}$ are the image and object distances relative to lens surfaces 1 and 2, and d is the lens thickness. Using the thin lens approximation, $d \ll 1$ and setting the refractive index in air, $n_1 = 1$, Equation 2.2.41 reduces to Lensmaker's equation [63, 64],

$$\frac{1}{f} = (n_2 - 1) \left(\frac{1}{R_1} - \frac{1}{R_2} \right), \quad (2.2.42)$$

where f is the focal length. In order to calculate the propagation time $\Delta T(r)$ Fermat's principle is applied which is given by,

$$L_1 + nL_2 + L_3 + L_4 = n d_0 + f, \quad (2.2.43)$$

with lens thickness, d_0 , focal length, f , and the path lengths, $L_{1,4}$, are from the geometry shown in figure 2.8. The propagation time, $T(r)$, of a plane wave from A to F is calculated by,

$$T(r) = \frac{L_1 + L_3 + L_4}{c} + \frac{L_2}{c} \left(n - \lambda \frac{dn}{d\lambda} \right). \quad (2.2.44)$$

Using the paraxial approximation the expressions for d_0 and L_2 are,

$$d_0 = \frac{r_0^2}{2} \left(\frac{1}{R_1} + \frac{1}{R_2} \right), \quad (2.2.45)$$

and,

$$L_2 = \frac{r_0^2 - r^2}{2} \left(\frac{1}{R_1} + \frac{1}{R_2} \right), \quad (2.2.46)$$

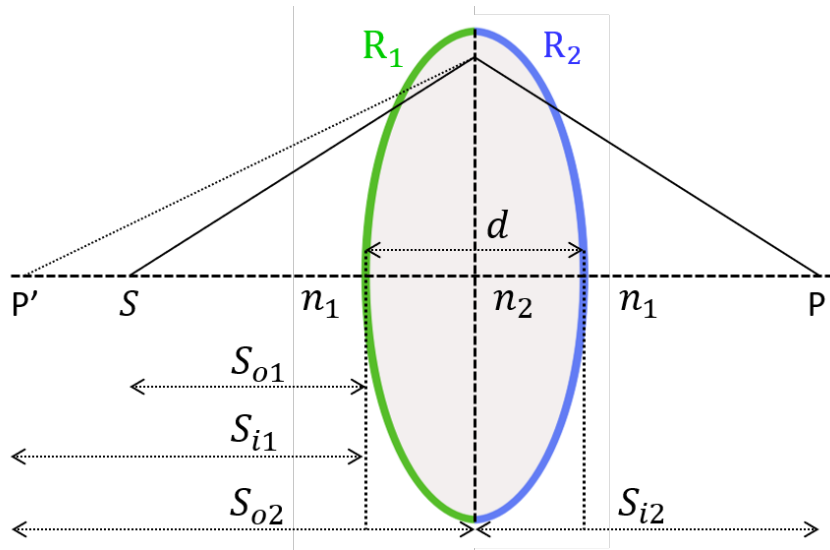


Figure 2.7: Geometry of light passing through a lens with spherical surfaces, R_1 and R_2 , and thickness, d . Refractive indices are n_1 outside and n_2 inside the lens. $S_{o,i}$ denote object and image distances relative to surfaces R_1 and R_2 .

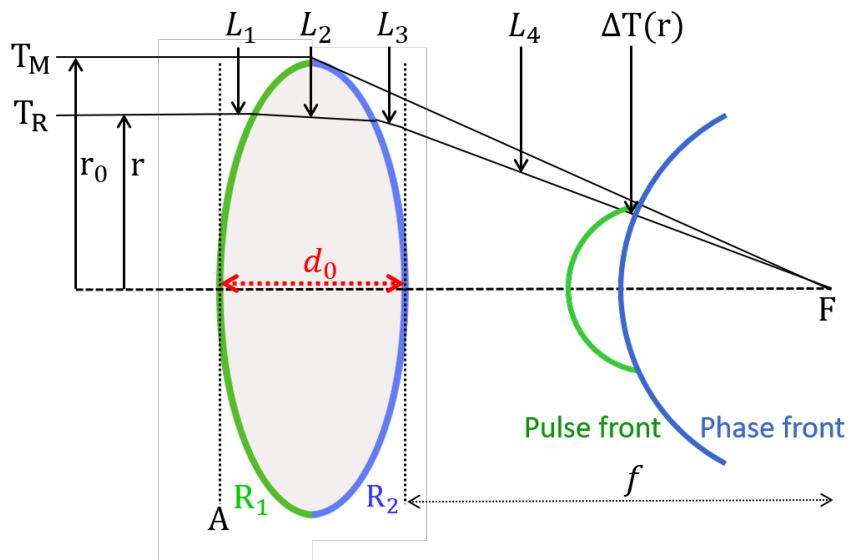


Figure 2.8: Geometry to calculate the propagation time $T(r)$ of a plane wave from A to focal point F .

where r and r_0 are the radii of the incident light rays [65]. Using equations 2.2.43 through 2.2.46 the propagation time becomes,

$$T(r) = \frac{f}{c} + \frac{d_0}{c} \left(n - \lambda \frac{dn}{d\lambda} \right) + \frac{r^2}{2c} \left(\frac{1}{R_1} + \frac{1}{R_2} \right) \lambda \frac{dn}{d\lambda}. \quad (2.2.47)$$

Using 2.2.45 and 2.2.47 the propagation time for the outermost ray from figure 2.8 is,

$$T_M \equiv T(r_0) = \frac{1}{c}(f + n d_0). \quad (2.2.48)$$

The delay between the phase and pulse fronts can be calculated from Lensmaker's equation 2.2.42 and equation 2.2.47,

$$\Delta T(r) \equiv T(r) - T_M = \frac{r_0^2 - r^2}{2cf(n-1)} \left(-\lambda \frac{dn}{d\lambda} \right). \quad (2.2.49)$$

The effect of the PTD is shown in figure 2.9 for pulse fronts and wavefronts about the focal plane at $t = 0$, where the pulse has been broadened by 4.81 ps. The pulse front equations of motion are given by,

$$x(t) = c(t - \Delta T(r)) \cos(\alpha), \quad (2.2.50)$$

$$y(t) = c(t - \Delta T(r)) \cos(\alpha), \quad (2.2.51)$$

$$(2.2.52)$$

where, $\alpha = \tan^{-1}(r/f)$ [62].

PTD effects can be removed using an achromat, however adaptive optics allows for both the removal of these effects and additional control over the pulse fronts and wave fronts.

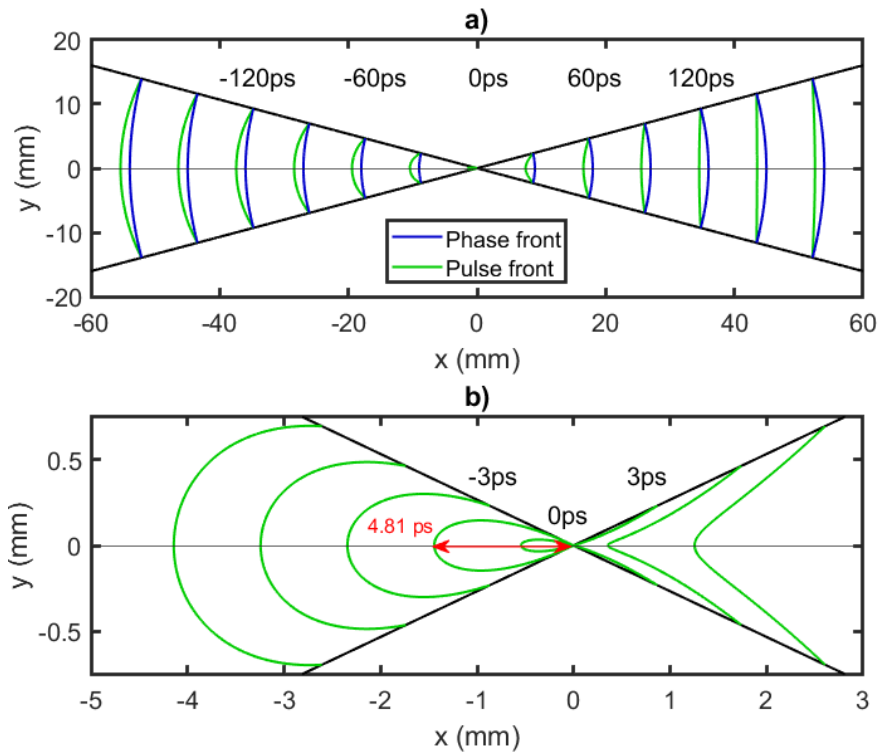


Figure 2.9: a) Pulse and wave front behaviour behind a lens of radius $r = 40$ mm, focal length 150 mm, refractive index $n = 1.50799$, $\lambda(dn/d\lambda) = -0.1375$ for wavelength $\lambda = 249$ nm. b) Pulse and wave front behaviour about the focal plane at $x = 0$. The propagation time difference, 4.81 ps, before the focus shows a loop structure where the pulse has partially passed through $x = 0$ while the remainder of the pulse lags behind [62].

In 2015 a beam shaping technique was developed by Sun et al. that allows for shaping in both the spatial and temporal domain [66]. In their dual-adaptive optic setup a deformable mirror (DM) is used to distort the pulse and phase fronts simultaneously. A spatial light modulator (SLM) is then used to cancel any phase front distortions, effectively demonstrating decoupled control of the pulse and phase fronts. This technique allows for the generation of spatially and temporally tailored beam profiles and the compensation of the PTD effects described in figure 2.9 on ultrafast pulses through a lens or distortions through other optical materials.

Within this thesis only spatial shaping is considered using a single and dual element approach for applications in high-order harmonic generation. Additionally, the propagation of a super-Gaussian beam with a flat-phase profile will generate a donut-shaped transverse intensity profile [60]. In this thesis all models assume that

the targets are located at the focus and are thin enough to neglect these propagation effects.

2.3 Three-step model of high-harmonic generation

High-harmonic generation (HHG) is a highly non-linear process that generates coherent extreme ultraviolet (XUV) radiation. Figure 2.10 illustrates an example of HHG where an infrared pulsed Gaussian driver field is focused onto a thin noble gas target where the typical laser intensities are of the order of $10^{14} \text{ W cm}^{-2}$. Within the gas target q^{th} harmonics are generated with frequencies $w_q = qw_0$, where q is an odd integer and w_0 is the fundamental frequency of the driving laser. Although a quantum model of HHG is given in chapter 6 this process can be understood by using a three-step (semi-classical) model (TSM) as interpreted in 1993 by Paul Corkum [29, 30].

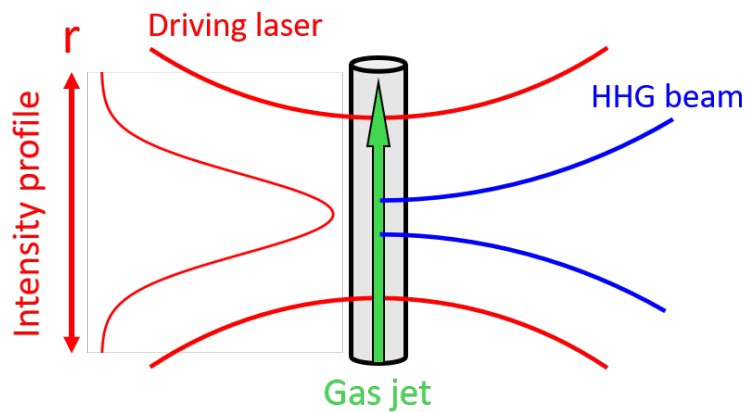


Figure 2.10: A Gaussian driver IR field (red) generates high-harmonics (blue) in a thin gas target.

2.3.1 TSM introduction

The TSM as illustrated in figure 2.11 follows these distinct steps [26, 48, 67]:

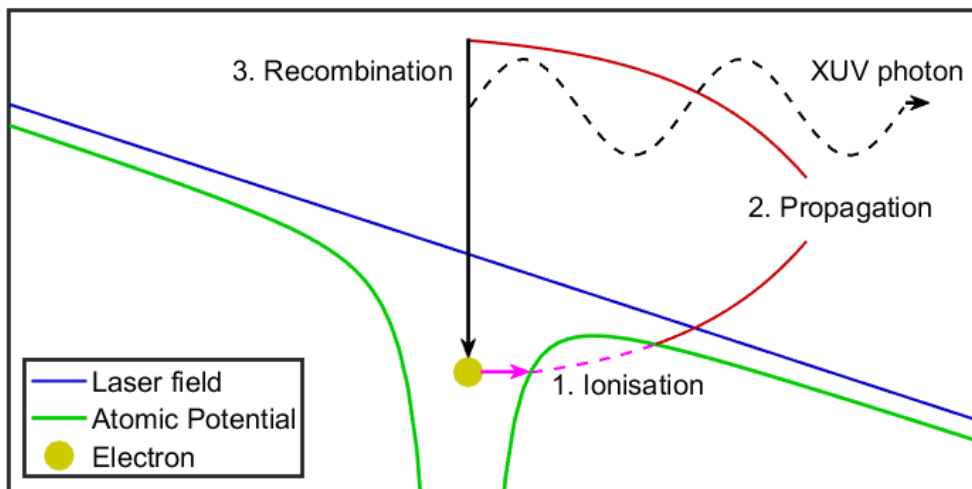


Figure 2.11: A laser field (blue) distorts the atomic potential (green) such that the electron can undergo tunnel ionisation (magenta). The electron (yellow) then propagates in the continuum (red) until it recombines with its parent ion (black), releasing an XUV photon (dashed black).

- 1) Ionisation. An electron is in an unperturbed ground state until it is instantly ionised at some point in the laser pulse.
- 2) Propagation. The electron enters the continuum at rest. As a free particle it is accelerated by and follows a trajectory determined by the oscillating electric field of the driving laser.
- 3) Recombination. The electron is accelerated back towards its parent ion where it re-collides and a harmonic photon is released. This photon has energy equivalent to the kinetic energy of the electron upon collision plus the ionisation energy.

The above steps are known as the birth, continuum and recombination times respectively denoted by, T_b , $T_r - T_b$, and T_r . The regimes of ionisation are determined by the adiabatic Keldysh parameter which is defined as,

$$\gamma = \frac{\omega_0}{e|E_0|} \sqrt{2I_p m_e}, \quad (2.3.1)$$

where ω_0 and $|E_0|$ are the frequency and magnitude of the electric field, e and m_e are the charge and mass of an electron and I_p is the ionisation potential [68, 69]. Figure 2.12 illustrates three regimes of ionisation defined by the Keldysh parameter.

Within this thesis calculations are made for the tunnel ionisation process.

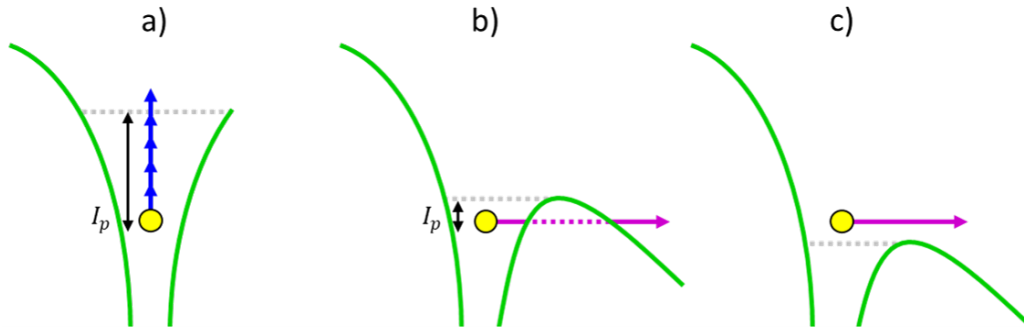


Figure 2.12: Ionisation regimes defined by the Keldysh parameter, γ . The atomic Coulomb potential is shown in green, the electron in yellow, and I_p denotes the ionisation potential. a) illustrates multi-photon ionisation for $\gamma \gg 1$, b) illustrates tunnel ionisation for $\gamma < 1$ and c) illustrates over-the-barrier ionisation for $\gamma \ll 1$ [70].

For tunnel ionisation to occur the atomic potential needs lowering to the point where the electron can pass through the potential barrier but not so low as to allow for it to be liberated over the barrier. This means that the electron is only liberated around the electric field extremum of the driving laser pulse. The ionisation time windows are larger for a slowly varying driving field when $\omega_0 \ll I_p$, implying that the tunnelling regime is dominant when $\gamma < 1$.

2.3.2 Electron displacement

In the TSM the electron trajectory in the continuum can be determined using classical physics. Starting with the real part of the sinusoidal driver field,

$$E(t) = E_0 \cos(\omega t), \quad (2.3.2)$$

where ω is the driver frequency. The force experienced by the ionised electron is,

$$F = eE_0 \cos(\omega t) = m_e \frac{d^2 x}{dt^2}. \quad (2.3.3)$$

Rearranging equation 2.3.3 into an expression for the velocity,

$$v = \frac{dx}{dt} = \frac{eE_0}{m_e} \int_{t_0}^t \cos(\omega t) dt, \quad (2.3.4)$$

$$= \frac{eE_0}{m_e \omega} (\sin(\omega t) - \sin(\omega t_0)), \quad (2.3.5)$$

where t_0 indicates the birth time at which the velocity is zero. By integrating once more the expression for the electron displacement is [26, 33, 69],

$$x(t, t_0) = \frac{eE_0}{m_e \omega} \int_{t_0}^t (\sin(\omega t) - \sin(\omega t_0)), \quad (2.3.6)$$

$$= \frac{eE_0}{m_e \omega^2} [\cos(\omega t_0) - \cos(\omega t) - (\omega t - \omega t_0) \sin(\omega t_0)]. \quad (2.3.7)$$

Electron displacements starting at multiple birth times are shown in figure 2.13 for time windows where the electron can and cannot classically return to their parent ion. The figure also shows that some electrons that can return but ‘miss’ the initial recombination window may recombine at later times, however this process is not examined further within this thesis.

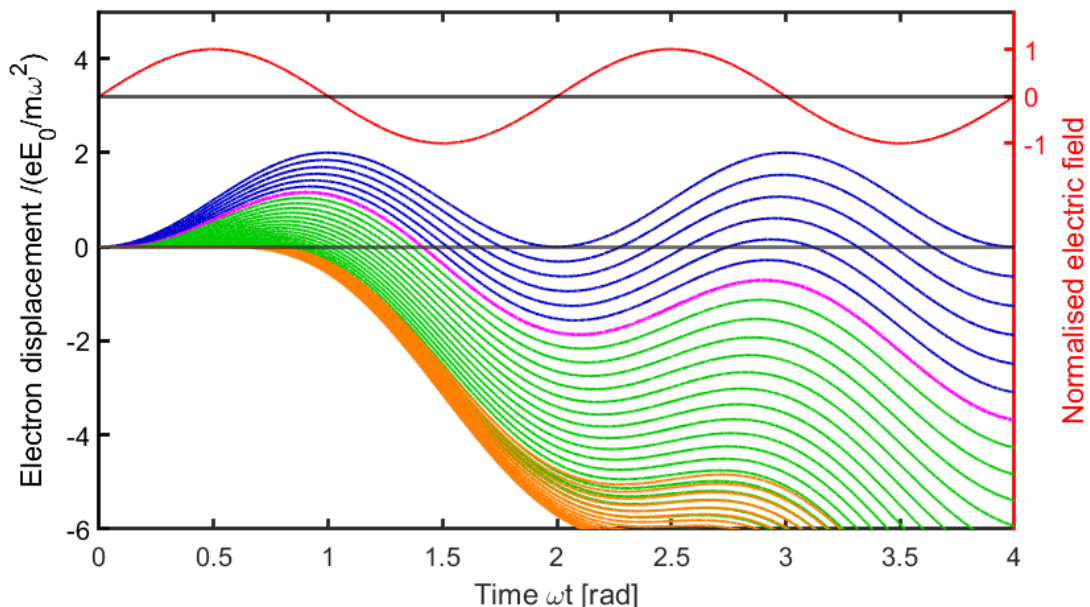


Figure 2.13: Classical electron trajectories for different ionisation (birth) times within the electric field as described by equation 2.3.7. Long trajectory paths are in blue, short trajectory paths are in green, the cutoff trajectory is in magenta, and electrons that cannot return to their parent ion are in orange.

2.3.3 The cutoff energy

The time averaged ponderomotive energy is defined as,

$$U_p = \frac{1}{2} m_e \omega^2 \langle x^2 \rangle. \quad (2.3.8)$$

For a sinusoidal displacement in x the time averaged value is the amplitude divided by $\sqrt{2}$. From equation 2.3.7, 2.3.8 becomes,

$$U_p = \frac{1}{2} m_e \omega^2 \left(\frac{e E_0}{\sqrt{2} m_e \omega} \right)^2, \quad (2.3.9)$$

$$= \frac{e^2 E_0^2}{4 m_e \omega^2} \propto I \lambda^2, \quad (2.3.10)$$

which states that the ponderomotive energy scales linearly with the maximum driver beam intensity and quadratically with the driver wavelength. Only considering electrons that return to their parent ion, the velocity and therefore the kinetic energy can be plotted as a function of time as shown in figure 2.14. Adding the contribution from the ground state energy I_p , the maximum energy of the photon emitted during recombination as a function of the ponderomotive and potential energy is, [21, 33, 47, 71–74],

$$E_{\max} = \hbar \omega_{\max} = 3.17 U_p + I_p. \quad (2.3.11)$$

This maximum energy corresponds to the cut-off energy of the HHG spectrum.

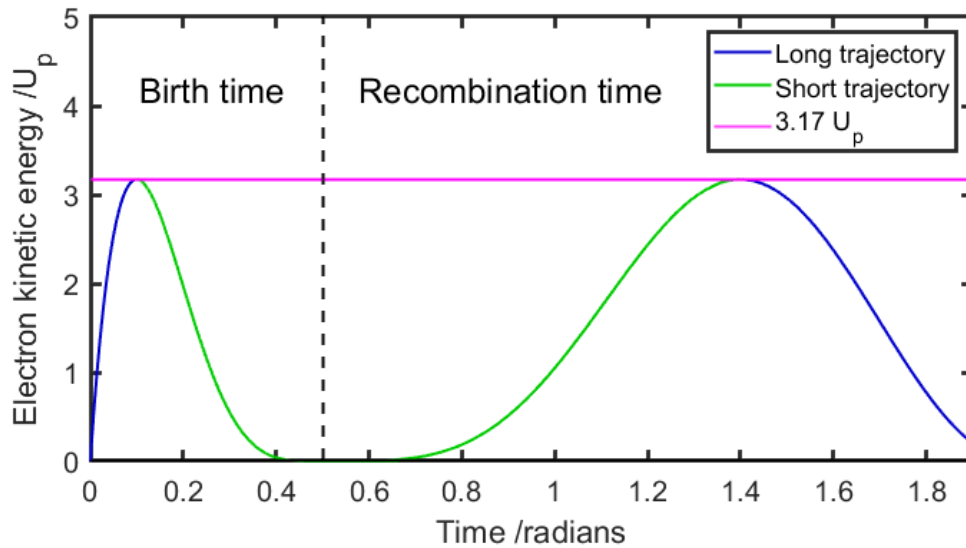


Figure 2.14: Kinetic energy of an electron on re-collision with their parent ion plotted against the birth and recombination times as separated by the dashed line. The long and short trajectory components are in blue and green respectively.

2.3.4 Long and short trajectories

At the maximum energy, $E = E_{max}$, from figure 2.14 there is only one trajectory that an electron can follow for a Gaussian driver beam. For any energy, $E < E_{max}$, there are two trajectories that can yield the same photon energy, namely the ‘long’ and ‘short’ paths as colour labelled in figure 2.14. These names reflect the different lengths of time that the electron spends in the continuum as shown in figure 2.15. For some applications an undesirable characteristic is the quantum interference of these trajectories which causes spectral modulations in the harmonic spectra [75]. One possible way to minimise these interference effects and maximise harmonic yield is to use a driver with a flat-top or super-Gaussian transverse intensity profile where more photons can be generated at $E = E_{max}$.

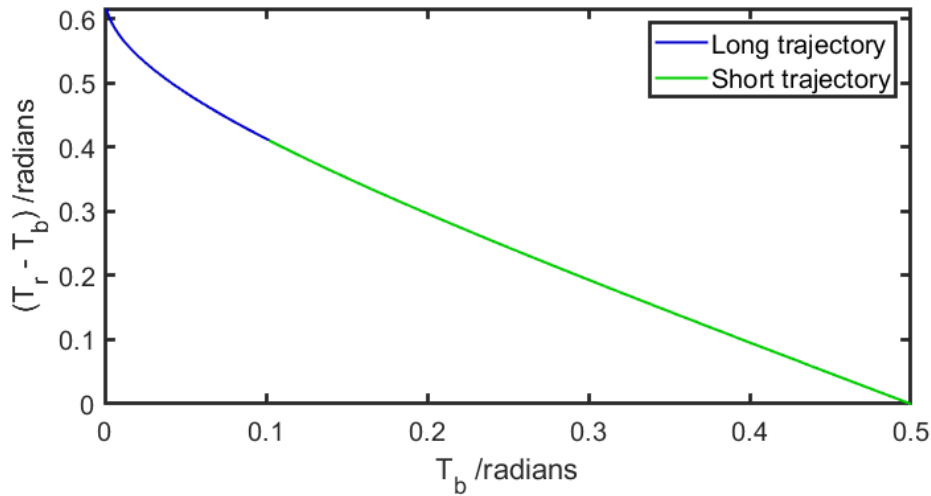


Figure 2.15: Phase accumulated by an electron in the continuum between birth and recombination times, T_b and T_r . [21, 33].

The quantum models of HHG are discussed further in chapter 6 with a study on the effects of tailored beam shaping.

2.3.5 Phase matching

The HHG process in practice takes place across a macroscopic medium such as the gas target in figure 2.10. The total harmonic field involves the propagation of both the driver and harmonic field generated at each position throughout the medium. Due to dispersion within this medium, the phase velocities for the fundamental and harmonic frequencies vary throughout the medium [26]. This leads to interference between the harmonic field contributions generated at different positions in the generating medium. In the absence of phase matching constructive interference, which leads to quadratic growth of the harmonic intensity with propagation distance, can only be achieved over a distance known as the coherence length which is given by,

$$L_c = \pi / \Delta k, \quad (2.3.12)$$

where Δk is the phase mismatch between the fundamental laser field and the generated harmonic. For distances larger than L_c destructive interference occurs, reducing the harmonic intensity. In practice phase-matching effects can be minimised by selecting suitably thin gas targets such that the thickness of the gas target $L_{\text{gas}} \ll L_c$ [76]. In this thesis HHG models assume a thin gas target of one atom thickness such that phase matching considerations are neglected.

Chapter 3

Optimisation algorithms

"You should include your enemies
in your acknowledgements too, for
stoking the flames."

Siddharth Pandey

In this chapter four different optimisation algorithms will be used to find the global maximum of a simple 1D function as displayed in figure 3.8. Namely, these algorithms are: a random search algorithm (RSA), a genetic algorithm (GA), a simulated annealing algorithm (SA), and a genetic-annealing hybrid algorithm (HA). These algorithms are later used in chapters 4 and 5 to control adaptive optics elements to shape laser profiles. The MATLAB ‘global optimisation toolbox’ contains a version of both a GA and SA. These were not used by this author as these in-built codes do not offer as much tailoring to the algorithm features, and they are not designed to solve for iterative processes as required in the laboratory as discussed in chapter 4.

3.1 The motivation to use optimisation algorithms

Consider the problem of finding the global maximum of the function $f(x) = x^2$ for integer values $0 \leq x \leq 1000$, as in figure 3.1a. Here, x represents a ‘search space’ of all possible solutions over which the optimisation algorithms can evaluate $f(x)$.

Starting with a simple RSA, this algorithm evaluates $f(x)$ at a random value of x over numerous iterations and outputs the best solution found. This type of algorithm is computationally fast as the only operation prior to evaluating $f(x)$ is the generation of a random number within the search space [77, 78]. The disadvantage

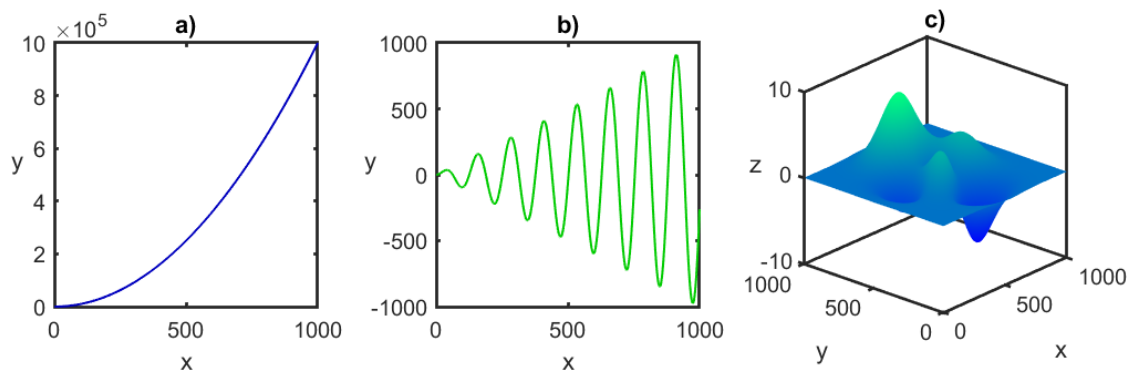


Figure 3.1: a) $y = x^2$, a simple function. b) $y = x \sin(x)$, a function with multiple local maxima. c) a more complicated function with a multi-dimensional search space as generated by the Matlab ‘peaks’ function.

with the RSA is that all of the information about the search space from previous iterations is not taken into account as x is randomly generated. This means that per iteration, the probability of finding the global maximum is inversely proportional to the size of the search space. An argument can be made that RSAs are the easiest to implement, but only adequate for quickly obtaining a better solution over relatively small search spaces. Improvements can be made by gradually constraining the search space around ‘good’ solutions as they are found, however there are a number of more sophisticated algorithms that can offer better reliability of finding the global maximum [79].

Gradient ascent, sometimes referred to as ‘hill climb’ algorithms evaluate the gradient of a function between $x_1 = x_{\text{initial}}$ and $x_2 = x_{\text{initial}} \pm \Delta x_{\text{initial}}$ (where x_{initial} for the first iteration is a random number within the search space), passing x_2 into the next iteration if the gradient is positive, or x_1 otherwise [80]. This approach is more robust, and converges much faster than the random search method. In the case of figure 3.1a, the average number of iterations needed to find the global maximum is half the size of the search space assuming $\Delta x_{\text{initial}}$ is ± 1 index in x . However, these algorithms are very sensitive to the initial conditions and are therefore susceptible to getting caught in local maxima of more complicated functions such as in figure 3.1b. To mitigate these problems, more complicated gradient ascent algorithms can iteratively optimise several random x_{initial} solutions and vary $\Delta x_{\text{initial}}$ (this is

called the ‘search-momentum’) values per iteration to escape local maxima [80]. The limitation of this kind of algorithm is realised when the functions become very complicated and the search spaces are very large and/or multidimensional such as in figure 3.1c. In this case, the number of starting locations necessary to converge on the global maximum can be computationally intensive, reducing the algorithm’s efficiency.

Machine learning (ML) or learning algorithms (LAs) are terms used to describe a range of computational algorithms that can be used to optimise a solution based on the search space information gained from previous iterations. Generally, these methods are both faster and more reliable than random searches. At present, LAs are a vast field of research in computer science and mathematics. Some popular methods include: particle swarm optimisation - a model based on the movement of bird flocks and fish schools, ant colony optimisation - a routine based on the social behaviour of ants, genetic algorithms and simulated annealing [77, 81–84]. The latter two are discussed in detail in section 3.2. Another subtype of LAs rising in popularity are artificial neural networks (ANNs) and deep learning (DL) which are models inspired on biological networks in the brain. These techniques excel in processing large datasets, often outperforming many of the other LAs described above. However, ANNs and DL require sufficiently large training/mock datasets to robustly and reliably extract the optimum output. They are also programmably more complicated and difficult to implement compared to other LAs [85].

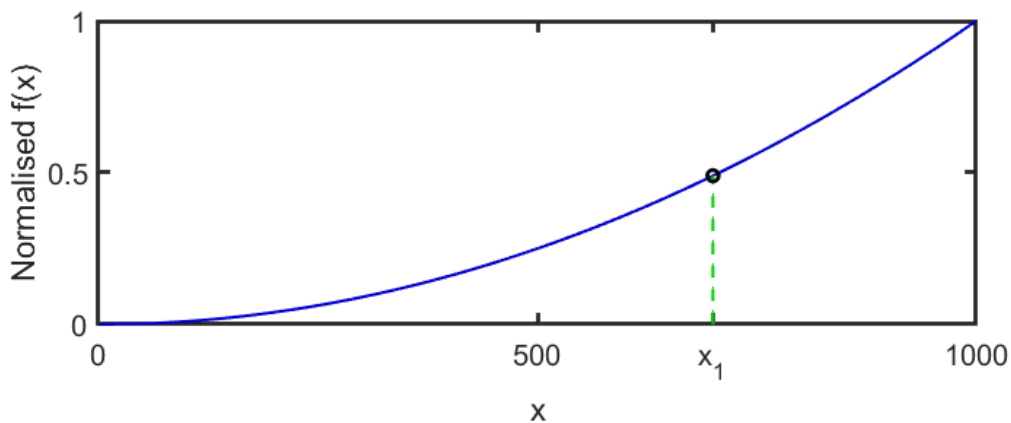
3.2 The genetic algorithm

3.2.1 Introduction

Genetic algorithms (GAs) are a subclass of evolutionary algorithms designed to optimise complex functions. Popularised by John Holland in 1960, GAs are inspired by Darwin’s theory of evolution. For this reason, many of the terms used in com-

Table 3.1: Genetic algorithm terminology.

GA terms	Description
Locus	A fixed position on a binary string
Chromosome	A binary string
Individual	The amalgamation of one or more binary strings
Fitness	A numerical value of a solution from an individual
Population	The number of solutions / individuals
Generation	An iteration of the algorithm



Binary string = [1010111100], with 10 loci.

Chromosome = a binary string with real value 700.

x_1 = an individual made from a single chromosome, green line.

$f(x_1)$ = the fitness of individual x_1 , black circle.

Figure 3.2: Genetic algorithm terminology example for a 1D function.

puter science are replaced with their biological counterparts. Table 3.1 displays a description of some of these terms and figure 3.2 displays an example of how these translate to a 1D problem. Variations of the algorithm have been applied in areas such as image processing, spacecraft trajectory planning, architecture design, artificial intelligence, and laser technology [86, 87].

Following figure 3.3, a typical GA will start with multiple random binary strings that make up the individuals of the first generation. In GAs the binary string length is arbitrary, however it is noteworthy that the string length is related to the precision of which the search space can be evaluated. Over many generations the algorithm will manipulate and evolve these strings by a set of rules to try and converge on the global maximum. The GA rules are shown in green in figure 3.3 and are described in subsections 3.2.2 through 3.2.6 [86–90].

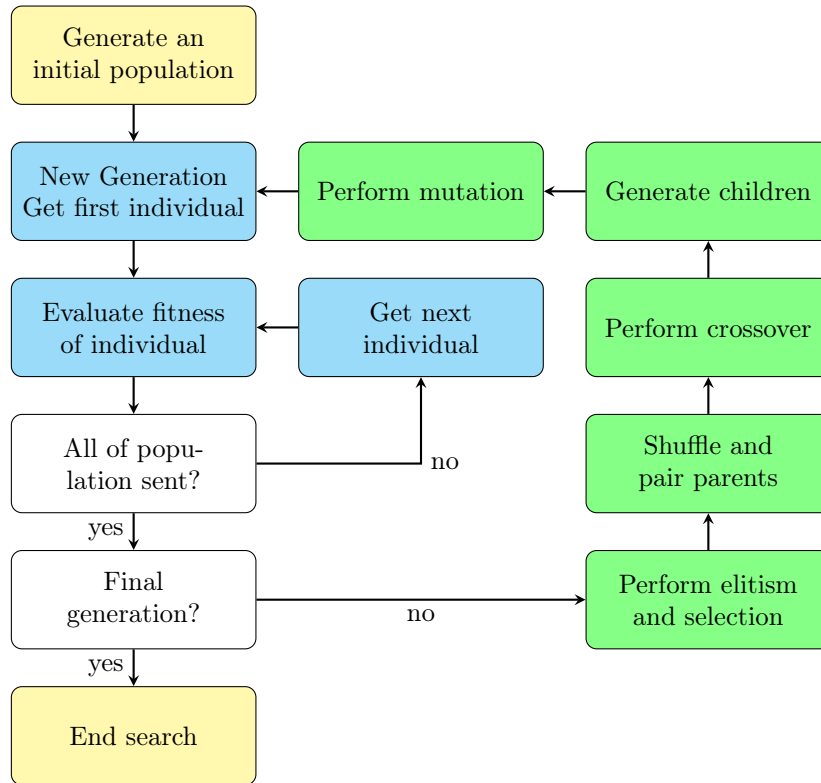


Figure 3.3: Genetic algorithm flow chart. Yellow boxes indicate the start and end of the algorithm. Green boxes indicate GA processes. Blue boxes indicate all other processes. White boxes indicate decisions.

3.2.2 Fitness

Fitness values are assigned for each individual to determine how ‘good’ the solutions are. The calculation(s) of these can vary widely depending on the problem, and can take into account one or more parameters. Biologically the ‘survival of the fittest’ ensures that fitter individuals are more likely to survive and pass their genetics onto future generations, while the unfit are removed from the gene pool. In parallel to this, in the GA fit individuals with good solutions aim to evolve over many generations to converge on the global maximum whilst the individuals with poor solutions are gradually discarded. To avoid confusion when comparing different algorithms this author will refer to evaluated cost functions as fitness values.

3.2.3 Selection

The selection process decides which individuals survive and go on to reproduce. There are many different selection methods, but all are dependent on the fitness calculated for each individual. In the simplest case, the top 50% of the population - as determined by their fitness - survive, removing the remaining 50%. The disadvantage with this method is that it decreases the genetic diversity of the population. This means that there is a chance that an individual with a poor overall fitness is removed even though they carried some key loci necessary for the optimum solution.

A popular selection process is called the roulette wheel method. This method mitigates the genetic diversity problem by distinguishing between ‘poor’, ‘good’, and ‘great’ individuals. In this regime all individuals are given a probability of survival proportional to their fitness values. For example, consider eight individuals, $N = 1, \dots, 8$, with fitness values f_N ($f_0 = 0$). Interval regions are calculated from the fitness values of each individual such that:

$$\sum_{j=0}^{N-1} f_j \leq F_N^{\text{int}} \leq F_{\text{tot}} - V, \quad (3.2.1)$$

where,

$$V = \sum_{i=N+1}^8 f_i, \quad F_{\text{tot}} = \sum_{k=0}^8 f_k, \quad (3.2.2)$$

and $V(N = 8) = 0$. A number is randomly chosen between 0 and F_{tot} , and the individual corresponding to the interval F_N^{int} is selected to survive. A visual representation is shown in figure 3.4 where a series of intervals are determined proportionally to each individual’s fitness and one is randomly selected. In the simple case, individuals are selected until 50% of the population is chosen this way. Each individual can only be selected once to continue to the next generation to avoid identical parents, this prevents the algorithm from converging too quickly and allows for more efficient coverage of the search space.

The drawback to this method is that the fittest individuals only acquire a higher

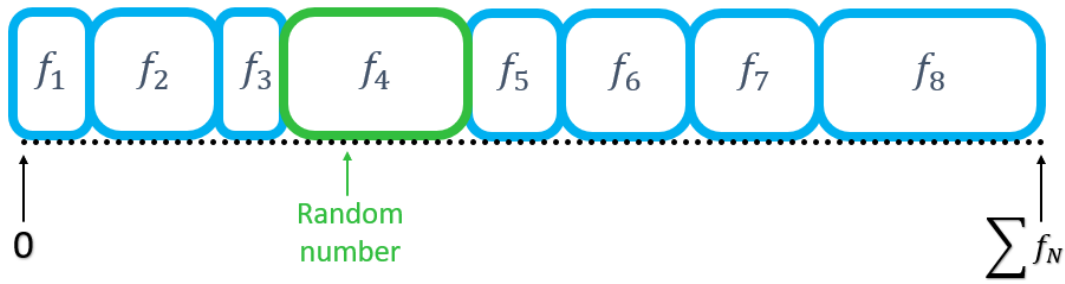


Figure 3.4: Visual representation of the roulette wheel selection method. A random number is chosen between 0 and the total sum of every individual's fitness, $\sum f_N$. The individual corresponding to the interval of the random number is chosen to survive.

selection probability instead of a guaranteed chance of survival. This problem is avoided by employing elitism as described in subsection 3.2.6. After the selection process is complete, individuals are paired up randomly to become parents for reproduction and genetic crossover.

3.2.4 Crossover

The crossover process serves as a way for the genetic algorithm to search through the search space. This is done by mixing the binary strings of two parents to create new individuals. This is analogous to parents passing their genetic information onto their children. In the simple case where 50% of the population are eliminated during the selection process, the crossover process will produce enough new children to conserve the population number.

Conventionally, crossover has an associated probability that determines whether the process occurs, or whether the children become exact clones of their parents. This probability of occurrence is commonly of the order of $> 70\%$. Clones are susceptible to mutation as described in subsection 3.2.5, where their chromosomes may be altered slightly to avoid early convergences. However, there is an advantage to cloning in the latest generations to hasten the algorithm's convergence around the best solutions found. If crossover does occur, there are several variations of how the chromosomes of the children are made.

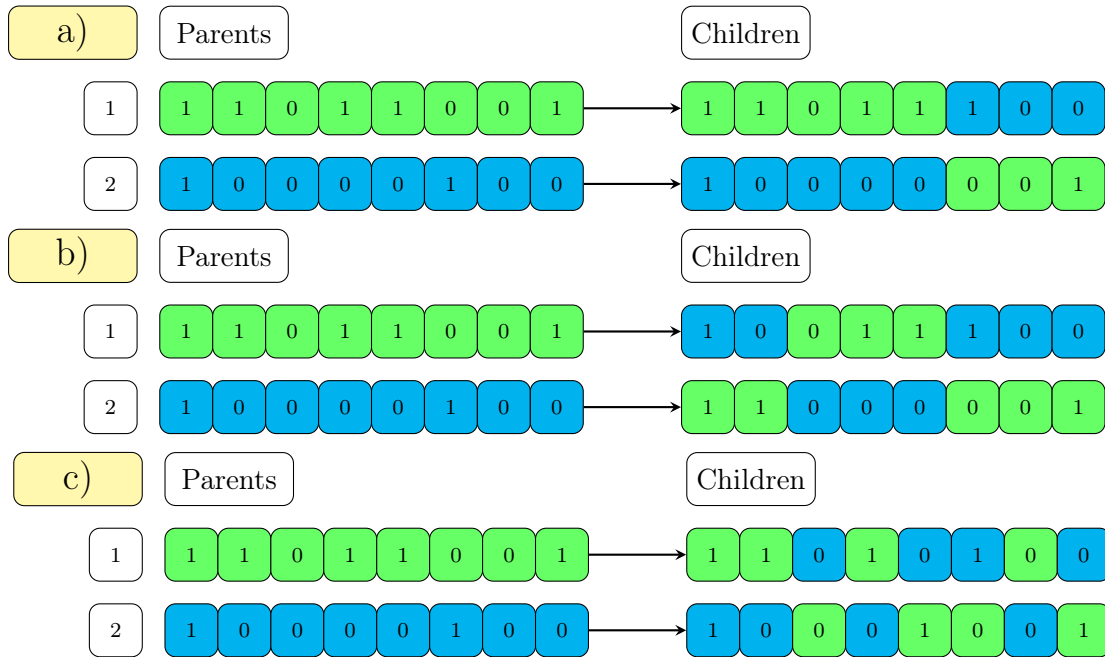


Figure 3.5: Illustration of crossover schemes, represented by 8-bit chromosomes for: a) single-point crossover, b) double-point crossover, and c) uniform crossover.

Three crossover methods are illustrated in figure 3.5 for chromosomes represented by 8-bit binary strings. Case a) describes single-point crossover. A random chromosome position is selected (here, the 5th locus), and the tail ends are swapped. Case b) describes double-point crossover. Two loci are selected at random and both the front and tail ends are swapped. Finally, in case c) a random and equal number of bits are selected to swap, this is known as uniform crossover. The advantage of uniform crossover is that the random binary changes allow the algorithm to rapidly search through the search space. However in binary the rightmost tail ends represent the smallest incremental changes. Convergence on the optimum solution would therefore require the fine tuning of these tails. Single-point and double-point crossover therefore allow the algorithm to converge faster, with single-point converging the fastest. For applications in this thesis, the single-point method was used.

3.2.5 Mutation and evolutionary pressure

During mutation the chromosomes are replicated with a small number of ‘mistakes’ as shown in figure 3.6. These mistakes are changes that can create individuals

either with a characteristic edge that gives them a greater chance of survival, or a characteristic flaw that worsens their chance of survival. After the crossover process, the loci from all individuals have a probability to randomly change from zero to one, or vice versa. This probability is problem dependent, however it is common to use a probability in the order of $1/L$ where L represents the length of the chromosome string.

Mutations allow the algorithm to progress by escaping local maxima, and reduce stagnation. If a GA does stagnate, evolutionary pressure can be introduced to increase the probability of mutations in a similar way to increasing the search momentum in gradient ascent. Mutations are beneficial to produce slightly better individuals to find the optimum solution. They also increase genetic diversity, and can slow down the speed of convergence, allowing the algorithm to search more of the search space. The drawback to mutating the entire population is that the best individual(s) can be given genetic flaws. This problem is removed by employing elitism as described in subsection 3.2.6.

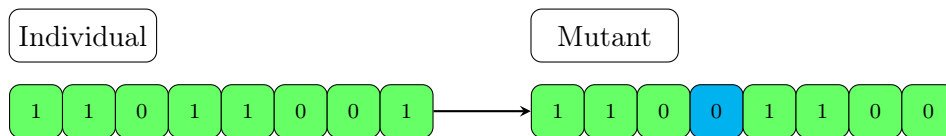


Figure 3.6: 8-bit single loci mutation example.

3.2.6 Elitism

During the crossover process there is a probability that the genetic information of individuals with the highest fitness is lost, reducing the effectiveness of the algorithm. To overcome this the elitism process ensures that the best individual(s) are preserved by automatically selecting them as parents, skipping the selection process. These elite parent(s) breed normally with the other individuals, but they are immune to any other changes such as mutation. Elite individual(s) are only forced to give up their immunity when fitter individuals are created. Typically, a genetic algorithm will have at least one elite individual.

3.3 The simulated annealing algorithm

3.3.1 Introduction

Simulated annealing (SA) algorithms have been in development since the 1980's. Just like GAs they are a good numerical method for difficult optimisation problems, and have been shown to out perform traditional hill-climb, and Kernighan-and-Lin algorithms [91,92].

SA is named after the physical process of annealing in chemistry and metallurgy in which a crystalline solid is heated and then slowly cooled. Over time this treatment changes the crystalline lattice configuration to become more regular, and removes impurities. The final result is a structurally superior material [93].

The basic routine of a SA algorithm is to navigate the search space and accept all changes that are better, but to also periodically accept changes that are less ideal with a probability, P_{SA} , which is related to a temperature, T . The algorithm routine is outlined in figure 4.7 [91,94,95].

3.3.2 Acceptance probability

Considering again the maximisation problem of a function, $f(x)$, over search space, x , each SA iteration starts with an initial, x_{initial} and a proposed change, x_{new} about x_{initial} . If $f(x_{\text{new}})$ improves the solution then it is automatically accepted as the next iteration's x_{initial} . This is exactly the same as gradient ascent, however in SA if $f(x_{\text{new}}) < f(x_{\text{initial}})$, a transition probability, P_{SA} , is calculated to accept x_{new} regardless. In SAs this probability is analogous to the Boltzmann distribution,

$$P_B = \exp\left[-\frac{\Delta E}{k_B T}\right], \quad (3.3.1)$$

where k_B is the Boltzmann constant, T is the temperature, and ΔE represents a change in energy. Instead let us define ΔE as the change in evaluated fitness of

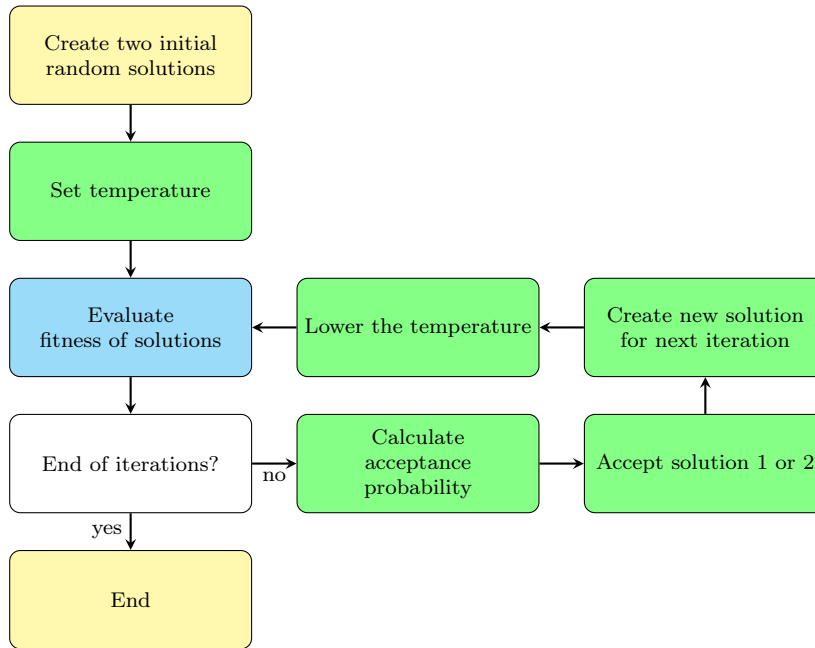


Figure 3.7: Simulated annealing flow chart. Yellow boxes indicate the start and end of the algorithm. Green boxes indicate SA processes. Blue box indicates non-SA process. White boxes indicate decisions.

the two solutions such that $\Delta E = \Delta f = f(x_{\text{initial}}) - f(x_{\text{new}})$, $k_B = 1$, and the temperature, T to be a problem-dependent parameter such that,

$$P_{\text{SA}} = \exp \left[-\frac{\Delta f}{T} \right]. \quad (3.3.2)$$

If this transition P_{SA} is larger than a randomly generated number, $P_{\text{SA}} > \text{rand}\{0, 1\}$, then the new change is accepted. In SAs the most important parameter to tune is the temperature. If the temperature is very large, $(T \rightarrow \infty)$, then $P_{\text{SA}} \rightarrow 1$, meaning all changes good or poor are accepted and the algorithm will erratically search and disregard the information from Δf . If the temperature is very small, $(T \rightarrow 0)$, then any poorer change will be rejected, limiting the ability of the algorithm to explore the search space. At $T = 0$, the algorithm reduces down to a gradient ascent algorithm by only accepting better solutions. The gradient or geometry of the temperature cooling over all iterations is free to define, however it's profile is often linear or exponentially decaying over the set number of iterations [81,91,93].

3.4 The hybrid algorithm

Within the literature there are several examples where algorithms are iterated between in order to find a solution. Such routines can use the GA or SA until a defined fitness criteria is met, at which point the other algorithm takes over with a seeded set of parameters in the search space from the best results found [96, 97].

Within this thesis the hybrid algorithm (HA) used does not follow this same blueprint described above. Instead the algorithm operates identically to the SA flowchart in figure 4.7, but the search space is binary encoded as used in the GA. These details are expanded upon in section 3.5.1. This subtle difference allows this algorithm to use the same genetic mutation described in section 3.2.5 as its primary way to navigate the search space, combining the searching capability of the GA with the simplicity of the SA.

3.5 Test problem

To test the RSA, GA, SA and HA, a 1D function was created with a search space equivalent to a 12-bit binary number in index, this is displayed in figure 3.8. Two notable features include: the existence of many local maxima to ‘trap’ the algorithms, and that the global and second maxima are very close in amplitude value to increase the difficulty in finding the optimal solution.

3.5.1 Algorithm implementation

The test function from figure 3.8 has a search space with decimal solutions in x . The binary encoded solutions using the GA and HA were therefore converted to decimal numbers before evaluating $f(x)$. The $d = 12$ -bit binary numbers $(d_{12} \dots d_2, d_1)$ were

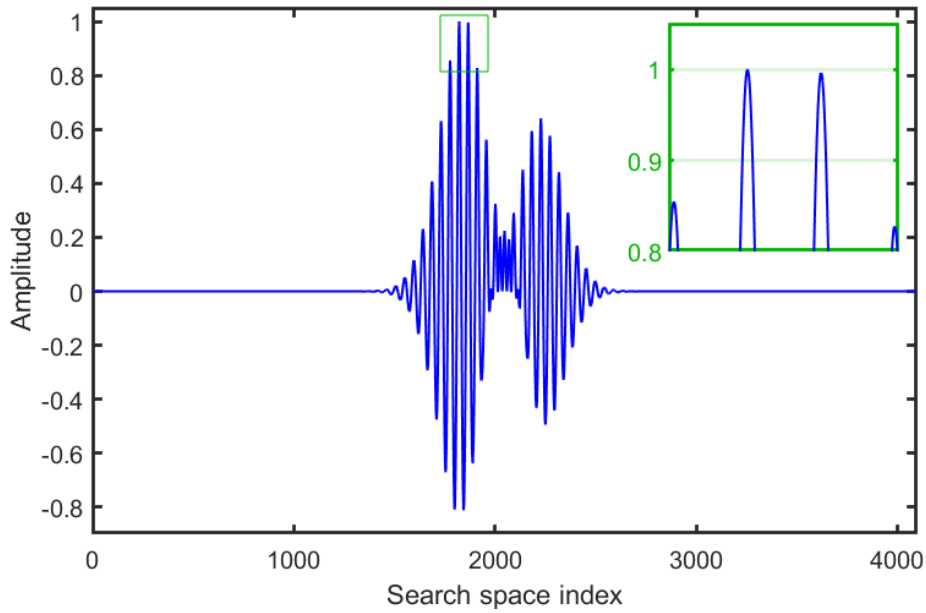


Figure 3.8: 1D test function with many local maxima. The search space index is over a 12-bit binary range. The zoomed in portion of the function between the global maxima and 2nd maxima have been highlighted in the green box.

converted to an index value, D , using,

$$D = \sum_{i=1}^{12} d_i(2^{i-1}). \quad (3.5.1)$$

This was converted to the corresponding decimal search space value within x using,

$$x = \left(\frac{D - D_{\min}}{D_{\max} - D_{\min}} \right) (x_{\max} - x_{\min}) + x_{\min}, \quad (3.5.2)$$

where D_{\min}, D_{\max} represent the binary index range and x_{\min}, x_{\max} represent the search space range of solutions. This type conversion was not necessary for the SA or RSA as each new proposed solution was chosen at a random point within x .

The parameters used by the GA, SA, and HA are displayed in table 3.2. The two search space values for the first iteration of the RSA and SA were chosen at random x positions, and the GA and HA began with multiple randomly scrambled 12-bit strings.

Table 3.2: Parameters of the genetic algorithm (GA), simulated annealing algorithm (SA) and hybrid algorithm (HA) for solving the 1D test function.

Parameter	Value	Algorithm
Population	8	GA
Crossover probability	100%	GA
Selection type	Roulette wheel	GA
Generation survival rate	50%	GA
Elitism on/off	On	GA
Number of elite individuals	1	GA
Mutation rate	30%	GA, HA
Maximum temperature	0.1	SA, HA
Minimum temperature	0	SA, HA
Temperature geometry	Linear	SA, HA
Generations / iterations	1500	GA, SA, HA

3.6 Results and discussion

Successful runs of the algorithms were when the global maximum of the 1D function in figure 3.8 was found. Statistics were also recorded for ‘good’ runs that instead converged on the 2nd maxima. Any other result was considered a ‘bad’ run. Figure 3.9 depicts the percentage of successful and ‘good’ solutions found from 10 000 runs of each algorithm. Figure 3.10 shows the convergence characteristics of a single run from each algorithm.

The RSA had the highest rate of failed runs and spent most iterations searching around the space outside of the central region of the test function and away from the global maxima. A better result was found by the final iteration however there was no discernible convergence. Other than the ease of implementation the RSA was outperformed by all other algorithms.

The GA was the most reliable algorithm with the highest success rate. Within the 10 000 iterations < 100 failed to find the global or 2nd maxima. From figure 3.10 the increase in the average fitness of the population shows a clear, steady convergence before plateauing after the global maximum was found. The main disadvantage with the GA was the complexity of implementation compared to the other three. Table

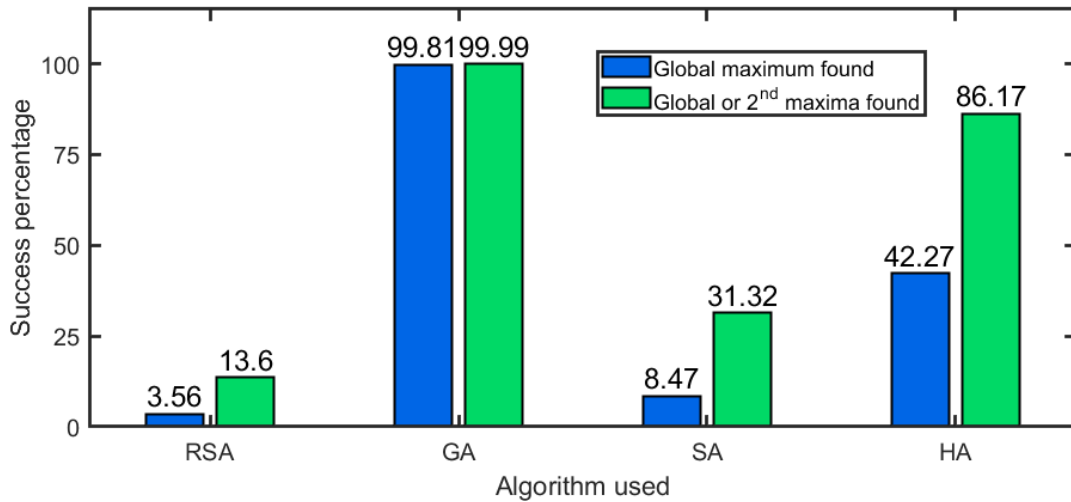


Figure 3.9: Global (blue) and global or 2nd maxima (green) found by the random search, genetic, simulated-annealing and hybrid algorithms after 10 000 runs at 1500 iterations per run.

Table 3.3: Summary of performance and complexity for the random search algorithm (RSA), genetic algorithm (GA), simulated annealing algorithm (SA) and hybrid algorithm (HA).

	RSA	GA	SA	HA
Performance	Poorest	Best	Second poorest	Second best
Complexity	Easiest	Hardest	Second easiest	Second hardest
Run time	Fastest	Slowest	Second fastest	Second slowest

3.3 displays a summary of algorithm performance, complexity and run time.

Although outperformed by the GA and HA, the SA exhibited a success rate over twice that of the RSA. Throughout most of the iterations the SA rapidly searched over the central region of the test function, however within figure 3.10 the fitness values are erratic. This type of algorithm may benefit from additional constraints on the choice of x_{new} to slow the convergence rate but more thoroughly search through the search space.

The HA offers a middle ground between the GA and SA in terms of complexity and reliability. Most of the early iterations are spent rapidly searching not unlike the SA, however the final $\simeq 250$ iterations show a far more controlled convergence.

All four algorithms have been shown to offer an improvement on the initial solutions. The performances from figure 3.10 show that the reliability and robustness

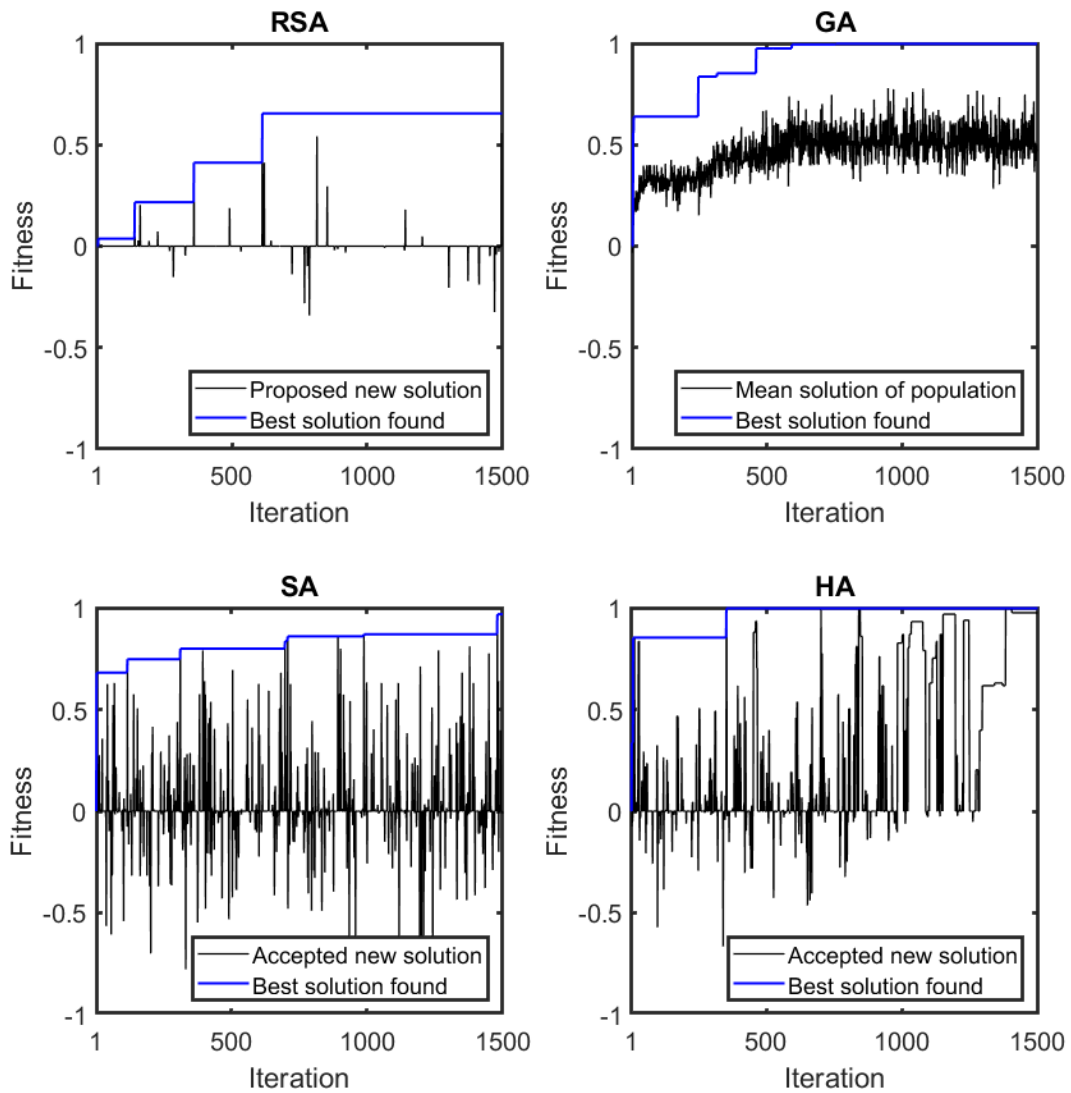


Figure 3.10: Fitness values over 1500 iterations of the random search, genetic, simulated annealing and hybrid algorithms.

scale with algorithm complexity. In chapter 4 the SA, GA and HA will be used in the application of beam shaping using adaptive optics. Within this thesis an additional Gerchberg-Saxton (GS) algorithm is utilised in section 5.7.4. This type of algorithm is tailored for retrieving the phase profiles between planes of two fixed intensity profiles.

Chapter 4

Beam shaping with a deformable mirror

"Positronium is intrinsically
unstable and prone to
self-annihilation, much like myself."

Robert Clayton

In this chapter experiments performed using a DM to shape the transverse spatial distribution of a CW laser beam at the focus are described. Using a wavefront sensorless approach, a set of learning algorithms developed by the author to stochastically optimise the Gaussian profile from a low powered He-Ne laser into super-Gaussian profiles of user-defined orders.

4.1 The deformable mirror

The first deformable mirror was conceptualised by Horace Babcock in 1953, with the intent to compensate for the effects of atmospheric turbulence on astronomical observations [98]. The correction element was made from a reflecting mirror covered by a thin layer of oil. A rastered electric charge was deposited on surface of the oil by conventional cathode-ray techniques, and through electrostatic forces the oil film is distorted according to the charge spatial pattern. Limitations of this device included slow corrections, high chromatic dispersion, and high environmental sensitivity [99].

Since this first demonstration, DM technology has evolved considerably. At present there are several different DM architectures commercially available. Two

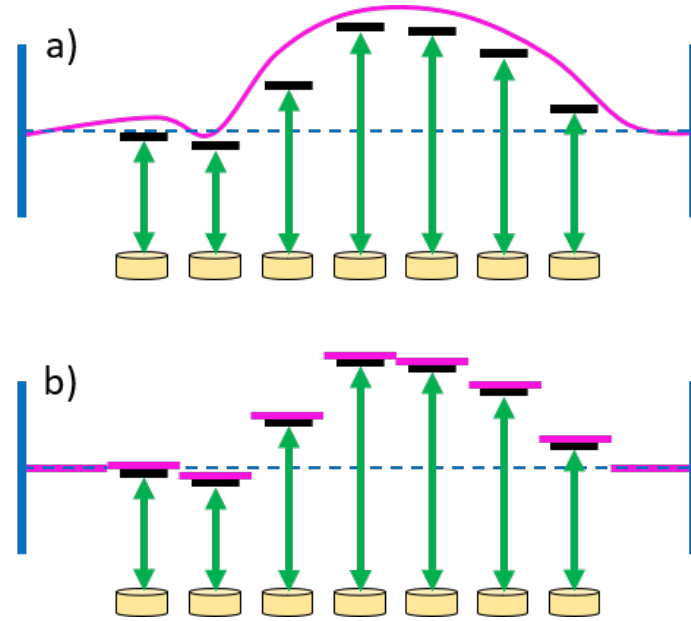


Figure 4.1: Cross-section illustrated examples of two deformable mirror architectures. a) a flexible membrane deformable mirror, b) a segmented deformable mirror. Actuators (black) are moved by their coupled coils (yellow) to manipulate the mirror surface (magenta).

popular types are the flexible-membrane and segmented mirrors, as illustrated in figure 4.1a and 4.1b respectively.

Flexible-membrane mirrors comprise of a continuous surface which can be manipulated by a series of actuators. The positions of the individual actuators can be controlled by applying a small current to their coupled coils. In segmented models, these actuators instead control the positions of a series of independent flat mirrors, with little to zero cross-talk of neighbouring actuators on the mirror surface. The disadvantage of segmented models is the presence of gaps and sharp edges between the individual mirrors, which can lead to scattering of the impinging light. In comparison, the flexible-membrane models do not have additional sources of scattering, and are therefore able to maintain higher optical power [100]. For this project, the flexible membrane ALPAO DM69 model was used. The DM specifications can be found in table 4.1 and the actuator layout in figure 4.2.

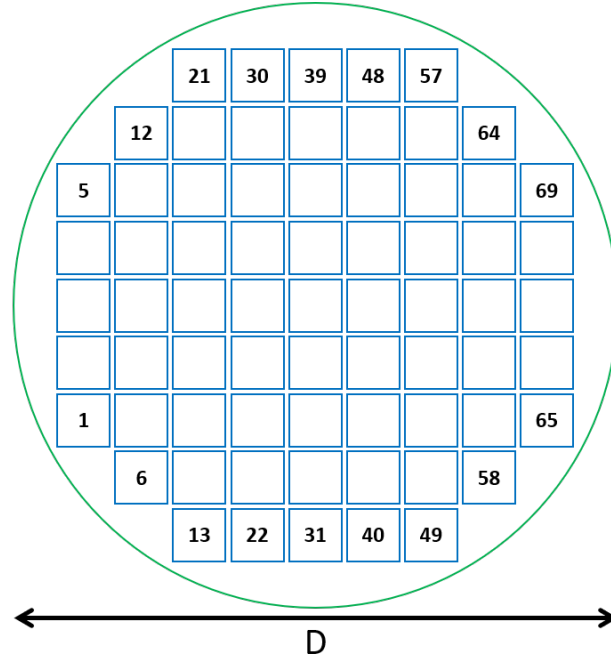


Figure 4.2: ALPAO DM69 square-actuator layout. Aperture diameter, $D = 10.5$ mm. DM specification is stated in table 4.1.

Table 4.1: ALPAO DM69 Specifications.

Specification	Value
Mirror type	Flexible membrane
Total actuator number	69
Pupil diameter	10.5 mm
Number of actuators across diameter centre	9
Approximate settling time	0.2 ms

4.2 Applications of deformable mirrors with optimisation algorithms

Due to their programmable nature DMs are frequently used together with optimisation routines to improve the quality of laser profiles [40, 101]. DMs have many desirable features for such applications, including their high reflectivity, a broad spectral range, high damage thresholds, the ability to correct high-order aberrations, and fast response times [102]. The many features of these devices has lead to their widespread adoption in fields such as astronomy, optical communications, microscopy, and quantum engineering [46, 103].

Experiments with DMs often use learning algorithms to optimise laser profiles. Stochastic optical reconstruction microscopy (STORM) is a super-resolution technique used commonly for the imaging of molecules [104, 105]. However, due to refractive and scattering characteristics of organic matter, a beam passing through larger biological samples can acquire optical aberrations. These aberrations degrade the point spread function (PSF), reducing both the localisation accuracy and the number of localisations needed to maintain STORM's high resolution. Experiments performed in 2017 used a DM with a particle-swarm optimisation (PSO) algorithm to compensate for the aberrations [106]. This technique was applied to imaging boutons located $100\ \mu\text{m}$ deep within *drosophila melanogaster* larvae, enabling a $146\ \text{nm}$ resolution to be achieved.

Pulse compression is a fundamental technique for nonlinear spectroscopy, optical communication, and ultrafast lasers [107]. Typically, combined passive elements such as gratings, static mirrors and prisms have been used to achieve pulse compression [108, 109]. One drawback of these is the inability to compensate for any arbitrary phase. An experiment in 1999 aimed to perform active pulse compression of a laser using a micro-machined DM. The DM surface was manipulated by a GA to introduce delays between different frequency components by adjusting the optical

path, before being reassembled. The results show a pulse compressed from 92 to 15 fs [110]. In 2018, the same technique was demonstrated using a more sophisticated neural-network algorithm. It was shown that convergence rates were on the order of $40\times$ faster - in terms of run-time - compared to a standard evolutionary algorithm [111].

DMs are regularly used in high power laser systems with peak intensities on the order of 10^{14} W cm⁻² [45, 112]. Experiments performed by Bonora et. al. used a DM controlled by a GA to optimise the signal of XUV harmonics created by a mid-infrared driving pulse. It was observed that the signal of the 5th harmonic was enhanced by a factor of two within ≈ 40 GA iterations [46]. Using a DM and a similar evolutionary algorithm, Bartels et. al. show high-order harmonic signal improvements by up to an order of magnitude [113].

Typical HHG experiments use a laser with a Gaussian profile to generate harmonics. During this extremely non-linear process harmonics are only made at the centremost area of the driver laser. For increased efficiency HHG can be driven with super-Gaussian profiles where more energy is concentrated within the centremost region. At present, the literature contains few examples of DMs being used to create super-Gaussian profiles at the far field. Several attempts to create super-Gaussian profiles using a DM controlled by a GA were hindered by a combination of the DM search range and algorithm efficacy [40, 114]. In 2007 Yang et. al. showed that this setup can be used for the generation of second-order super-Gaussian transverse profiles using a 19-actuator DM [43]. Similar results have also been show using a 37-actuator DM controlled instead by a SA algorithm [44].

This chapter will show that a DM can achieve super-Gaussian transverse profiles of finely-tuned orders from the Gaussian profile of a low-powered He-Ne laser. A non-stochastic approach to beam shaping with a DM would require pre-calculating the search space by calculating the influence function of all actuators using a ‘poke-matrix’ [40, 115]. This process is time consuming and the DM would require regular calibration. Learning algorithms offer a convenient way to manipulate the mir-

ror starting from an initial non-calibrated surface. In order to determine the best approach for generating tailored profiles using the available DM, a variety of optimisation routines were developed and implemented, including: GA, SA and a GA-SA hybrid. To expand on the work found in the literature the results will express the orders of achieved super-Gaussians, the power maintained within the beam centre, and the convergence and reliability of the algorithms used.

4.3 Experimental setup

Beam shaping experiments were made with a REO R-30991 continuous wave laser with wavelength, 633 nm. Since the beam diameter of the laser was approximately 1.5 mm, the beam needed to be expanded to fill the aperture of the DM. A Galilean telescope provided a $\times 4$ magnification. Collimation of the beam after the telescope was ensured by minimising the beam's defocus using a Thorlabs WFS150-7AR Shack-Hartmann wavefront sensor (WFS). After the telescope, the power transmission through an iris was measured for several iris diameters. The diameter of the iris was reduced in 0.5 mm increments from 11 mm (which exceeded the DM aperture), to fully closed. Images were taken with a iDS UI-388xCP-M CCD camera with 3088×2076 pixels and $2.4 \mu\text{m}$ individual pixel size. The integrated power transmission is,

$$\text{power transmission} = 1 - \exp \left[-2 \left(\frac{a}{w} \right)^2 \right], \quad (4.3.1)$$

where a and w represent the iris aperture and $1/e^2$ beam radius respectively [27]. These measurements, as well as a fit to the data using equation 4.3.1, are shown in figure 4.4. A value for the $1/e^2$ beam diameter of (6.12 ± 0.12) mm was determined from the fit to the data. The beam after the DM was focused with a $f = 250$ mm lens. The focal spot was magnified using an Olympus PLN10X $\times 10$ objective, and imaged with a CCD camera mounted on a Newport MFA-CC series motorised translation

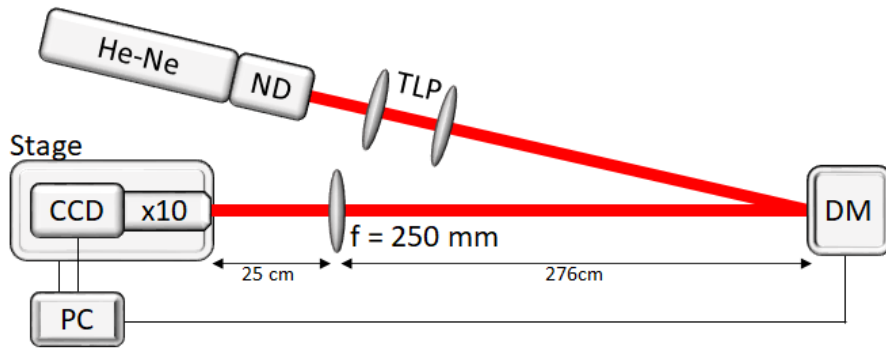


Figure 4.3: Schematic of shaping beamline, including the He-Ne laser, neutral-density filters (ND), a telescope-lens pair (TLP), deformable mirror (DM), $\times 10$ objective, and a CCD camera mounted to a computer-controlled translation stage. The angle of incidence of the beam onto the DM was $\approx 3^\circ$.

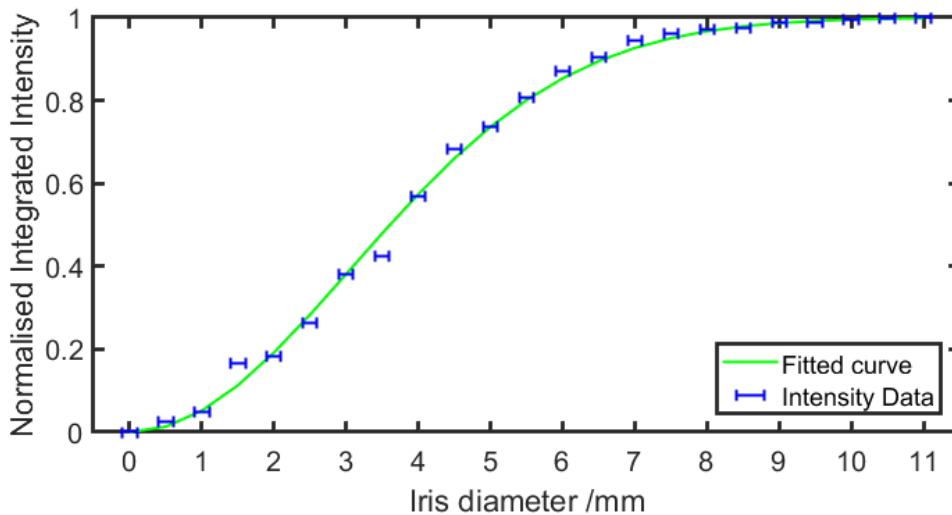


Figure 4.4: Power transmission through an iris as a function of iris diameter. The integrated signal at each iris position was the average taken over 50 camera exposures. The resulting signal errors were small and not visible within this figure. The beam diameter extracted from the fit was (6.12 ± 0.12) mm.

stage. The purpose of the objective was to ensure that a sufficient number of CCD pixels were illuminated for fitting routines. The setup for this is illustrated in figure 4.3. Neutral density (ND) filters were placed after the He-Ne to prevent the camera from saturating.

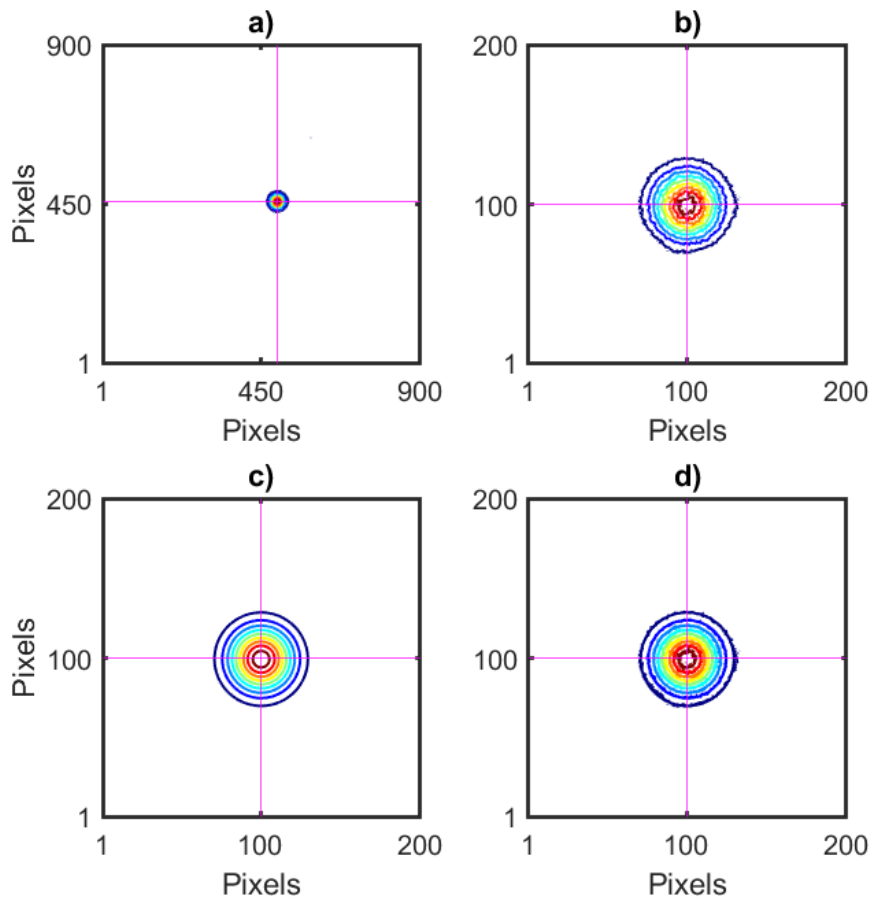


Figure 4.5: Contour plots of the 2D fitting process. a) the large static ROI. The location of the first moment is shown in magenta. b) the small ROI centred on the first moment. c) a 2D Gaussian fit. d) the 2D Gaussian fit from c) overlapping the data from b).

4.4 Genetic algorithm implementation

The vertical position of each actuator on the ALPAO DM were assigned by a 12-bit unsigned binary number that correspond to a normalised voltage $V = \pm 1$. These binary numbers are treated as the chromosomes that make up an individual. Each individual is therefore an amalgamation of the 69 actuator positions - creating a 828-bit binary number, which represents one surface of the DM. The GA and experimental parameters can be found in table 4.2. The experimental setup was as described in section 4.3.

The diameter of the initial He-Ne beam on the CCD camera was ≈ 100 pixels, a value much smaller than the 3088×2076 CCD pixel grid. Image capture from the

CCD was therefore limited to a static region of interest (ROI) of 900×900 pixels about the approximate beam centre. The computation time to fit a 2D $N \times N$ grid is $\propto N^2$. For fitting-time efficiency, a first moment calculation was made on the large ROI using equation 2.1.3 to create a smaller 200×200 pixel ROI about the beam centre. All 2D fitting routines were performed on this smaller ROI. This process is demonstrated in figure 4.5 for a Gaussian beam.

To start the GA minimisation routine, an initial population was made of an individual, $\text{ind}(1)$, with all voltages corresponding to $V = 0$ such that,

$$\text{ind}(1) = [011111111111, 011111111111, \dots, 011111111111], \quad (4.4.1)$$

and 15 other other individuals, mutated about $\text{ind}(1)$. Each surface was sent to the mirror, followed by a time delay of 0.2s to allow the DM to settle. For each image a background subtraction was performed by recording the average integrated signal in a 30×30 pixel window, located ≈ 400 pixels away from the beam centre and subtracting it from the recorded image.

A 2D fit of the measured intensity distribution was performed using MATLAB's least-squares routine, fitting a super-Gaussian,

$$\text{Fit} = \alpha_{\text{amp}} \exp \left[-2 \left(\frac{((x - \alpha_x)^2 + (y - \alpha_y)^2)}{\alpha_w^2} \right)^{\alpha_{\text{order}}} \right] + \alpha_z. \quad (4.4.2)$$

with free parameters for the amplitude, α_{amp} , width, α_w , positional offsets, $\alpha_x, \alpha_y, \alpha_z$, and super-Gaussian order, α_{order} .

The fitting outputs were the residual of the fit (res), and the fitted order (P_{fitted}). In order to optimise the energy within the $1/e^2$ beam diameter a masking function was applied. A disc was created about the beam centre approximately the size of the initial He-Ne beam diameter. The R_{mask} ratio of the intensity inside and the outside the disk area was,

$$R_{\text{mask}} = \frac{\sum I_{\text{Outside}}}{\sum I_{\text{Inside}}}. \quad (4.4.3)$$

Table 4.2: Parameters used in genetic algorithm.

Parameter	Value
Population	8
Generations	1500
Mutation probability children	1/200
Mutation probability parents	1/150
Crossover probability	70%
Selection type	Roulette
Generation survival rate	50%
Elitism on/off	On
Number of elite individuals	1
DM voltage range	$\pm 3.5\%$
Masking radius	40 pixels

Minimising this mask function optimises the light into the beam centre, reducing the widening of the beam. The fitness allocated to each individual was calculated by,

$$\text{Fitness} = W_{\text{res}} \times \text{res} + \frac{R_{\text{mask}}}{W_R} + W_p \times P_d, \quad (4.4.4)$$

where weighting factors W_{res} , W_R , W_p , were 10, 10 and 250 respectively, chosen such that each of the three fitness components start at approximately the same value. The fitness parameter, P_d , is the difference between the fitted and target super-Gaussian order as given by,

The power difference, P_d , was calculated by,

$$P_d = |P_{\text{fitted}} - P_{\text{target}}|. \quad (4.4.5)$$

where P_{target} is the user-defined target order of the super-Gaussian.

Selection and elitism were applied to select the best 50% of the population as parents. The parents are randomly shuffled, paired up, and bred to conserve the population number. Mutation was then performed on all but the single elite individual, creating the next generation. To hasten the convergence rates, non-elite parents underwent a lower mutation rate than the children.

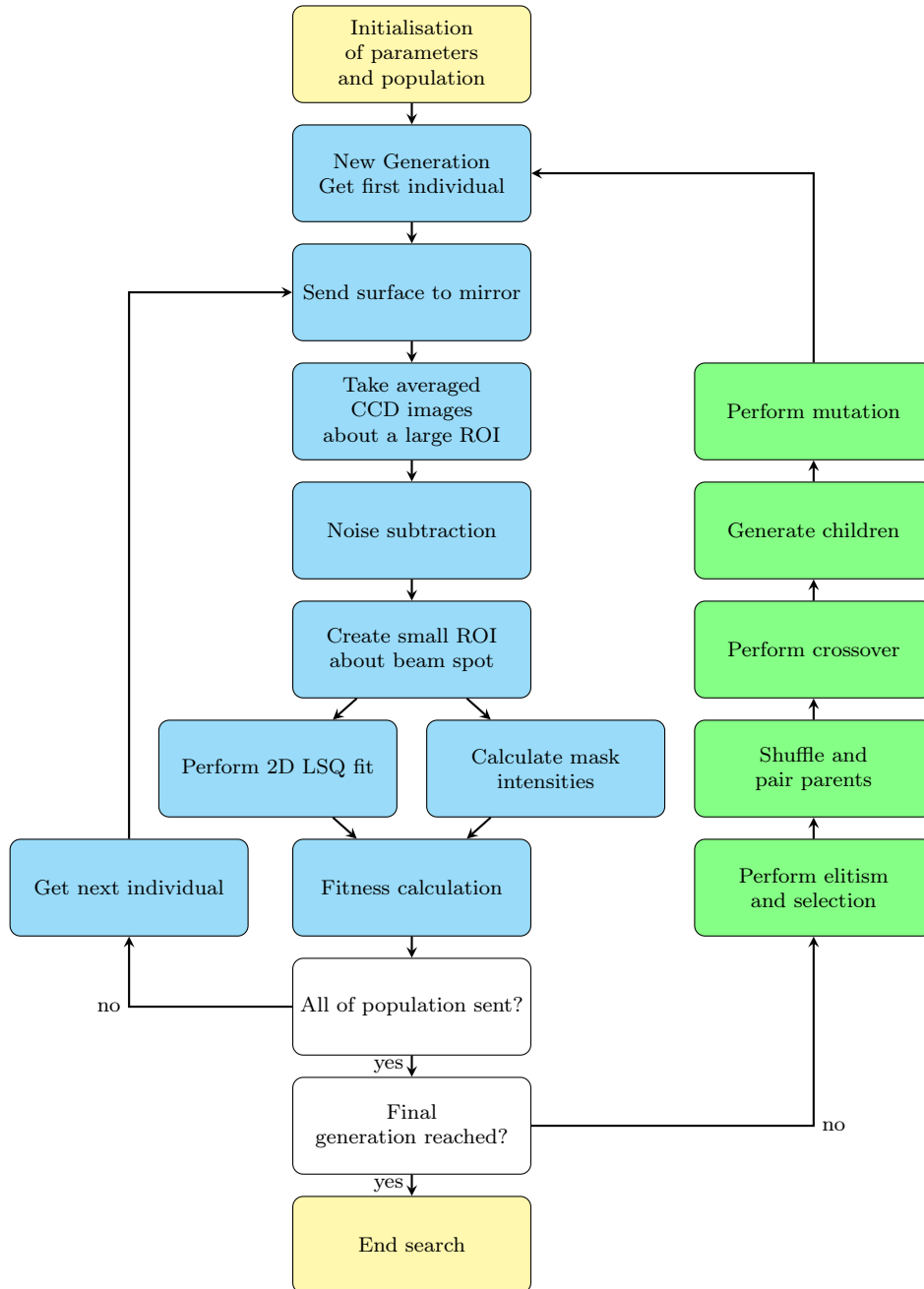


Figure 4.6: Flow chart of the genetic algorithm used to perform spatial shaping of a laser. Yellow boxes indicate the start and end of the algorithm. Green boxes indicate algorithm processes. Blue boxes indicates non-algorithm processes. White boxes indicate decisions.

4.5 Simulated annealing algorithm implementation

To compare the two algorithms directly, all mutual parameters and calculations have been kept the same such as iteration number, fitness calculations and DM actuator range. The other parameters for SA are displayed in table 4.3, with the flow chart in figure 4.7. The SA as displayed in this figure compares two surfaces per iteration, whereas the GA compares 8. For this reason, it was taken that four iterations at the same temperature of the SA algorithm would be the equivalent of one GA iteration.

The standard SA algorithm does not use binary encoded actuator positions. Instead, the first perturbed surface is generated using random actuator positions between the maximum and minimum voltages, V_{\max} and V_{\min} . After the first iteration all actuators are subjected to random perturbations within the range of

$$\text{Pert}_{SA} = 0 : \frac{|V_{\max}| + |V_{\min}|}{16}. \quad (4.5.1)$$

This range is based on values used by Fayyaz et al [116].

4.5.1 Genetic simulated annealing hybrid implementation

The genetic-simulated-annealing hybrid algorithm (HA) follows the SA routine found in flow chart in figure 4.7. However, the surfaces are binary encoded in the same way as the GA. In this version of annealing the HA utilises the GA mutation method described in section 4.4 to perturb the surface of the DM. To ensure the search space was more thoroughly explored the mutation rate was chosen to be the same as the children in table 4.2.

Table 4.3: Beam shaping simulated annealing parameters.

Parameter	Value
Maximum temperature	0.1
Minimum temperature	0
Temperature geometry	Linear
Weighting constants	$k_B = \gamma = 1$

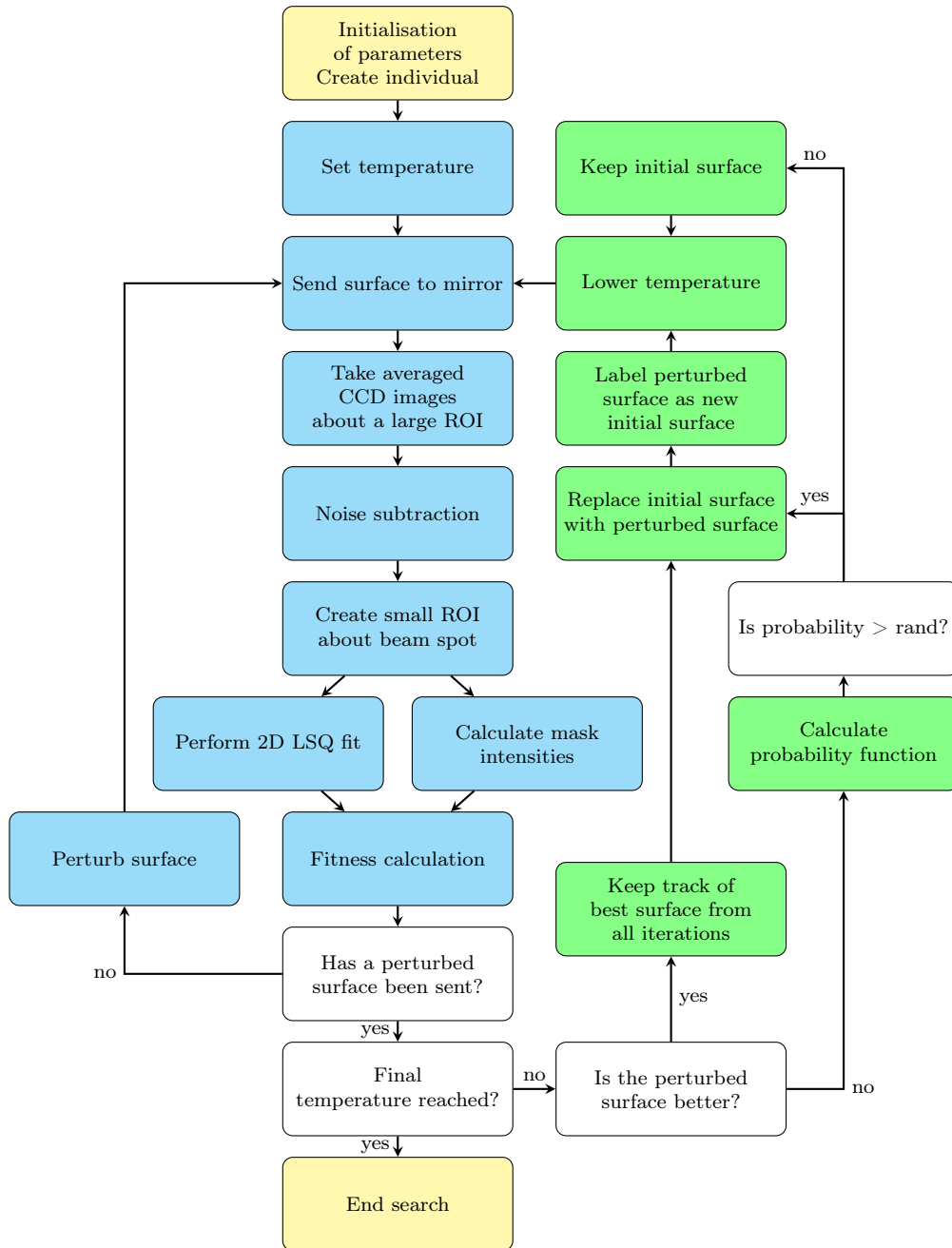


Figure 4.7: Flow chart of the simulated annealing algorithm used to perform spatial shaping of a laser. Yellow boxes indicate the start and end of the algorithm. Green boxes indicate algorithm processes. Blue boxes indicates non-algorithm processes. White boxes indicate decisions.

4.6 Pre-optimised beam profile

The GA, SA, and HA were all initialised with a surface that corresponded to 0 V across all DM actuators. This initial surface does not correspond to a flat mirror surface. The pre-optimised transverse profile of the He-Ne laser at the focus is shown in figure 4.8 where for clarity the achieved beam profiles are also shown on a \log_{10} scale. Aberrations are clearly present on the beam. Post-optimisation, fewer discernible structures should be found away from the beam centre.

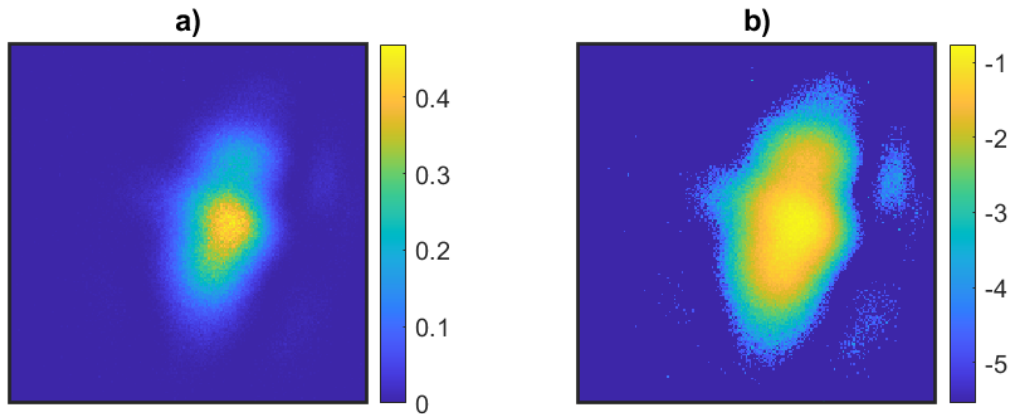


Figure 4.8: Pre-optimised transverse beam profiles from a He-Ne, on 200×200 pixel grids. a) beam profile. b) \log_{10} scale beam profile.

4.7 Algorithm results

4.7.1 Transverse beam profiles

Using the setup previously described in section 4.3 the GA, SA, and HA were used to generate a range of super-Gaussian transverse intensity profiles at the focal plane. These profiles are displayed in figure 4.10. The SA profiles show more scattered light outside of the beam centre for all target orders. For the GA and HA the target orders $P < 1.4$ there is visibly less scattered light outside the beam centre up until $P \geq 1.4$. This implies that there are still some aberrations present on

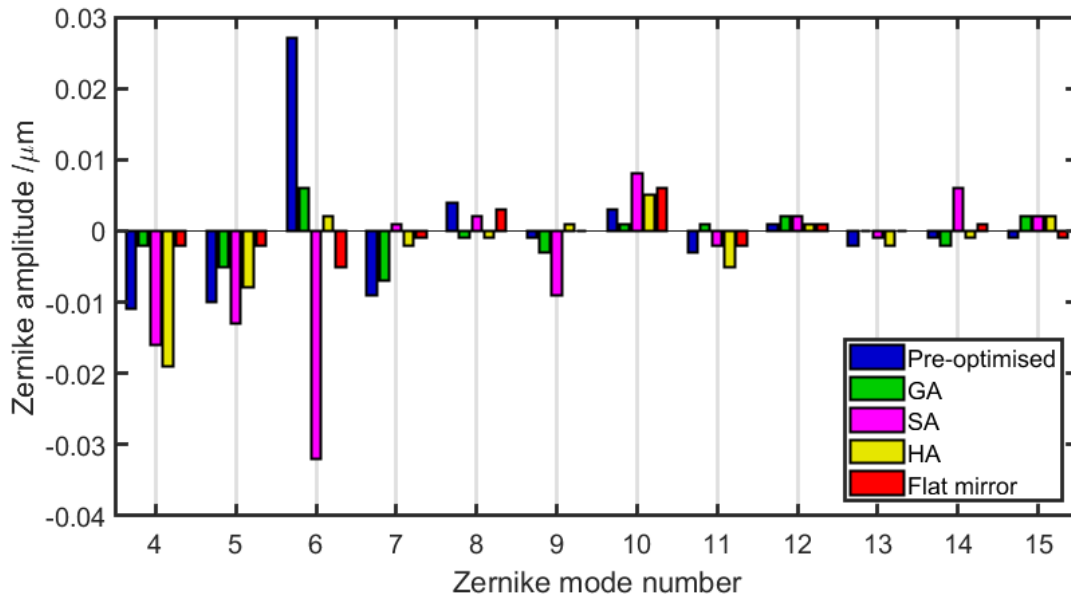


Figure 4.9: Amplitudes of Zernike modes at the back focal plane of a focusing lens before optimisation (blue), then after a genetic (green), simulated annealing (magenta) and hybrid algorithm (yellow), as well as a static flat mirror (red), for a target $P = 1$ Gaussian profile. Piston, tip, and tilt modes are not displayed.

the beam. The wavefront of the beam was characterised after each algorithm using a WFS. Zernike polynomial amplitudes (see Appendix:A1) at the back-focal plane of the focusing lens were recorded for target order $P = 1$. These amplitudes are shown in figure 4.9 for the beam profile pre-optimisation, the GA, SA and HA, and for a flat static mirror. From this figure the algorithm post optimisation with the fewest aberrations is the GA. The optimised profile with the SA and HA show that significant aberrations for the lowest modes are still present on the beam.

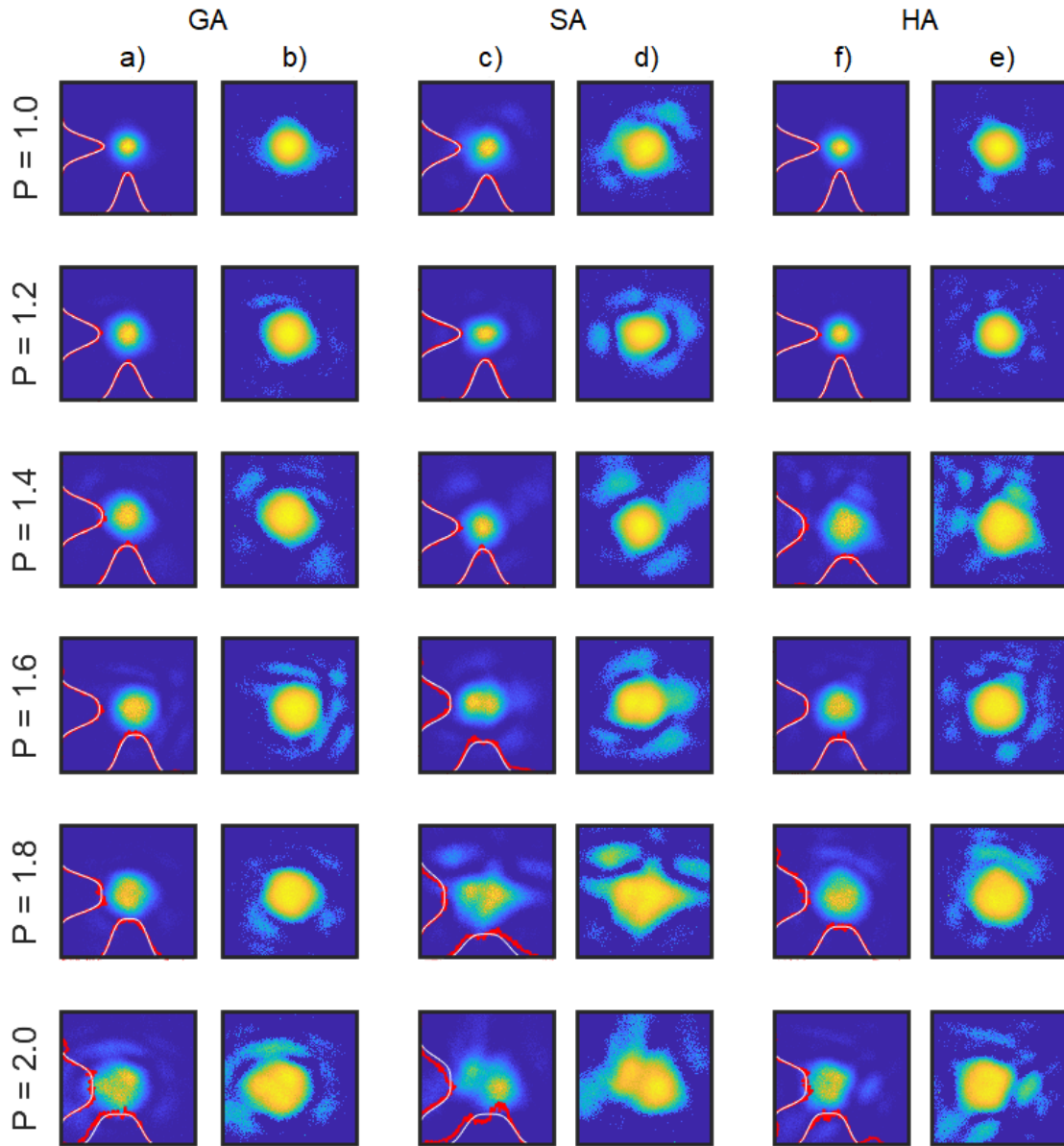


Figure 4.10: Super-Gaussian transverse profiles achieved with a genetic (GA), simulated annealing (SA), and a hybrid algorithm (HA), using a deformable mirror. P denotes the target order. Image size of 200×200 pixels. Columns a, c, and f show the normalised CCD images, with data lineouts along the X and Y first moments in red and lineouts along the same location from the 2D fitted super-Gaussian profiles in white. Columns b, d and e show the CCD images on a log scale to highlight the scattered light outside the beam centre.

4.7.2 Achieved orders and algorithm robustness

To assess reliability the GA, SA, and HA measurements were repeated three times. Figure 4.11 a, c, e, shows that all algorithms were able to maintain over 70% of the beam intensity within the $1/e^2$ diameter. However, in contrast to the SA, the GA and HA were able to consistently achieve the target super-Gaussian order.

To further assess the consistency of the three algorithms, amplitudes and widths after optimisation were compared. These results are shown in figure 4.11 b, d, f, where the theoretical optimum amplitudes calculated are also displayed. These optimum values were calculated from the measured beam widths and target super-Gaussian order relative to the beam profile achieved for order, $P = 1$, using equation 2.1.2. From figure 4.11 b, d, f, the SA was able to achieve profiles with near-optimum amplitudes. However the GA and HA show a greater level of consistency, particularly for target orders $P > 1.4$.

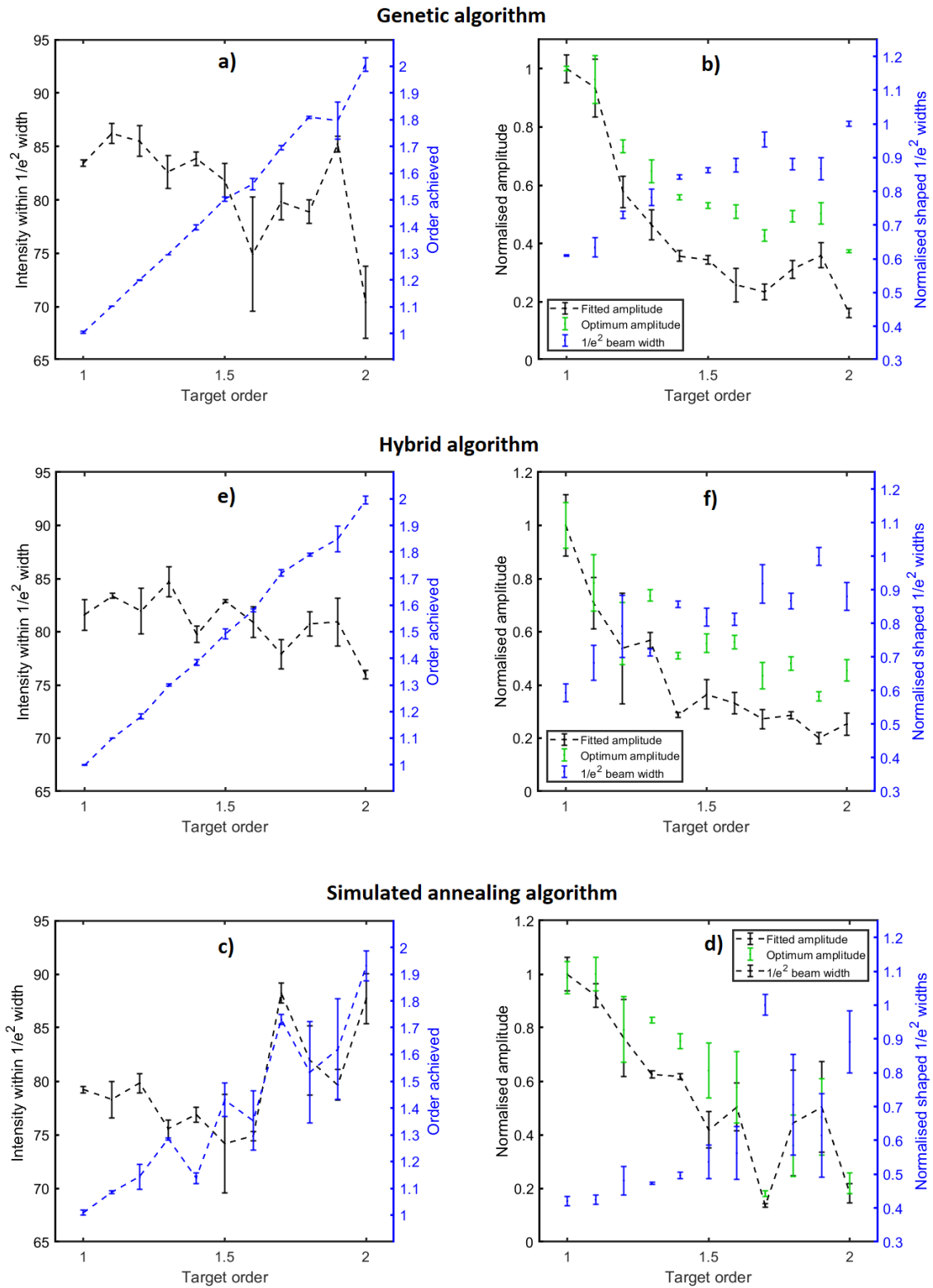


Figure 4.11: Super-Gaussian orders, intensity maintained within beam centre, and widths and amplitudes measured from three runs of the GA, HA and SA.

4.7.3 Algorithm convergence and run-time

To view the convergence of each algorithm fitness values were recorded after each iteration from equation 4.4.4. The convergence is shown in figure 4.12 for super-Gaussian orders, $P = 1.1$, $P = 1.5$, and $P = 1.9$. Within this figure the SA shows convergence on higher fitness values with increasing super-Gaussian order and converges later than the GA and HA.

A key parameter to calculate in optimisation routines is the runtime. The run-times of each algorithm were measured for 100 iterations. Figure 4.13 shows the average time per iteration for all three algorithms, as well as a variant of the hybrid algorithm ($HA_{T=3}$ discussed in section 4.7.4), and the CCD image capture, 2D fitting and mirror settling time. From this figure it can be observed that all three algorithms have approximately the same runtime.

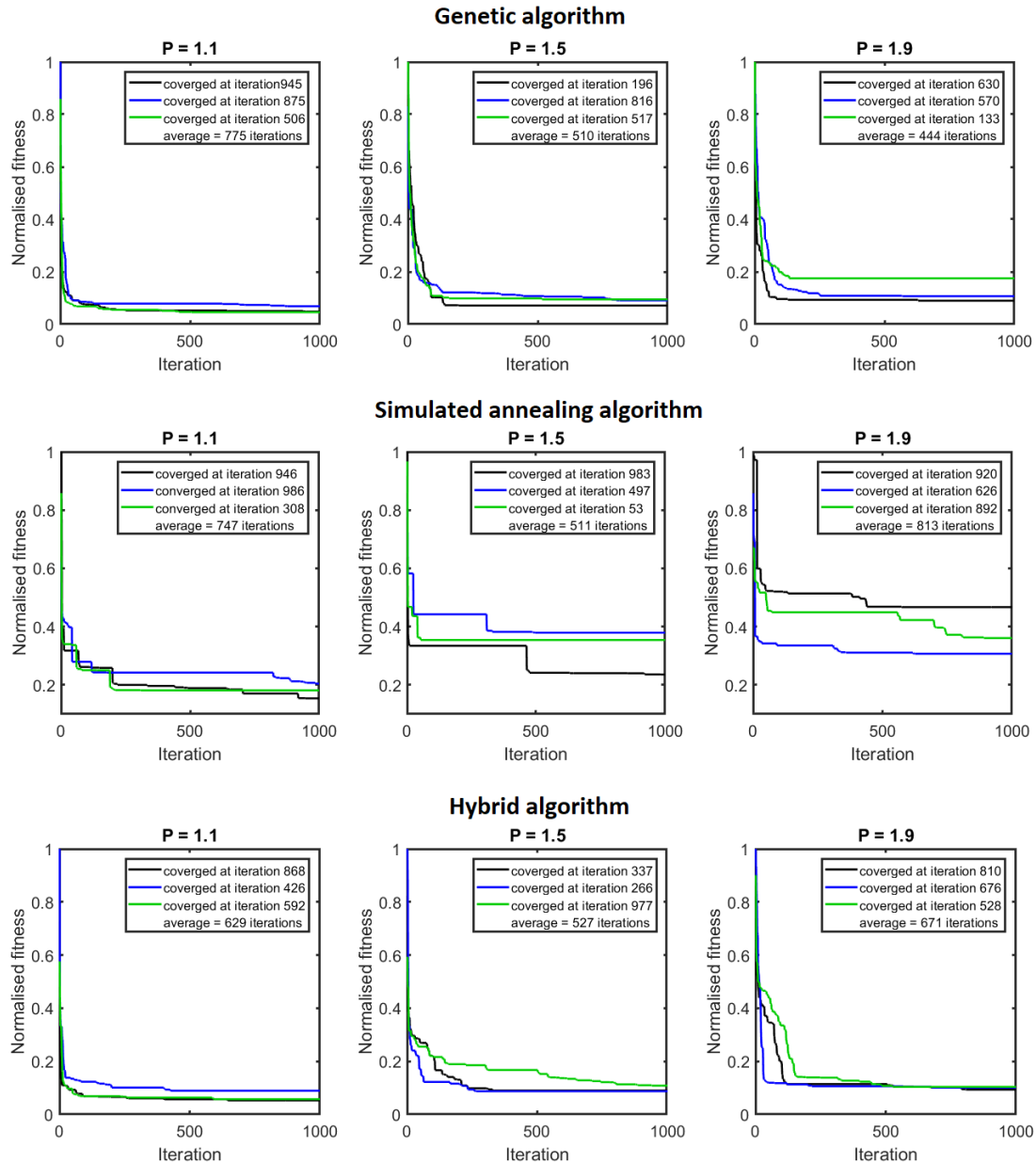


Figure 4.12: Convergence rates of the best result found over 1000 iterations for the GA, SA and HA, for super-Gaussian orders $P = 1.1, 1.5, 1.9$.

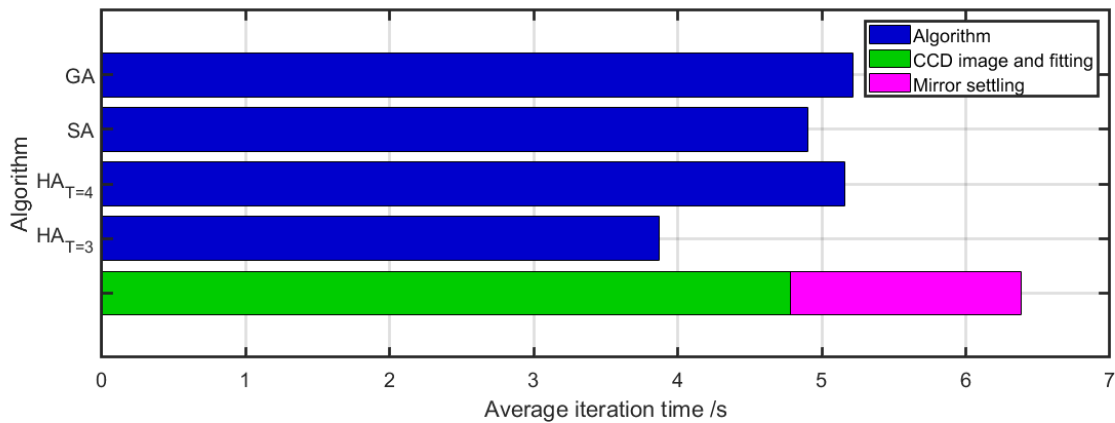


Figure 4.13: Runtime of the GA, SA, and HA, averaged over 100 iterations, sending identical initial surfaces to the deformable mirror per iteration. The HA performance for $T = 3$ and $T = 4$ per iteration are shown. The CCD capture time, 2D least-squares fitting time, and deformable mirror settling time are also included.

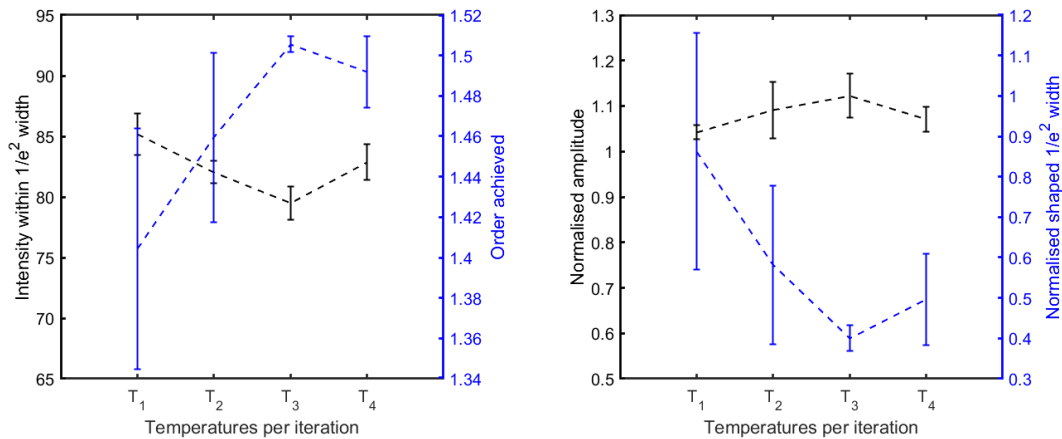


Figure 4.14: Super-Gaussian order, signal maintained within beam centre, and widths and amplitudes measured from three runs of the $T = 1, 2, 3, 4$ temperatures per iteration hybrid algorithm, for target order $P = 1.5$.

4.7.4 Hybrid algorithm runtime improvement

Comparing the results in figures, 4.9 through 4.13, the HA has proven to be a middle-ground option between the GA and SA in terms of performance, consistency, convergence and speed. To numerically test the limits of the HA, it was ran for values of $T = 1, 2, 3$ temperature repeats per iteration. From figure 4.13 it can be seen that each reduction in the number of temperatures improves the algorithm runtime by $\approx 25\%$ as expected. For target order $P = 1.5$, figure 4.14 shows the achieved super-Gaussian order, intensity within the beam centre, and the calculated

beam amplitudes and widths. These results show that the HA is only consistent for $T > 3$, and that $T \leq 2$ sacrifices performance significantly.

4.8 Discussion

The GA was the most reliable algorithm, with results from figure 4.11 showing convergence on consistent beam widths, amplitudes, and orders. One disadvantage of the GA is the increased number of core-steps - such as selection and crossover - within the algorithm, making it the most complex and difficult to implement out of the three.

The SA was the least consistent routine, it often missed super-Gaussian target orders, and introduced more Zernike aberrations for order $P = 1$. Although there were marginal improvements in the SA runtime, figure 4.12 shows that average convergences occurred later than the GA and HA.

The HA inherited the beneficial traits of both algorithms, exhibiting similar consistent results as the GA in figure 4.11 for achieved orders, amplitudes, widths and central beam intensity maintained. The $T = 3$ HA offers a runtime improvement over the SA and GA for similar performances.

Finally this wavefront sensor-less approach to beam shaping showed that although the GA and HA improved the Zernike aberrations for order, $P = 1$, some aberrations were still present on the beam. Higher super-Gaussian orders have also been achieved consistently with these two routines. A notable advantage to using these routines is the ability to bypass the calibration process of the deformable mirror, as well as the potential to search for other arbitrary beam shapes.

Chapter 5

Beam shaping with a spatial light modulator

"The world is not ready for my
words of wisdom."

Sam Offler

In this chapter a spatial light modulator (SLM) will be used to shape the transverse spatial profile of a CW laser beam. A known π -shift method for realising tunable super-Gaussian profiles is investigated and compared to an approach using a learning algorithm. This will be followed by a discussion on beam shaping with dual adaptive optic (AO) techniques.

5.1 The spatial light modulator

Spatial light modulators (SLMs) are adaptive optic elements consisting of an array of programmable pixels arranged in 1D or 2D. Light is manipulated locally about different pixels by changing the optical paths [117,118]. Based on the birefringence of liquid crystals (LCs), a LC-SLM modulates light. The optically-transparent LCs are confined in a cavity between these pixels and a window. LCs with a positive dielectric anisotropy change their orientation by aligning themselves in the direction of the electric field which in turn changes the refractive index [119,120]. SLMs operate either in reflection or transmission. Transmissive SLMs have an LC layer between two windows instead of one; a well-known example of this is the liquid crystal display (LCD). Reflection SLMs have a single window and a reflective layer of pixels. These

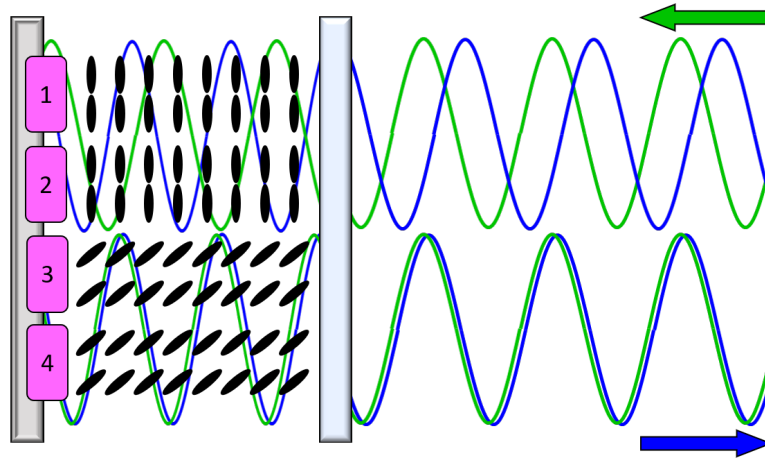


Figure 5.1: Schematic illustration of the operating principle of a phase-only LC-SLM. The reflective pixels are coloured magenta, the liquid crystals are represented by black ovals, the transparent window is in light blue, and the incoming and outgoing beams are coloured green and dark blue respectively.

typically have a larger dynamic range as light propagates twice through the LC modulation layer. LCoS (liquid crystal on silicon) are the most popular SLM of this class and mostly use either phase-only or amplitude-only modulation [121]. An example of a phase-only SLM is displayed in figure 5.1.

For decades high-in-demand applications such as the LCDs, image projection, digital holography, micro-processing, telecommunications, and optical vortex generation have attracted a lot of funding into the development of SLMs [117, 120, 122]. In the context of adaptive optics, SLMs offer similar beam control and shaping capabilities to deformable mirrors. The following two sections will discuss examples of SLMs for shaping experiments, and then the use of SLMs in HHG experiments.

5.2 Beam steering and shaping with a single SLM

SLMs have been used in laser systems as control devices with the ability to remove aberrations [122, 123]. Changing the refractive index across the SLM changes the phase of light propagating through the material. This introduces a phase shift across the SLM that allows these devices to steer the direction of the beam [120].

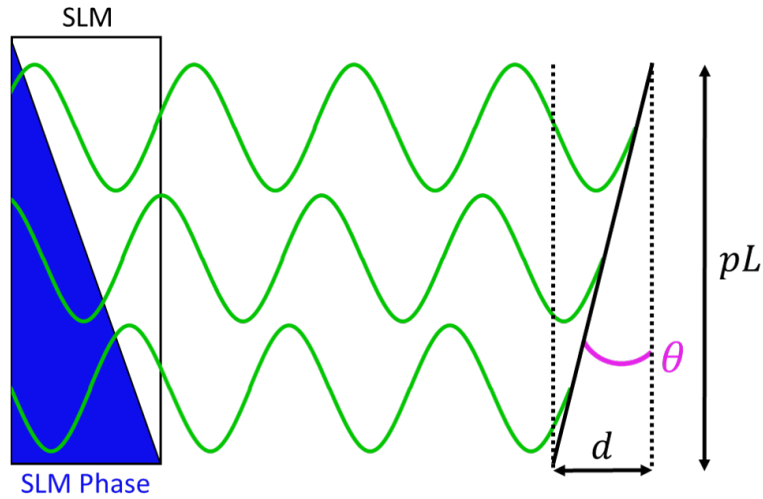


Figure 5.2: Illustration of a linear phase shift producing a tilt in the wave front equal to θ . The optical period, pixel width and path difference is given by L , p and d respectively.

For example, a 1D linear phase shift across an SLM creates a shift equal to,

$$\phi(r) = \frac{r}{L} 2\pi, \quad (5.2.1)$$

where L is the optical period. This shift produces a tilt on the optical wave front by an angle θ , such that,

$$\tan \theta = \frac{d}{pL}, \quad (5.2.2)$$

where d is the path difference and p is the pixel width. This is illustrated in figure 5.2. At the far field this changes the transverse position of the beam [124].

The ability to shape and steer simultaneously are ideal for applications such as ‘optical tweezing’, which was the shared subject of the Nobel Prize in 2018 with CPA. Optical tweezers (OTs) are particle or molecule trapping mechanism which has found applications in microbiology [37–39]. A realised use for OTs is as a precise drug delivery method to small optically transparent biological structures such as neurons [125]. Another proposed application is to combine OTs with laser zona drilling for fertilisation. In this process a micrometre hole is drilled directly into an egg cell to breach the zona pellucida via laser, then the potentially movement-inhibited sperm cell can be guided through using an OT [126].

Several tweezing experiments were performed in the 2000s by researchers such as Eriksen, Bowman and Wulff. They showed that a single SLM can both correct the wavefront which is important for imaging biological samples where tissues don't have a uniform refractive index, and at the same time manipulate the positions of single or multiple micron-scale particles [127–129].

Dark hollow (or 'doughnut') transverse laser profiles are desirable in applications such as atom trapping and atom guiding to limit the motion along the optical axis [130–132]. Numerous experiments have shown that transverse hollow-Gaussian and Bessel-like profiles can be achieved by use of a single phase-only SLM [133, 134].

5.3 Spatial light modulators for HHG

The reflectivity of an SLM is typically $\approx 90\%$ compared to a deformable mirror ($> 97\%$) [135]. The additional loss of light is due to the diffraction into higher orders by the grating-like structure of the pixel grid, the light absorption between the pixel gaps, and the loss of light between the multiple layers of the SLM structure. SLMs are therefore more susceptible to damage by mechanisms such as the heating of the LC layer and laser ablation of the LC confining substrates [117]. Despite their lower damage threshold SLMs have been used on HHG beam lines for applications such as pulse shaping and holography [136, 137].

In 2012 Eyring used a Ti:Sapphire laser with a central wavelength of 800 nm, pulse duration 30 fs, and peak intensity $3 \times 10^{15} \text{ W cm}^{-2}$, in combination with a phase-only SLM to improve the harmonic yield. The phase mask of the SLM was manipulated by a genetic algorithm where the fitness values were calculated from the intensities of the harmonics using a spectrometer. Post optimisation a six-fold increase in harmonic intensity was observed from the 21st to the 35th harmonic order [138]. The optimised driver beam profile was observed to have a lower maximum peak intensity and a larger diameter, indicating that correcting the wavefront is fundamental for the efficiency of HHG. Walter et al. used a similar laser, SLM,

and optimisation algorithm to demonstrate spatial control to concentrate as much intensity into the generating region of a hollow-core waveguide. They demonstrated an increase in harmonic intensity from the 17th to the 23rd harmonic order of up to a factor of five [139].

5.4 SLM simulation setup

For the remainder of this chapter simulations will be made of beam shaping using a phase-only SLM. As an alternative to using static elements, deformable mirrors, or two-optical-path mirrors, an SLM will be used to spatially shape the transverse Gaussian profile from a He-Ne CW laser into super-Gaussian profiles of various orders, with the intended application of driving HHG [49].

The simulation setup is based on the setup as shown in figure 4.3 where the SLM replaces the deformable mirror. The SLM surface and the CCD detection plane are positioned in an $f - f$ arrangement at the front and back focal plane of a thin lens, respectively to take advantage of the Fourier transform relationship between these planes as described in chapter 2 [60, 140].

Sections 5.4.1 and 5.4.2 will outline and compare two methods of super-Gaussian generation. The first method applies a top-hat phase shift with an amplitude of π . The width of this shift is proportional to the super-Gaussian order achieved within the beam centre. The second method will use the SA and HA algorithms applied previously to the deformable mirror in chapter 4 to achieve profiles of multiple target orders.

5.4.1 π -shift shaping method

Treacher et al (2020) demonstrated that an SLM can be used to create super-Gaussian spatial profiles to drive and improve the brightness of single harmonics [50]. The technique used imprinted a π -phase shift transversely onto a collimated

Gaussian beam. This technique was based on the two-optical-path mirror [49], where a single phase step caused the centre and periphery of the beam to interfere at the focus, changing the transverse intensity profile. Further details on the π -shift shaping method for HHG can be found in references [48, 50].

π -phase shifts of multiple widths were imprinted onto a Gaussian profile of $1/e^2$ width w_G , at the SLM and propagated by the Fourier transform method to a detector plane, where the SLM and detector are in the back and front focal plane of a lens, respectively. Figure 5.3 displays intensity profiles at the detector plane after π -shifts of widths $0.800 w_G$, $0.925 w_G$, and $1.400 w_G$, with the super-Gaussian fits to these profiles which have fitted orders $P = 2.62, 1.77$, and 1.16 respectively. For π -shift widths greater than w_G the shaped profiles at the focus become increasingly Gaussian-like. At a width equal to $1.5 w_G$ the fitted order $P \approx 1$. Figure 5.3d displays an intensity profile near this limit at $1.4 w_G$.

Figure 5.4a displays the super-Gaussian order generated as a function of the π -shift width. It can be observed here that the fitted errors increase with super-Gaussian order. This means that there is a compromise between super-Gaussian order and quality. Figure 5.4b displays the intensity maintained within the beam centre at the detector plane relative to the $1.5/e^2$ width of a Gaussian at the detector plane without any phase shift from the SLM. This shows that more intensity is lost within the beam centre for higher orders of super-Gaussians.

5.4.2 Algorithm shaping method

In this section the π -shift method will once again be used to generate super-Gaussian profiles of multiple orders. The fitted super-Gaussian profiles and orders will be the target inputs into the feedback loop of learning algorithms to investigate if any improvements can be made on the quality of the profile. The quality of the super-Gaussian will be calculated from the error in the fitted order, P .

A numerical study of optimisation algorithms for wavefront shaping using an SLM was carried out by Fayyaz et al. in 2019. They outlined six algorithms in-

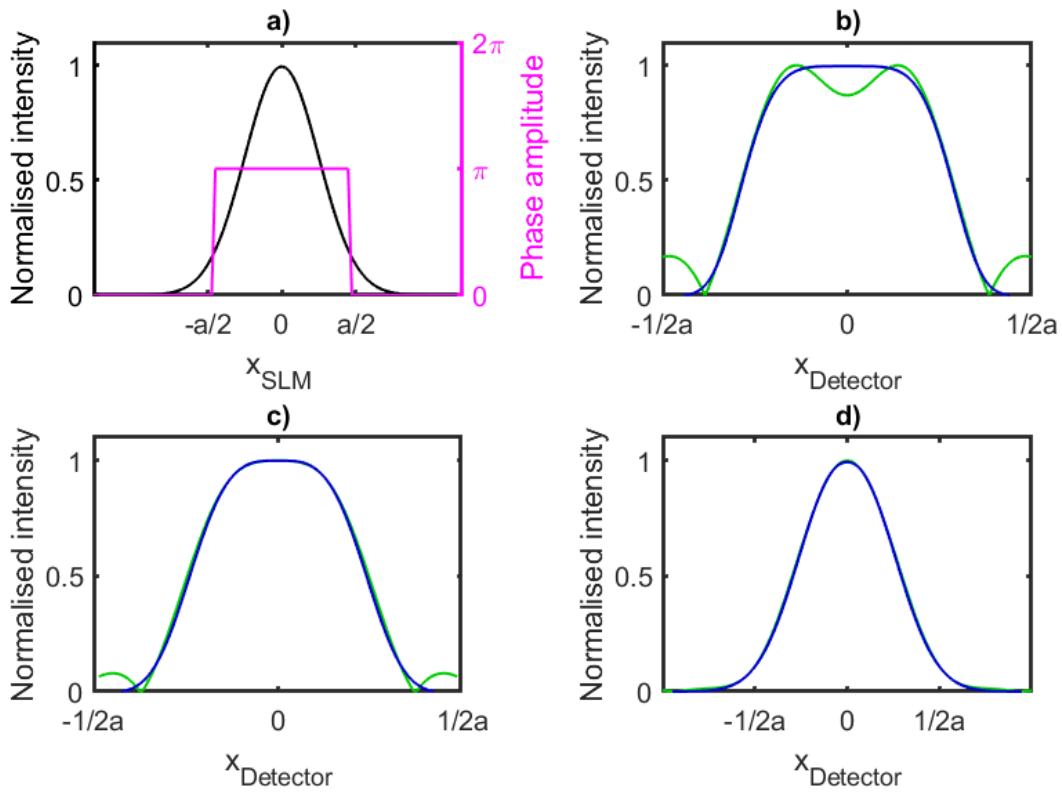


Figure 5.3: Super-Gaussian generation from π -phase shifts. a) initial Gaussian in black, example phase shift shown in magenta. Intensity profiles at the detector plane for imprinted phase shift widths of $0.800 w_G$, $0.925 w_G$ and $1.400 w_G$ where w_G is the initial Gaussian width are shown in b), c) and d) respectively in green, with fitted super-Gaussian profiles in blue.

cluding simulated annealing that can be implemented on a SLM [116]. Within this section the SA has been utilised by this author in a simulation to generate super-Gaussian profiles of user-specified orders. These results will be compared to the profiles obtained by the hybrid algorithm as used in chapters 3 and 4 and the π -shift method.

Assuming cylindrical symmetry the simulations were made in 1D. A collimated Gaussian of radius w_G from the He-Ne is incident onto a phase-only SLM surface with pixel width $p_w = 0.05 w_G$. The farthest pixel from the beam centre is $2.5 w_G$, which is sufficiently larger than the $1.5 w_G$ limit discussed in 5.4.1 for returning a profile with super-Gaussian order $P \approx 1$, at the focus.

The two learning algorithms used are a standard simulated annealing algorithm based on the version used by Fayyaz et al. and an adapted hybrid algorithm (HA)

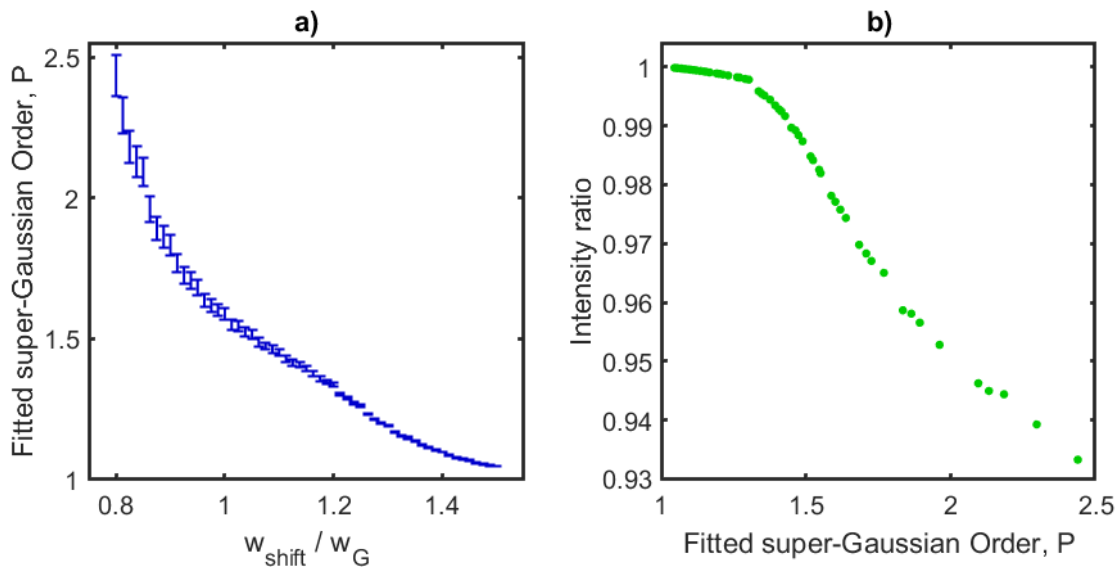


Figure 5.4: a) Fitted super-Gaussian orders with fitting errors. b) Beam intensity maintained within the beam centre.

Table 5.1: SLM simulated annealing (SA) and hybrid algorithm (HA) parameters. Some SA parameters as used by Fayyaz et al. [116].

Parameter	Value	Algorithm
Iterations	10 000	Both
Mutation probability	1/16	HA
Pixels perturbed	Random 50%	Both
SA Perturbation	$+(1/2^8)\pi$	SA
HA Perturbation range	$+0 : 2\pi$	HA
Maximum temperature	1	Both
Minimum temperature	0	Both
Temperature geometry	linear	Both

from chapter 4 [116]. Both algorithms follow the flow chart from figure 4.7 with parameter values from table 5.1. The acceptance probability was calculated from equation 3.3.2 and the fitness of the initial and new proposed solution were calculated from the sum of the square of the differences between the intensity profile of the beams and the target super-Gaussians. The perturbation method for both algorithms randomly selected 50% of the SLM pixels per iteration. The perturbation amount, P_ϕ , used by Fayyaz et al. was [116],

$$P_\phi = \frac{\pi}{2^n}, \quad (5.4.1)$$

with $n = 4$, such that in the SA each pixel of the SLM could hold one of 32 values between 0 and 2π . For beam shaping experiments this value may not be sensitive enough, however the benefits are that the learning algorithm evaluate over a relatively small search space and are likely to converge on a good solution quickly. For applications in this chapter, $P_\phi(n)$ was optimised in the SA by using a target $P = 1.77$ for $n = 4$ through to $n = 10$. The achieved orders for multiple n -values are shown in figure 5.5a along with the comparison to the result from the π -shift method. Figure 5.5a show that $n = 8$ was the optimum value, narrowly achieving the target order within the fitting error. Figure 5.5b then shows that $< 10\,000$ iterations was sufficient for fitness convergence for $n = 8$.

In the HA the pixel perturbation was set to a range $0 : B_d$, where B_d was the decimal value from an 8-bit binary number with a maximum value of 2π .

For both the SA and HA, any SLM pixel perturbation that would have a phase shift value greater than 2π was wrapped back around to 0.

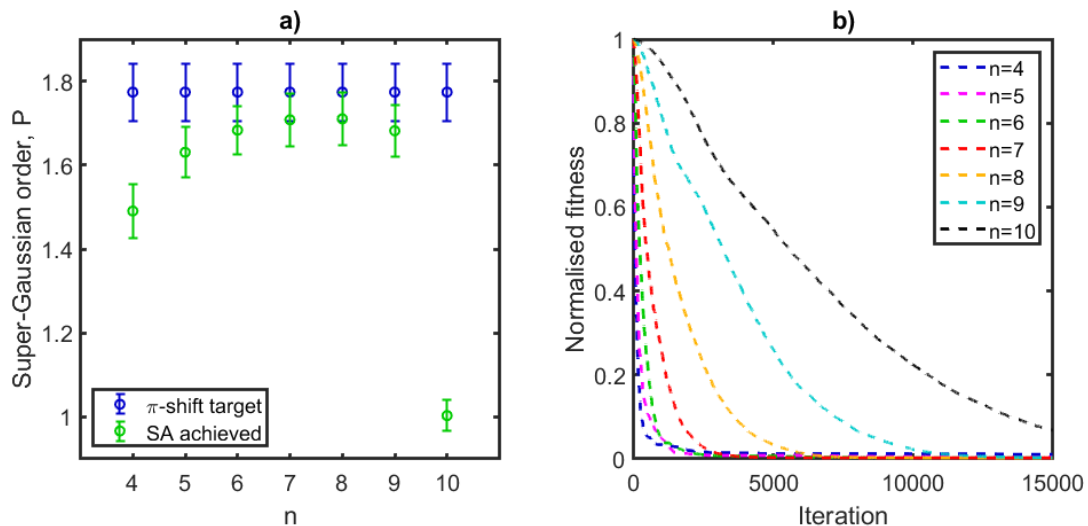


Figure 5.5: a) Super-Gaussian target order from π -shift method in blue, SA achieved order in green, for multiple n -values. b) Fitness values for SA iterations for multiple n -values.

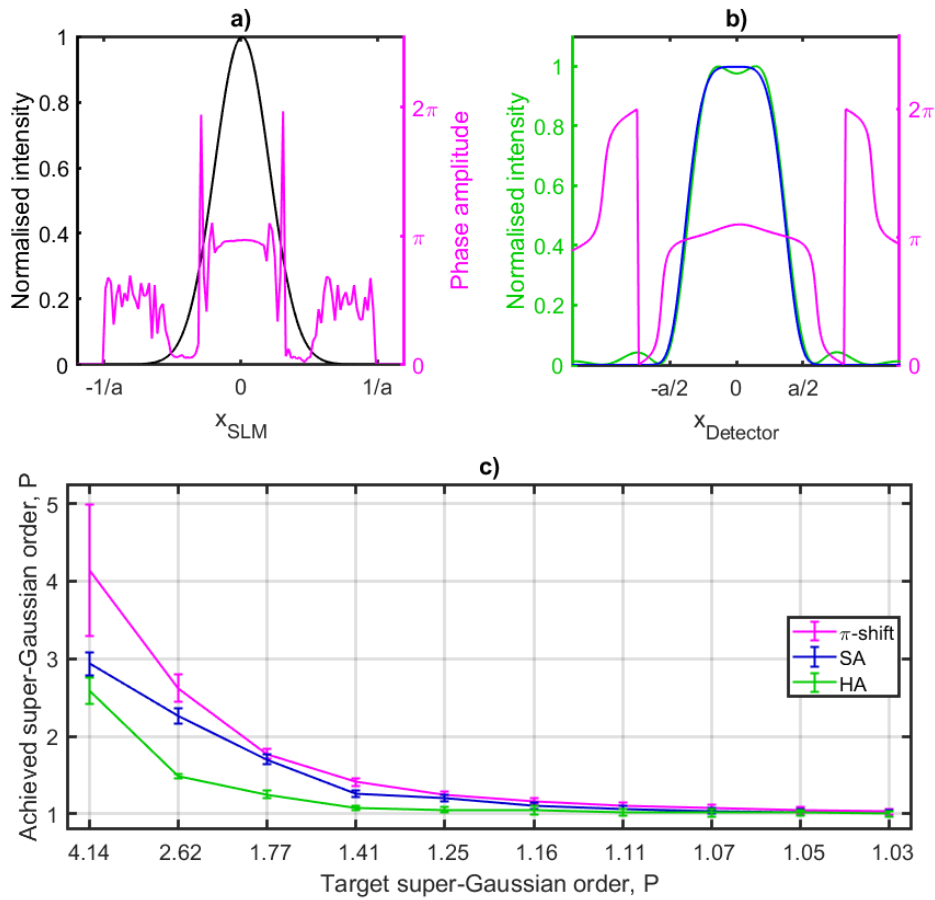


Figure 5.6: a) Gaussian profile in black, SA imprinted phase solution in magenta for a target super-Gaussian $P = 2.62$. b) Intensity profile at the detector plane in green with the fitted super-Gaussian in blue with fitted order $P = 2.26 \pm 0.09$, and phase profile in magenta. c) Super-Gaussian orders achieved by the SA, HA and π -shift method, plotted relative to the order from π -shift method.

5.5 SLM shaping results

Figure 5.6a and b show a result from the SA algorithm for super-Gaussian target order $P = 2.62$. Figure 5.6c then shows the results of the super-Gaussians achieved using both the SA and HA algorithms compared with super-Gaussians generated by the π -shift method. It was observed that the SA algorithm outperformed the HA algorithm in terms of super-Gaussian order achieved. However for target order $P = 4.14$ although the HA did not reach the target order, it did achieve an order higher than the $P = 2.62$ target but with a smaller fitting error than the π -shift method.

5.6 Other SLM shaping considerations

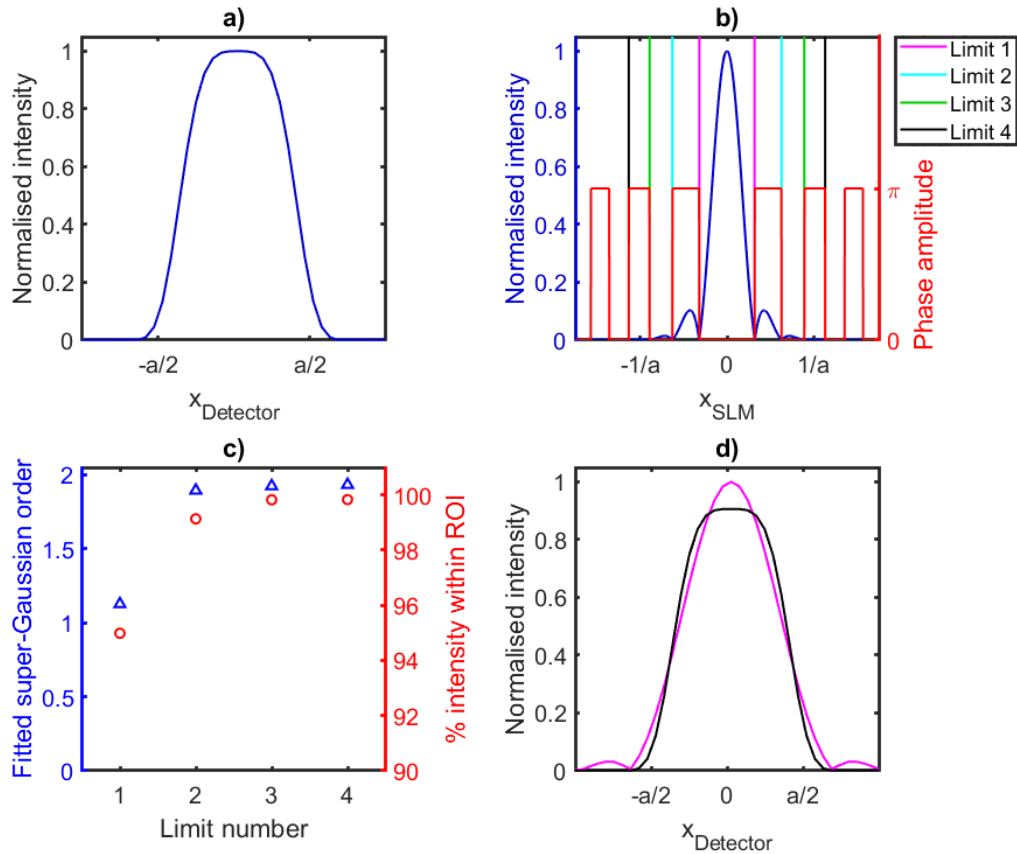


Figure 5.7: a) Target intensity profile at the focus, $P = 2$, with a flat transverse phase. b) Back propagated field from the target to the SLM plane. Intensity profile in blue, phase profile in red. The magenta, cyan, green and black lines ("limits") outline the four regions where the beam will be truncated and propagated forwards to the focal plane. c) Fitted super-Gaussian orders and percentage of beam intensity within the focus ROI about the beam centre for each of the four truncated fields. d) Intensity profile at the focus for fields propagated between truncated limits 1 (magenta) and 4 (black).

The target super-Gaussian of order $P = 2$ with a flat phase front at the focal plane of a lens, and the field at the back focal plane such that the planes are in an $f - f$ arrangement, are shown in figure 5.7a and b respectively. It is observed that the field required at the back focal plane is a Bessel-like structure in intensity and a repeated π -step in phase for intensity lobes outside the beam centre. Practically there is a limit to the size of the SLM that can be used in a shaping experiment.

Figure 5.7c shows that there is little benefit for an SLM that is large enough to include more than 2 lobes, where the loss of integrated intensity is $< 1\%$. To obtain the Bessel-like intensity profile required at the SLM a second adaptive optic may be introduced.

5.7 Dual element adaptive optics

This section will discuss shaping with two adaptive optics elements. Due to COVID restrictions experimental work on dual AO shaping at Swansea University was not possible. Simulation work has taken place of what would have been performed experimentally. A discussion on dual-element adaptive optics for applications in high-order harmonic generation is included in chapter 6.

5.7.1 Dual deformable mirrors

Dual DMs are commonly arranged in ‘Woofers-Tweeters’ configurations where the first and second DM compensate respectively for low and high order aberrations [99, 141]. These systems have been used to remove wavefront aberrations in applications such as STORM microscopy and in-vivo biomedical imaging [106, 142]. Lei et al. used a Woofer-Tweeter system controlled by a gradient descent algorithm which used the Strehl ratio, S_r , as a cost function [143]. S_r has a value between 0 and 1 where 1 is given for a beam with no aberrations [144]. Lei et al. evaluated $S_r = 0.74$ with a single DM and $S_r = 0.95$ using dual DMs. They also recorded an energy loss between the initial beam and the beam at the far field to be 16%.

5.7.2 One deformable mirror and one spatial light modulator

Beam shaping with ultrafast pulsed lasers requires a degree of control over the phase front and the pulse front. Although dual DM systems offer good control over the pulse front, there is always concomitant phase front distortions which may not be

desirable in some applications. Section 2.2.4 details how pulse fronts and phase fronts slip when passing through any material. Sun et al. demonstrated that a dual AO system with a DM and an SLM offered decoupled control over both the pulse fronts and phase fronts to compensate for phase front distortions and generate tailored beam profiles [66]. Controlled by phase-retrieval algorithms, Nei et al. have shown that this type of AO system can be used to generate flattop beam profiles from an input Gaussian [145].

5.7.3 Dual spatial light modulators

In 1998 Kelly et al. showed that a greater phase aberration correction could be achieved using a dual SLM system as opposed to a single SLM [146]. Multiple studies have since been made into the use of dual SLM systems for beam shaping and other applications such as vortex beam generation [147, 148]. Ma et al. showed examples of dual SLM systems that have been used for converting transverse Gaussian beams into flattop profiles. This research includes demonstrations of dual SLMs controlled by gradient decent or SA algorithms [149, 150]. One of the disadvantages of dual SLMs is the increased loss of light from diffraction as discussed in section 5.3. Ma et al. (2010) highlight that the power lost between an initial quasi-Gaussian beam and the shaped top-hat profile is on the order of 29% [151, 152].

5.7.4 Dual element shaping with a Gerchberg Saxton algorithm

This section aims to investigate the feasibility of shaping using two adaptive optics elements for HHG based on the schematic in figure 6.3. At the gas target an ideal super-Gaussian of $P = 2$, width $w_0 = 90 \mu\text{m}$ and a flat phase profile is propagated back to the SLM via a Fourier transform as described in section 2.2.4. This gives the ideal target field at the back-focal plane of the lens. Between the two AO elements the ASM propagation method is used to propagate a distance $z = 500 \text{mm}$. It is assumed that the input driver beam incident on the first AO element is a collimated

Gaussian with a flat phase, and the aperture diameter of both AO elements is 13 cm.

The Gerchberg-Saxton (GS) is an iterative algorithm that is used to retrieve the phase needed between planes of known intensity profiles as represented by the flowchart in figure 5.8. In figure 5.8 the first AO element is at plane 1 and the second AO element is at plane 2. On the first iteration the field of a known intensity profile (here it is a collimated Gaussian) is propagated from the first to the second plane with a guessed phase profile. At the second plane the intensity profile is replaced with the target profile and propagated back to the first plane. Here, the intensity profile is again replaced with the Gaussian intensity profile. This continues until the algorithm either converges or the maximum number of iterations is reached.

The GS algorithm was used to retrieve the phase required at the first AO element to create the intensity profile at the second element [153–156]. At the second AO element the ideal phase to generate super-Gaussian profile $P = 2$ at the focal plane is transversely imprinted on the beam and propagated to the front focal plane of the lens. The results from the GS are shown in figure 5.9. For the beam profile created by the GS at the gas target the intensity maintained within the $1/e^2$ width is 79.6%.

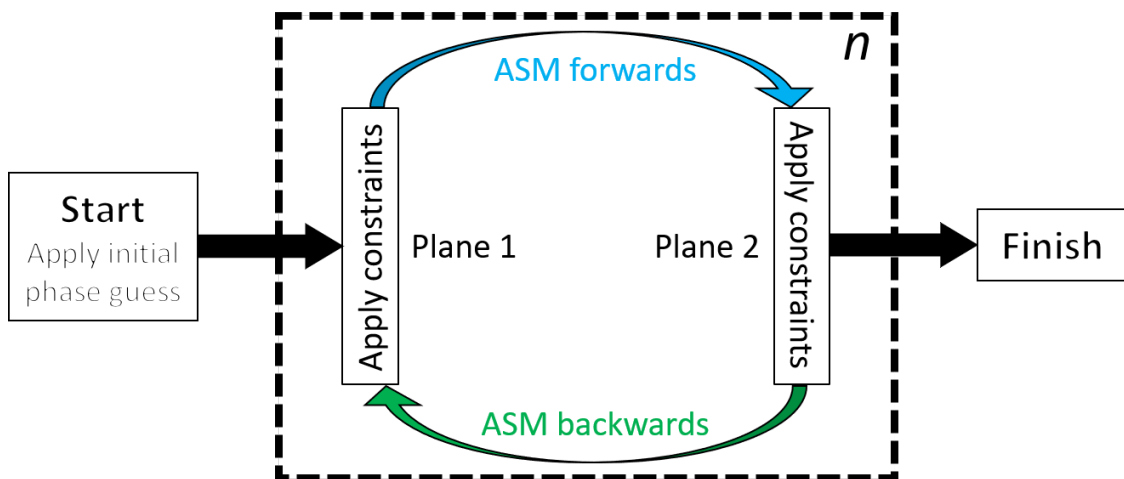


Figure 5.8: Flowchart describing the Gerchberg-Saxton algorithm between two planes. The angular spectrum method (ASM) is used to propagate between these planes separated by $z = 500$ mm. Constraints are made by replacing the acquired with the target intensity profiles at each plane. The algorithm finishes after n iterations.

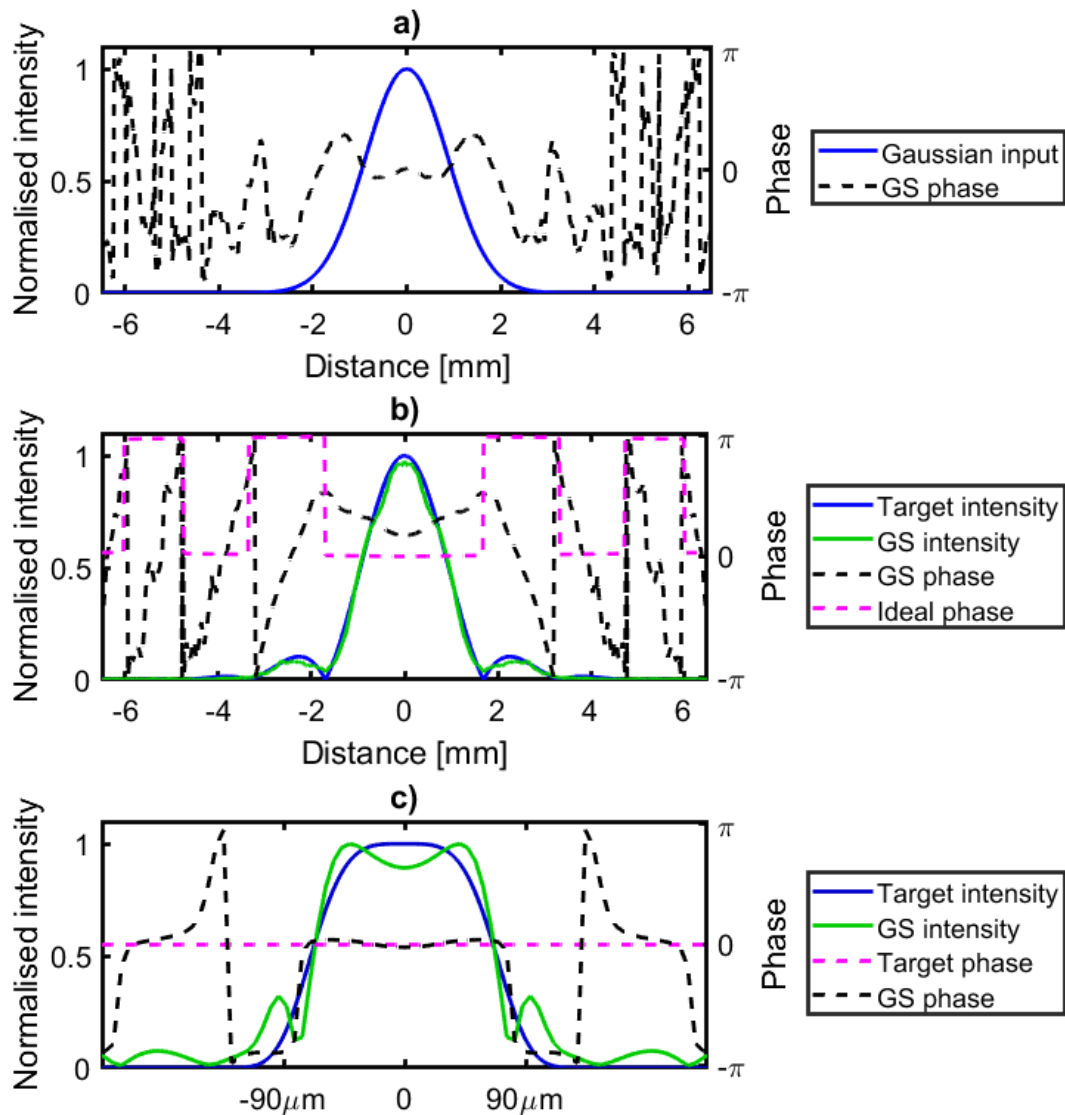


Figure 5.9: Dual element shaping results from a Gerchberg-Saxton (GS) algorithm. a) The input Gaussian and phase required at the first shaping element. b) The target and GS intensity profile at the second shaping element. c) The target intensity and phase at the focus. The GS field (green and blue) is propagated from the second shaping element with the GS intensity and the ideal phase.

Chapter 6

Driving HHG with tailored fields

"Onwards and upwards."

Oliver Heath

In this chapter the simple dipole model (SDM) and Lewenstein model are compared and used to simulate high-order harmonic generation (HHG) with shaped driver beam profiles. These models offer a more accurate description than Corkum's three step model as described in chapter 2. To investigate the effect of shaping the transverse intensity profile of the driving laser on the generated harmonic beam, simulations have been performed for an adaptive optics system. The fringe visibility has been calculated as a measure of coherence of the harmonic fields for multiple super-Gaussian drivers. For convenience, atomic units are used in throughout this chapter such that: the reduced Planck's constant, $\hbar = 1$, electron charge, $e = 1$, electron mass $m_e = 1$, Bohr radius, $a_0 = 1$, energy, $27.21 \text{ [eV]} = 1$, time, $1 \text{ [fs]} = 41$, and the angular frequency for a 800 nm wavelength is $\omega = 0.057 \text{ [157, 158]}$.

6.1 The Lewenstein model of HHG

Although the three-step model is intuitive it cannot adequately describe the HHG process which is quantum in nature. The interaction between an atom and a linearly polarised laser field, $\mathbf{E}(t)$, can be described by the time-dependent Schrödinger equation (TDSE),

$$i\frac{\partial}{\partial t}\psi(\mathbf{r}, t) = \left[-\frac{1}{2}\mathbf{p}^2 + V(\mathbf{r}) - \mathbf{E}(t)\cdot\mathbf{r} \right] \psi(\mathbf{r}, t), \quad (6.1.1)$$

with wavefunction $\psi(\mathbf{r}, t)$, momentum \mathbf{p} , and the atomic potential $V(\mathbf{r})$. The TDSE can be solved numerically however it can be difficult to physically interpret the results with this treatment [26, 69]. The Lewenstein model [159] offers an alternative semi-classical approach which is based on the strong field approximation (SFA) [67, 73, 160–166]. Within this model the three assumptions are:

- The contribution from all of the excited states (above the ground state $|\psi_0\rangle$) are neglected.
- The motion of the electron in the continuum is independent of the atomic potential due to the strong field. This is the strong field approximation.
- The depletion of the ground state is negligible.

The latter can only remain true if the driving laser has intensity less than the saturation intensity such that most electrons remain in their bound state. The first two assumptions are generally true providing that the Keldysh parameter,

$$\gamma = \sqrt{\frac{I_p}{2U_p}} < 1. \quad (6.1.2)$$

This is the tunnelling-ionization regime as described in section 2.3.1 [68, 159, 164]. Using the assumptions and conditions above an analytical expression for the time dependent dipole moment of a single atom will be shown. The first step is to consider a driving laser pulse which is linearly polarised such that,

$$\mathbf{E}(t) = E_x(t) \quad \text{and} \quad \mathbf{d}(\mathbf{p}) = d_x(\mathbf{p}), \quad (6.1.3)$$

and the intensity duration, t_{FW} , is determined by its full-width at half-maximum (FWHM). The electric field is given by,

$$E(t) = E_0 \exp\left(-\frac{2 \ln 2}{t_{\text{FW}}^2} t^2\right) \cos(\omega t). \quad (6.1.4)$$

To remain consistent with Lewenstein *et al.* [159] let the birth (ionization), recombination and continuum times be referred to as t' , t and t'' respectively and let τ be such that $\tau = t - t'$. The time-dependent dipole moment in the x -direction is,

$$\begin{aligned} \langle x(t) \rangle = & i \int_0^\infty d\tau \int_0^\infty d^3p E(t - \tau) d(p - A(t - \tau)) \\ & \times \exp(-iS(p, t, \tau)) d^*(p - A(t)) + c.c. \end{aligned} \quad (6.1.5)$$

The integrand can be written as the product of three distinct functions such that,

$$\langle x(t) \rangle \approx \int_0^\infty a_{\text{ion}}(t, \tau) \times a_{\text{prop}}(t, \tau, p_s) \times a_{\text{recom}}(t, p_s) d\tau + c.c. \quad (6.1.6)$$

In this intuitive form $a_{\text{ion}}(t, \tau)$, $a_{\text{prop}}(t, \tau, p_s)$ and $a_{\text{recom}}(t, p_s)$ represent the semi-classical ionization, propagation and recombination probability amplitudes which are described in Corkum's three step model. Within equation 6.1.5 the vector potential of the driving laser field, $A(t)$, is given such that,

$$E(t) = -\frac{\partial A(t)}{\partial t}, \quad (6.1.7)$$

for any time, t . The canonical momentum is represented by p , $d(k)$ is the atomic dipole matrix element between the bound state and continuum state with momentum $k = p - A(t)$, and S is the quasi-classical action of the ionized electron where the phase accumulated by the electron in the continuum is equal to $\exp(-iS(p, t, t''))$. The path integral over all p is replaced by applying a saddle-point approximation (Appendix: A2) [26].

The following three subsections will now outline the details to calculate each probability amplitude as shown in equation 6.1.6.

6.1.1 Ionization

Amplitude a_{ion} represents the transition of the electron from the bound state into the continuum. This occurs at time $t - \tau$ and with momentum, p , such that,

$$a_{\text{ion}}(t, \tau) = E(t - \tau)d(p - A(t - \tau)). \quad (6.1.8)$$

Within the tunnelling-ionization regime with $\gamma < 1$, the Ammosov-Delone-Krainov (ADK) model for ionization can be utilised [73, 167]. The rate of ionization is described by,

$$\omega_{\text{ADK}}(t) = I_p |C_{n^*}|^2 \left(\frac{2(2I_p)^{\frac{1}{2}}}{E(t)} \right)^{2n^*-1} \exp \left(-\frac{2(2I_p)^{\frac{3}{2}}}{3E(t)} \right), \quad (6.1.9)$$

where the principal quantum number is given by, $n^* = Z/\sqrt{(2I_p)}$, and Z is the degree of ionization. $C_{n^*} \approx 2$ accounts for the atomic species and initial electronic configuration. Given an initial gas-density, n_0 , equation 6.1.9 can be used to calculate the free-electron density, $n(t)$, which is defined as,

$$n(t) = n_0 \left(1 - \exp \left[-\int_{-\infty}^t dt' \omega_{\text{ADK}}(t') \right] \right). \quad (6.1.10)$$

With a known free electron density the amplitude, a_{ion} , is given by,

$$a_{\text{ion}}(t, \tau) = \sqrt{\frac{dn(t - \tau)}{dt}}. \quad (6.1.11)$$

6.1.2 Propagation

Under the influence of the strong laser field the quasi-classical action, S , describes the path of the free electron with constant momentum, p , as described by,

$$p = v + A(t''), \quad (6.1.12)$$

recalling that this definition of p applies only to the momentum in the continuum.

The action is therefore described by,

$$S(p, t, \tau) = \int_{t-\tau}^t dt'' \left[\frac{(p - A(t''))^2}{2} + I_p \right]. \quad (6.1.13)$$

The integral over all p is carried out by using a saddle-point approximation which is an extension of Laplace's method. This means that the main contribution to the propagation amplitude is from about the points of least action, i.e. for the stationary momentum values. These points are given by,

$$\nabla_p S(p, t, \tau) = \int_{t-\tau}^t \frac{dt''}{dp} \left[\frac{(p - A(t''))^2}{2} + I_p \right], \quad (6.1.14)$$

$$= \int_{t-\tau}^t dt'' [(p - A(t''))], \quad (6.1.15)$$

which from equation 6.1.12 becomes,

$$\begin{aligned} \nabla_p S(p, t, \tau) &= \int_{t-\tau}^t dt'' v(t''), \\ &= x(t) - x(t - \tau), \\ &= 0. \end{aligned} \quad (6.1.16)$$

The dominant electron paths therefore come from the electrons that return to their parent ions. The stationary momentum values can then be obtained by using equations 6.1.15 and 6.1.16,

$$\int_{t-\tau}^t dt'' [(p_s - A(t''))] = 0, \quad (6.1.17)$$

$$\int_{t-\tau}^t dt'' p_s = \int_{t-\tau}^t dt'' A(t''), \quad (6.1.18)$$

which yields the saddle points,

$$p_s(t, \tau) = \frac{1}{\tau} \int_{t-\tau}^t dt'' A(t''). \quad (6.1.19)$$

The phase that the electron accumulates is given by $\exp(-S(p_s, t, \tau))$. With a pre-factor to compensate for the quantum spread of the electron-wavepacket, the propagation amplitude is then given by,

$$a_{\text{prop}}(t, \tau, p_s) = \left(\frac{2\pi}{i\tau}\right)^{\frac{3}{2}} \exp(-S(p_s, t, \tau)). \quad (6.1.20)$$

6.1.3 Recombination

The amplitude for the recombination of the electron-ion pair at time t is given by,

$$a_{\text{recom}}(t, p_s) = d^*(p_s - A(t)). \quad (6.1.21)$$

Here there is a contribution from the ground state and the returning electron wave-function. The interaction between these states is the only contributors to HHG. The returning wave-function is treated as a plane wave such that,

$$a_{\text{recom}}(t, p) \propto \int \psi_0 x \exp(ipx) dx, \quad (6.1.22)$$

where ψ_0 represents the ground state. For hydrogen-like atoms, the free dipole matrix element is approximately,

$$a_{\text{recom}}(t, p_s) = i \frac{2^{\frac{7}{2}} (2 I_p)^{\frac{5}{4}}}{\pi} \frac{p_s}{(p_s^2 + (2 I_p))^3}. \quad (6.1.23)$$

6.1.4 HHG spectra

The spectra of HHG across odd harmonics where $w_q = qw_0$, has a distinctive decline for low-order harmonics, followed by a plateau region where the intensity variation is minimal, followed by a second decline as defined by the cutoff region described in the three step model from equation 2.3.11. The scaling of the cutoff region in the three step model is also observed in the SFA. The intensity spectrum of HHG

is given by [26],

$$I(\omega) \propto \left| \int \langle x(t) \rangle \exp(i\omega t) dt \right|^2. \quad (6.1.24)$$

Using the SFA the single-atom HHG spectra is shown in figure 6.1 where $E_{\text{cutoff}} \propto I_{\text{max}}$ can be observed.

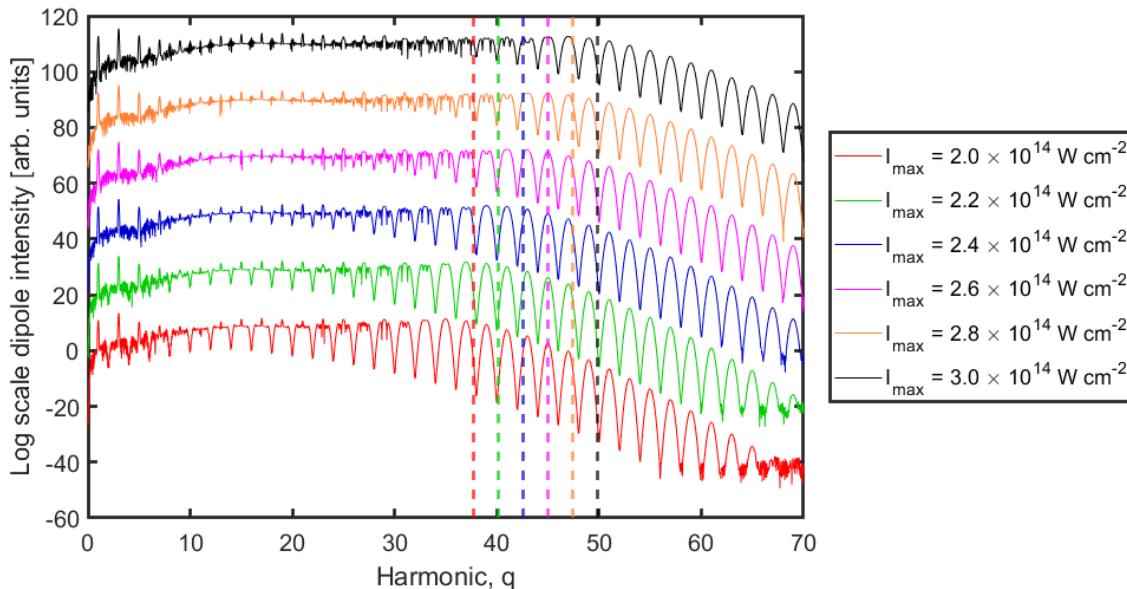


Figure 6.1: Single atom HHG spectra calculated using the SFA for argon for multiple peak driver intensities, I_{max} . The dotted lines show the cutoff energies calculated from the three step model and each spectrum has been vertically offset for clarity. The driver wavelength is 800 nm with a pulse duration of 40 fs FWHM.

6.1.5 SFA benchmarking

The spectra from the single-atom SFA were benchmarked against examples in literature and found to give good agreement by visibly comparing the location of the harmonic peaks and the cutoff harmonic between figures from [26,72,74,168,169], using the like-for-like parameters: maximum driver beam intensity, driver beam width, driver wavelength pulse duration, gas ionisation energy, and propagation distance from the source.

The SFA was then used to calculate the HHG field at the focus of the driving laser for multiple atoms along a thin transverse plane. The HHG field was then propagated using the Hankel transform to the far field. Using like-for-like SFA

parameters the far field displayed in figure 6.2a gives good agreement with the spatially resolved HHG spectra from Catoire et al. as displayed in figure 6.2b [75].

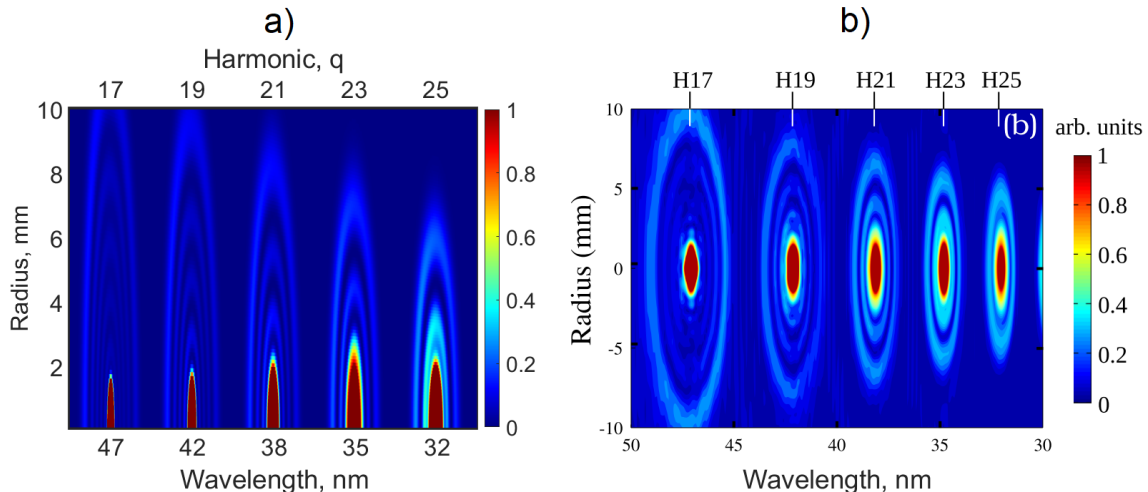


Figure 6.2: a) Intensity-normalised far-field harmonic spectra calculated using the SFA. The peak intensity is $I_{\max} = 2 \times 10^{14} \text{ Wcm}^{-2}$, the Gaussian pulse width is 40 [fs] FWHM, the transverse IR driver is a Gaussian of waist size $120 \mu\text{m}$, the driver wavelength is 800 nm, and the source-detector distance is 3 m. b) Results of the SFA from Catoire et al. for the same parameters [75].

6.2 The simple dipole model

An alternative method to describe HHG is the simple dipole model (SDM). The SDM is a simplified model that is more easily interpreted than the SFA, whilst containing most of the same features as the SFA. Within this section the key features of the SDM will be discussed showing how the behaviour of the harmonic field divergence changes with the driver beam intensity profile, particularly the dependence on harmonic beam width w_q at the generation plane, with super-Gaussian order P . According to the SDM the harmonic dipole is described by,

$$d_q(r) = I_{\text{IR}}^{\frac{q_{\text{eff}}}{2}}(r) \exp[i(q\phi_{\text{IR}}(r) + \phi_{\text{atom}}(r))], \quad (6.2.1)$$

where $I_{\text{IR}}(r)$ is the transverse intensity profile of the laser, q_{eff} is the effective non-linearity, q is the harmonic order, $\phi_{\text{IR}}(r)$ is the phase from the fundamental beam, and $\phi_{\text{atom}}(r)$ is the atomic dipole phase [48, 50, 75, 170, 171]. The atomic dipole phase is given by,

$$\phi_{\text{atom}}(r) \approx U_p \tau \approx -\alpha_q^j I_{\text{IR}}(r), \quad (6.2.2)$$

where α_q^j depends on the electron transit time and is different for the long ($j = l$) and short ($j = s$) trajectories [172]. For long trajectories, $t - t' \approx 2\pi/w$, and the estimate for α_q^l is given by $\pi/2w$ which is $24 \times 10^{-14} \text{ cm}^2 \text{ W}^{-1}$. For short trajectories the estimate for α_q^s is about four times smaller at $6 \times 10^{-14} \text{ cm}^2 \text{ W}^{-1}$ [75]. Rewriting equation 6.2.1, the SDM in the form of the sum between the two trajectories is,

$$d_q(r) = \sum_{j=l,s} A_j I_{\text{IR}}^{\frac{q_{\text{eff}}}{2}}(r) \exp[-i \alpha_q^j I_{\text{IR}}(r)] \exp[q\phi_{\text{IR}}(r) + \Delta\phi_j], \quad (6.2.3)$$

where A_j are the amplitudes from the long and short trajectory components, and $\Delta\phi_j$ is the difference phase difference between the long and short trajectories [75]. At the harmonic generation plane the driver laser imprints a phase on the harmonic field equal to,

$$\phi_{\text{IR}}(r) = \frac{\pi r^2}{\lambda R(z)}, \quad (6.2.4)$$

where $R(z)$ is the radius of curvature. The SDM yields the following expression which shows that the harmonic source size scales with q_{eff} ,

$$I_q(r) \propto \exp \left[-2 q_{\text{eff}} \left(\frac{r^2}{w_0^2} \right)^P \right], \quad (6.2.5)$$

where P is the super-Gaussian order and w_0 is the $1/e^2$ radius of the driving beam. From equations 6.2.5 and 2.1.1 the P -dependent width of the harmonic source is given by [50, 170],

$$w_q^P = \frac{w_0}{\sqrt[2P]{q_{\text{eff}}}}. \quad (6.2.6)$$

6.3 HHG model beamline

In this section HHG is simulated using laser and beamline parameters typically available in research laboratories in order to mimic practical experiments. A typical HHG beamline consisting of a dual-element AO system is illustrated in figure 6.3 [48, 139]. Here a driving laser is spatially shaped by the AO system before being focused onto a gas target. Harmonics generated in the gas target are detected downstream by an x-ray CCD or spectrometer. In order to simulate the HHG beam at the detector it is necessary to consider both the propagation of the IR driving beam and the generated XUV beam. The following three distinct sections must be considered:

1. The propagation of the IR field between the two AO elements, where the ASM will be utilised.
2. The propagation of the IR field between the second element and the gas cell, where the Fourier transform properties of a lens as discussed in section 2.2.4 can be employed if the second AO element and gas cell are one focal length away from the lens. At the plane of the gas cell the SFA is then used to calculate the harmonic field.
3. The propagation of the harmonic field between gas cell and the detector, where assuming cylindrical symmetry the Hankel transform will be utilised.

Within this chapter only spatial shaping effects are considered. The SFA and SDM are used to create the harmonic field at the gas cell where the single atom response is calculated across the transverse plane. The harmonic field is generated by calculating $\langle x(r) \rangle$ over the entire Gaussian pulse and for each radial position as illustrated in figure 6.4. For the remainder of this chapter the values in table 6.1 are used for HHG simulations. From equation 2.1.2 different orders of super-Gaussians of the same width have different peak intensities. To practically maintain the same I_{\max} a wave plate and a polariser may be placed before the gas target.

Table 6.1: HHG simulation parameters [165,173].

Parameter	Value
Driver wavelength, λ	800 nm
Driver radius, w_0	$90 \mu\text{m}$
Driver maximum intensity, I_{max}	$2 \times 10^{14} \text{ W cm}^{-2}$
Pulse duration, τ	40 fs
Gas (Ar) ionization energy, I_p	15.759 eV

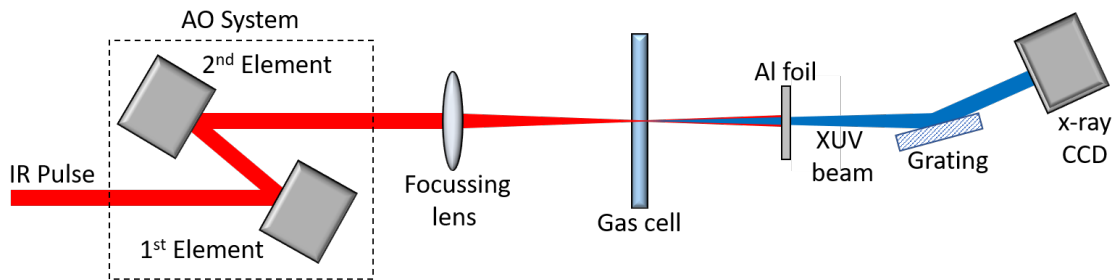


Figure 6.3: Schematic of a typical harmonic beamline including an AO system. An IR driving pulse is shaped by an adaptive optics system and focused to a gas target where harmonics are generated. An aluminium foil only allows the XUV beam through to a grating. A detector such as a CCD then measures these harmonics further along the beamline.

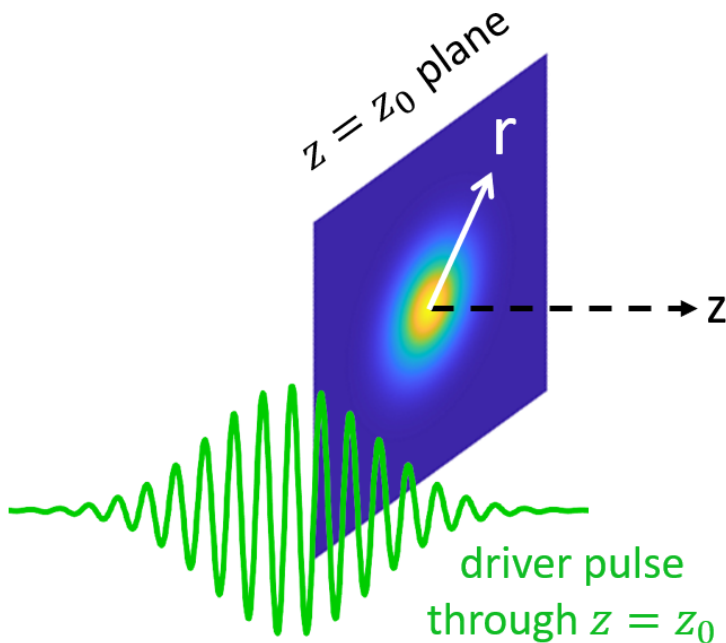


Figure 6.4: An illustration of harmonic generation at the gas target for a single infinitesimal plane. The harmonic spectrum is simulated at the generation plane by calculating the dipole over the Gaussian pulse (green) in time, the transverse profile as a function of radial distance in space. The field is then propagated in the z -direction down the beamline.

6.4 Beam shaping for HHG

Simulations have been performed using the SDM and SFA to investigate the effects of using a driver laser with transverse intensity profiles of increasing super-Gaussian order. The practical benefit of super-Gaussian shaping using adaptive optics to lower divergence is the ability to irradiate smaller volumes of interest, and increase brightness [50]. Super-Gaussians drivers are also more efficient for HHG as there is more energy in the central region of the beam where the intensity is above the threshold for generating high harmonics. The two areas of investigation presented are the HHG beam divergence and coherence that are of interest for applications such as coherent diffractive imaging. The divergence of a beam,

$$d \propto \frac{z\lambda}{w_0}, \quad (6.4.1)$$

where z is the propagation distance, λ is wavelength and w_0 is the source size [174]. From equation 6.2.6 the source size of HHG increases with super-Gaussian order, P . The divergence is therefore expected to decrease with increased P . Equation 6.2.6 describes the harmonic source width dependence on P and is displayed in figure 6.5. This figure shows that increasing P yields diminishing returns for reducing beam divergence. The differential of the P -dependence also shows that experimentally the size of the harmonic source would be the most sensitive to changes in super-Gaussian order about $P \approx 1.8$. The divergence of the HHG beam was investigated by calculating the far-field spatial intensity distribution for a range of super-Gaussian transverse laser intensities. An example intensity distribution about harmonic $q = 23$ is given figure 6.6 for driver orders $P = 1$ through $P = 2$. The width of the generated harmonics at the detector plane was determined using the second moment method as described in section 2.1.2.

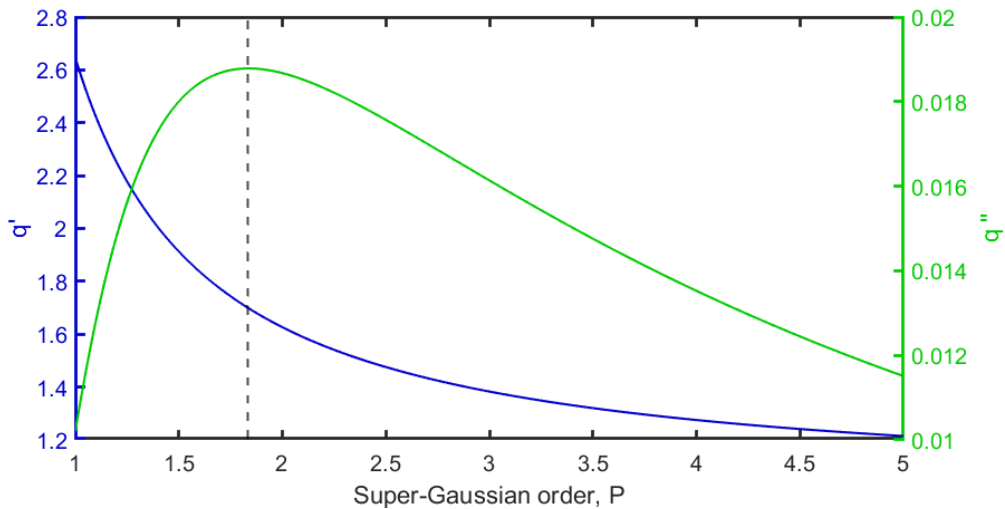


Figure 6.5: Variation of the harmonic size with super-Gaussian order using the denominator in equation 6.2.6 from the simple dipole model. $q' = \sqrt[2P]{q_{\text{eff}}}$, $q'' = \frac{d}{d(2P)} \sqrt[2P]{q_{\text{eff}}}$ (with a peak at $P = 1.835$), and $q_{\text{eff}} = 6.99$.

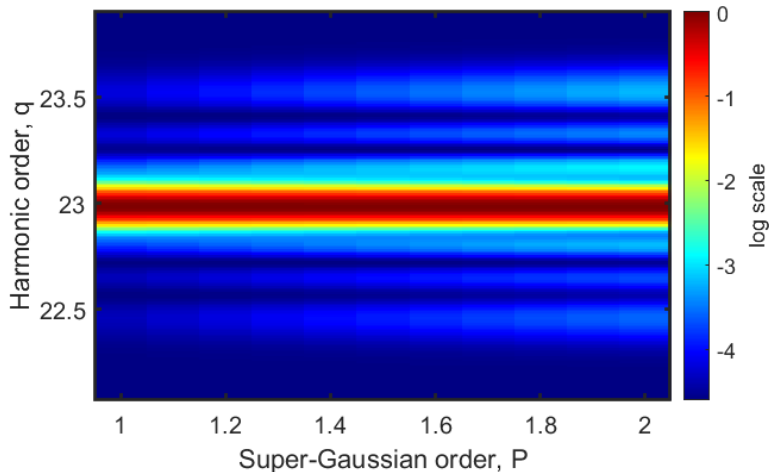


Figure 6.6: Intensity distribution at the far field for multiple driver beam super-Gaussian orders about $q = 23$ calculated from the SFA.

6.4.1 Calculating divergence using the SFA and SDM

The HHG fields calculated using the SFA and SDM were propagated 3 m to the far-field using a Hankel transform.

The SDM was seeded with the far-field second moments of $q = 25$ that was calculated from the SFA. MATLAB's least-squares fit was used to numerically obtain

Table 6.2: Simple dipole estimated parameters.

Parameter	Value
A_{long}	0.4005
A_{short}	0.5995
ϕ_j	0.98 [rad]
q_{eff}	6.99

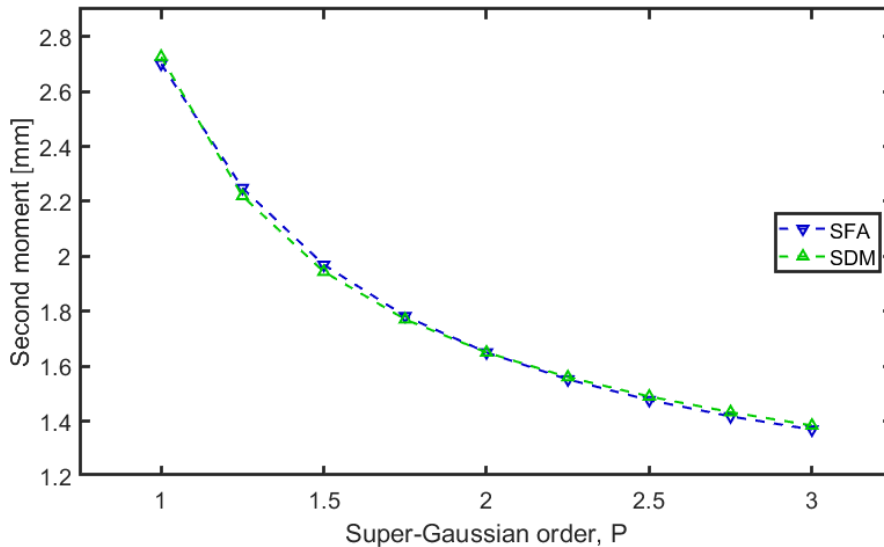


Figure 6.7: The second moments calculated from the simple dipole model (SDM) and the strong field approximation (SFA) at propagation distance $z = 3$ m from the source, for $q = 25$. The SDM fitting parameters can be found in table 6.2 and the driver beam parameters are given in table 6.1.

estimate values for the parameters A_{long} , A_{short} , ϕ_j and q_{eff} , as required for equation 6.2.3. These values are displayed in table 6.2.

For orders $P = 1$ through $P = 3$ figure 6.7 shows good agreement between the SFA and SDM models for $q = 25$. Using the SDM parameters from table 6.2 the second moments were calculated for a range of harmonics about the cutoff $q = 37$. Figure 6.8 shows that in both models the divergence decreased with super-Gaussian order with an expected greater rate of change between $P = 1 \rightarrow 2$. There is however a disagreement in the second moments which is particularly noticeable for $23 \leq q \leq 33$. This may be a consequence of using second moments to calculate widths when the peaks of the transverse profile overlap in the SFA, or due to tuning to only a single harmonic, $q = 25$, in the SDM, or due to other more complex details

in the SFA model.

To probe the behaviour of the long and short trajectories, the SDM was chosen to isolate their contributions to the far-field intensity profile about $q = 23$ as shown in figure 6.9. Here the second moments for both trajectories are seen to decrease with P , with a more rapid decrease for the long trajectories. For long trajectories with low intensities, figure 6.9 c) shows a subtly diverging region which is also present in the SFA shown in figure 6.10, where the outer rings become fainter with P . The dashed lines in figure 6.10 indicate the second moment values from the SDM. This shows that the central ring is mostly from the short trajectory component, and has approximately the same divergence as a Gaussian beam of size equivalent to the size of the HHG source.

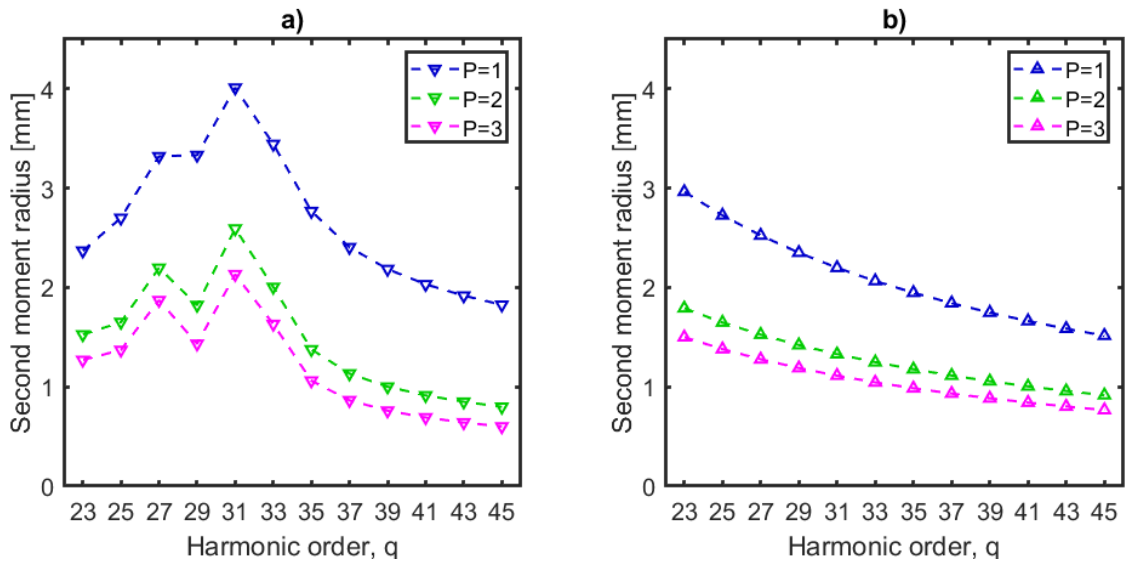


Figure 6.8: Second moments against harmonic order for super-Gaussian order $P = 1, 2, 3$, for a) the strong field approximation, and b) the simple dipole model. The driver beam parameters are given in table 6.1 and the propagation distance is 3 m. The cutoff harmonic is at $q = 33$.

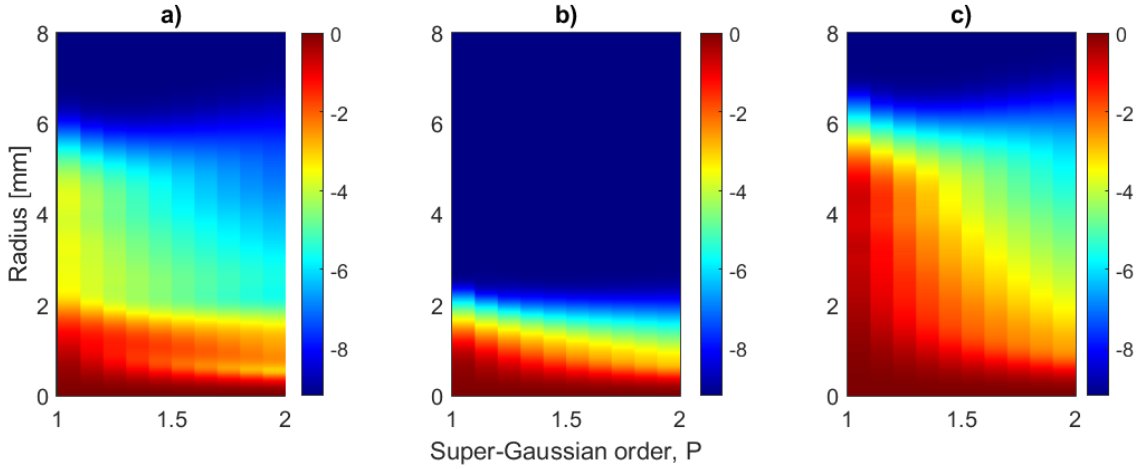


Figure 6.9: Log scale radial transverse intensity profile for harmonic $q = 23$ against super-Gaussian order, P , calculated from the simple dipole model (SDM). SDM parameters are given in table 6.2. a) long and short trajectory contributions, b) short trajectory only, c) long trajectory only. The intensity profiles have been normalised for each super-Gaussian order. The driver beam parameters are given in table 6.1 and the propagation distance is 3 m.

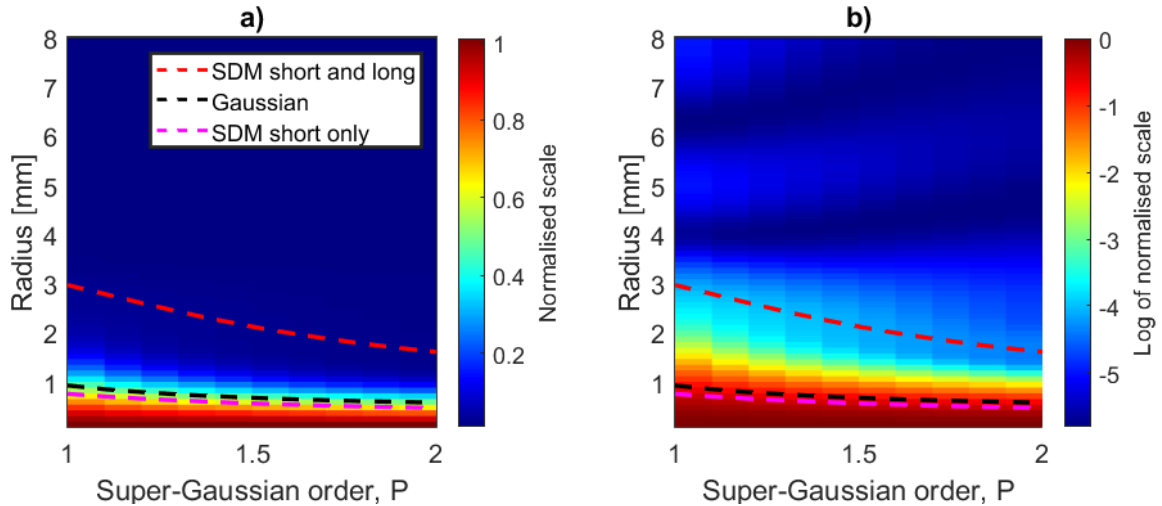


Figure 6.10: Radial transverse intensity profile for harmonic $q = 23$ against super-Gaussian order, P , calculated from the strong field approximation. The red dashed lines are the second moments from the long and short trajectory contributions from the simple dipole model (SDM), the black dashed lines are the Gaussian-equivalent beam size using equation 6.2.6, the magenta dashed lines are the second moments from the short-only trajectory contributions using the SDM.

6.4.2 Dual adaptive optics for HHG

This section uses the shaping results from the dual element system in section 5.7 to drive HHG.

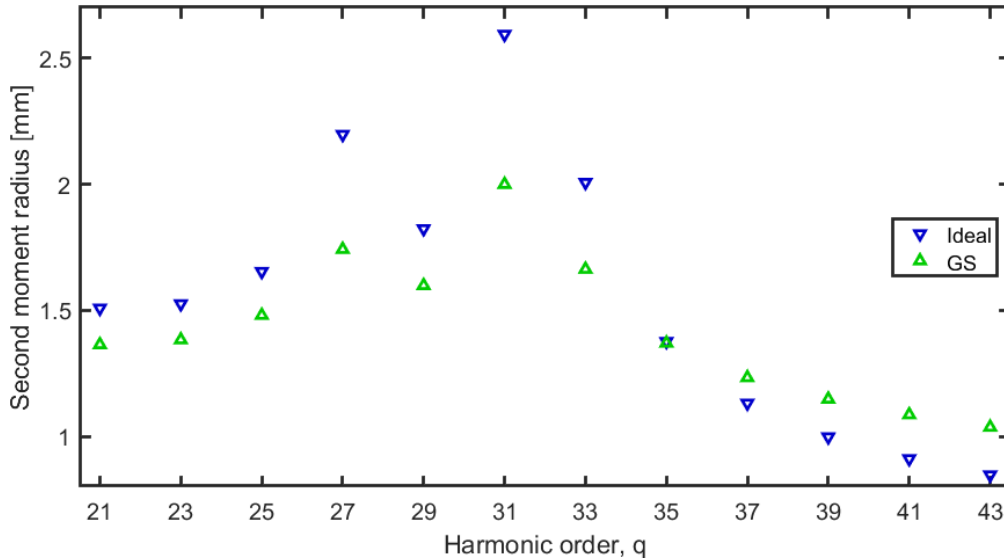


Figure 6.11: Second moments for harmonics 21 through 43 using the ideal super-Gaussian, $P = 2$, and the field generated by a Gerchberg-Saxton algorithm. Propagation distance from the generation plane is $z = 3$ m.

The SFA was used to calculate the HHG field using the driver field generated by the GS in figure 5.9c to give a realistic expectation of experimental results. At the far field the second moments were calculated and compared to the ideal $P = 2$ super-Gaussian. From figure 6.11, although the ideal field has higher second moments for harmonics up until the cutoff $q = 37$, the second moment values are still in a close agreement. A practical benefit of a dual-element shaper with either phase retrieval or other learning algorithms could be the ability to create such super-Gaussian profile with increased control over beam aberrations.

6.4.3 Spatial coherence and fringe visibility

Lastly the effect of beam shaping on spatial coherence will be considered. Perfect spatial coherence implies a fixed phase relationship across the beam profile, and is an ideal property in applications such as coherent diffractive imaging. Considering a

one dimensional electric field, $E(x, t)$, the aim is to calculate the degree of correlation between two spatially separated points, x_1 and x_2 . To do this we use the mutual coherence function (MCF). With zero time delay between x_1 and x_2 the MCF is defined by [155,175],

$$M(x_1, x_2, \tau = 0) = \langle E(x_1, t + \tau)E(x_2, t)^* \rangle. \quad (6.4.2)$$

The intensity integrated over time is,

$$I(x) = \langle |E(x, t)|^2 \rangle. \quad (6.4.3)$$

For $\tau = 0$ the intensity from the MCF is,

$$M(x_1, x_1, 0) = I(x_1), \quad (6.4.4)$$

$$M(x_2, x_2, 0) = I(x_2), \quad (6.4.5)$$

and when evaluated is referred to as the mutual intensity and denoted by J_{12} . The normalisation of the mutual intensity is given by,

$$\mu = \frac{J_{12}}{\sqrt{I(x_1)I(x_2)}}. \quad (6.4.6)$$

x_1 and x_2 can be thought of as the transverse locations of two pinholes. At the detection plane with spatial co-ordinates of X ,

$$E(X, t) = \alpha E(x_1, t) + \beta E(x_2, t), \quad (6.4.7)$$

where α and β account for the propagation of the fields from both pinholes. From equation 6.4.3, at the far-field diffraction pattern is given by,

$$I(X) = \langle |E(X, t)E(X, t)^*|^2 \rangle, \quad (6.4.8)$$

$$= |\alpha|^2 I(x_1) + |\beta|^2 I(x_2) + 2 \Re(\alpha\beta M(x_1, x_2)), \quad (6.4.9)$$

$$= I_1 + I_2 + 2 \Re(\alpha\beta J_{12}). \quad (6.4.10)$$

The maximum and minimum values of $I(X)$ are,

$$I_{\max} = I_1 + I_2 + 2\sqrt{I_1 I_2} |\mu|, \quad (6.4.11)$$

$$I_{\min} = I_1 + I_2 - 2\sqrt{I_1 I_2} |\mu|. \quad (6.4.12)$$

A convenient way to measure coherence is by the fringe visibility, V , of an interference pattern. The relationship between V and μ is given by [155, 175, 176],

$$V = \frac{2\sqrt{I_1 I_2}}{I_1 + I_2} |\mu|, \quad (6.4.13)$$

$$= \frac{I_{\max} - I_{\min}}{I_{\max} + I_{\min}}. \quad (6.4.14)$$

For different values of fringe visibility:

1. $V = 1$, implies perfect coherence,
2. $V = 0$, implies completely incoherent light, and
3. $0 < V < 1$, implies partially coherent light.

To determine if super-Gaussian drivers were more robust to intensity fluctuations the fringe visibility was calculated using different super-Gaussian orders, $P = 1, 2, 3$, for both a single and a 10-shot-averaged HHG field at the detector plane at $z = 1000$ mm, with a one percent noise value in the maximum driver intensity at the generation plane. At $z = 500$ two pinholes of diameter 0.32 mm were placed such that one was at the centre of the beam and the other was free to move transversely. The fringe visibility was calculated within the first lobe of the diffraction envelope.

Increasing the driver beam's super-Gaussian order increases the size of the harmonic source. From [177,178] increasing the source size can be thought of as adding additional point sources. The fringe pattern at the detection plane is made of the contribution of the wavefronts of all these point sources. moving the position of a point source shifts the location of the fringes. The light and dark fringes are localised about the regions on the detector plane where the optical path difference between two interfering wavefronts is small. Increasing the source size, and therefore the number of point sources, leads to these sources become more out of phase with one another and reduces the visibility of the fringes [177,178]. The decrease in fringe visibility with super-Gaussian order can be observed in figure 6.12a. It can also be observed that there was negligible difference in V between the single and 10-shot averaged fields for different super-Gaussian driver orders.

6.5 Discussion

The SFA and SDM have both shown that the divergence of the HHG beam decreased for increased driver order P . It has also been shown that the harmonic source size is most sensitive about $P \approx 1.8$. It was also observed that the super-Gaussian drivers had almost no effect on the fringe visibility calculations for single and 10-shot averaged fields. A dual AO system was modelled to show what could be achievable with such a system experimentally. The benefit of such a system could be increased shaping control to remove beam aberrations.

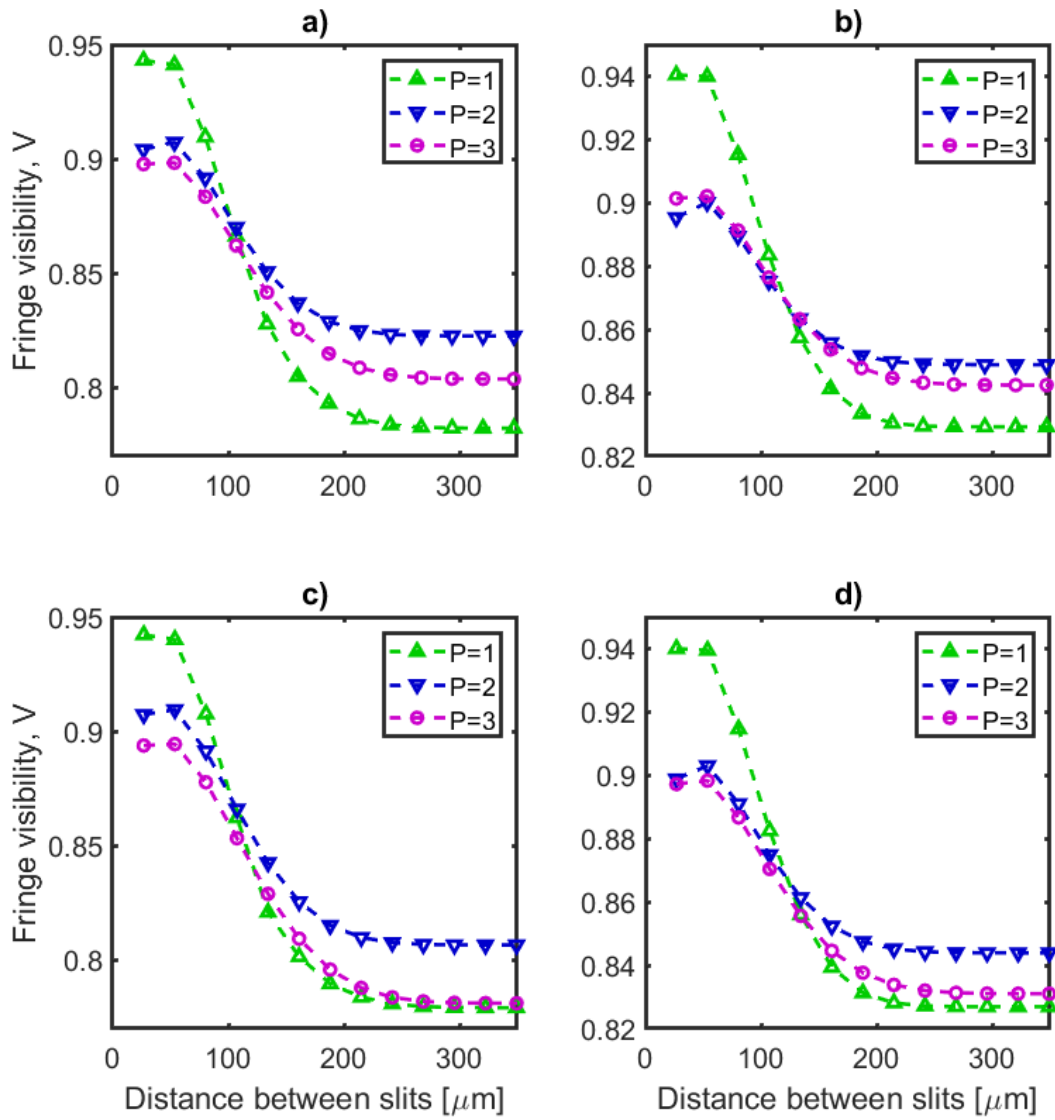


Figure 6.12: Fringe visibility against slit-slit distance for different super-Gaussian orders, P . a) and b) show the results for a single-shot exposure for $q = 23$ and $q = 27$ respectively. c) and d) show the results for an exposure averaged over 10 laser shots at the detector plane for $q = 23$ and $q = 27$ respectively.

Chapter 7

Conclusion

"That was a really good talk, you made it *look* like you've done a lot of work."

Phil John

7.1 Summary of thesis

This thesis has investigated beam shaping techniques to create super-Gaussian transverse intensity profiles. This has been performed experimentally using a deformable mirror, and through simulations of a phase-only spatial light modulator. The beam manipulation by these devices has been determined numerically by learning algorithms. Simulations were made of super-Gaussian driver beams for high-order harmonic generation (HHG), and the effects on HHG beam divergence and coherence have been investigated. The key results of each chapter are outlined below.

7.2 Results

In chapter 3 the performance of a random search algorithm (RSA), genetic algorithm (GA), simulated annealing algorithm (SA), and hybrid genetic-simulated annealing algorithm (HA), was compared for a simple 1D global maximisation problem. It was found that the reliability and success rate of each algorithm scaled with the algorithm complexity. In complexity order these were as follows: RSA, SA, HA,

GA.

In chapter 4 the SA, HA and GA were used to shape the Gaussian profile of a low-powered laser experimentally with a deformable mirror. All three algorithms were shown to be able to create super-Gaussians profiles of finely tuned orders $P = 1$ to $P = 2$ in $P = 0.1$ increments. The HA was found to offer a middle-ground between the SA and GA in terms of algorithm performance and difficulty of implementation.

In chapter 5 simulations were made of a phase-only spatial light modulator for super-Gaussian shaping using a known π -shift method as performed by Treacher et al. [50], a phase-step optimised SA as used by Fayyaz et al. [116], and the HA as created by this author. Here the SA outperformed the HA in terms of achieved super-Gaussian order. At higher orders, $P \approx 2.6$, the fitting error from the SA solutions showed that higher quality super-Gaussians may be achievable compared to the profiles using the π -shift method.

In chapter 6 the HHG process has been modelled using the strong field approximation and the simple dipole model and driven with super-Gaussians of orders $P = 1$ to $P = 3$. The HHG beam divergence was calculated using a second moment method. This was found to decrease with super-Gaussian order. The fringe visibility was calculated as a measure of HHG beam coherence. No discernible differences were found for the fringe visibilities of HHG beams generated by super-Gaussian drivers between single-shot and multi-shot pulses.

7.3 Future work

1. Further investigation into more complex algorithms such as neural networks may provide a significant improvement in the performance or runtime for beam-shaping experiments.
2. The dual AO system as demonstrated by [41] et al. has shown decoupled control of a laser beam's phase-front and wavefront. The deformable mirror and

spatial light modulator combination can be assembled and tested by adding aberrations from one element and removing these with the second element. These elements could both be driven by learning algorithms.

3. The dual AO system can be used to aim for target super-Gaussian orders up to $P = 2$ to compare with results in this thesis for a single-element (DM) shaper. Then the dual AO can be used to aim for target super-Gaussians of orders $P > 2$.
4. The dual AO system can be used on a HHG beamline such as Artemis at the Central Laser Facility to either optimise the complex profile of the driver beam, or to optimise from a different feedback method e.g. HHG beam divergence, brightness, or a single harmonic intensity at a detector plane.
5. The SFA code can be adapted to calculate the contributions from the long or short trajectories separately. This can then be compared with the results from the SDM.
6. The SFA and propagation codes can be adapted to calculate the harmonic field in a medium many atoms thick. This will lead to a model that will require phase-matching considerations.
7. The SFA and propagation codes can be made open source via Github.

Appendices

"Don't get sciencey on me."

Nina Mills

A1: Zernike polynomials

Even and odd Zernike polynomials of the respective forms,

$$Z_n^m \text{ even}(r, \theta) = R_n^m(r) \cos m\theta, \quad (7.3.1)$$

$$Z_n^m \text{ odd}(r, \theta) = R_n^m(r) \sin m\theta, \quad (7.3.2)$$

with radial polynomial,

$$R_n^m(r) = \sum_k^{\frac{n-m}{2}} \frac{(-1)^k (n-k)!}{k! \left(\frac{n+m}{2} - k\right)! \left(\frac{n-m}{2} - k\right)!} (r^{n-2k}), \quad (7.3.3)$$

are displayed up to Z_4^4 in figure 7.1. Table 7.1 displays the (m, n) values and common polynomial names [179].

Table 7.1: Common names for Zernike modes.

Noll index	m	n	Name
1	0	0	Piston
2	-1	1	Y-tilt
3	1	1	X-tilt
4	-2	2	Oblique astigmatism
5	0	2	Defocus
6	2	2	Vertical astigmatism
7	-3	3	Vertical trefoil
8	-1	3	Vertical coma
9	1	3	Horizontal coma
10	3	3	Oblique trefoil
11	-4	4	Oblique quadrafoil
12	-2	4	Oblique secondary astigmatism
13	0	4	Primary spherical
14	2	4	Vertical secondary astigmatism
15	4	4	Vertical quadrafoil

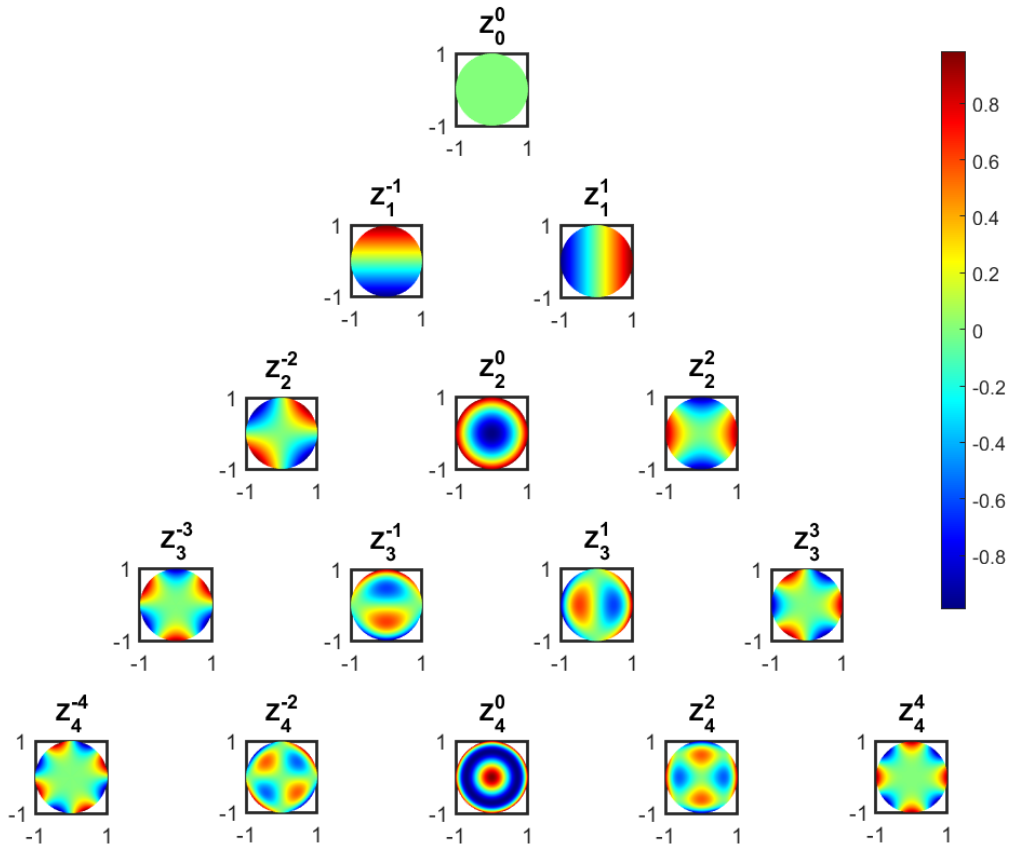


Figure 7.1: Z_n^m Zernike polynomials up to the 5th order. From [179].

A2: Stationary phase approximation

We start with an integral of the form,

$$I(\lambda) = \int_a^b f(t) \exp [i\lambda g(t)] dt, \quad (7.3.4)$$

where functions f and g can be approximated by a Taylor expansion about point $[a, b]$, and $\lambda \gg 1$. At some point c within $[a, b]$, $g'(c) = 0$ and $g'(c) \neq 0$ elsewhere in $[a, b]$. We assume $g''(c) \neq 0$ and $f(c) \neq 0$, and we define the sign of $g''(c)$ to be μ . Equation 7.3.4 can be rewritten such that,

$$I(\lambda) = \exp [i\lambda g(c)] \int_a^b f(t) \exp [i\lambda(g(t) - g(c))] dt. \quad (7.3.5)$$

$\exp [i\lambda(g(t) - g(c))]$ oscillates rapidly for $t \neq c$. This leads of cancellation everywhere except in small regions $c \pm \delta c$. Therefore,

$$I(\lambda) \approx \exp [i\lambda g(c)] \int_{c-\delta c}^{c+\delta c} f(t) \exp [i\lambda(g(t) - g(c))] dt, \quad (7.3.6)$$

$$\approx f(c) \exp [i\lambda g(c)] \int_{-\infty}^{\infty} f(t) \exp \left[\frac{i\lambda}{2} g''(c)(t - c)^2 \right] dt. \quad (7.3.7)$$

This is the form of a known integral. After some algebraic steps the leading order of this integral becomes,

$$I(\lambda) \approx f(c) \exp [i\lambda g(c)] \sqrt{\frac{2\pi}{\lambda |g''(c)|}} \exp \left(\frac{i\pi\mu}{4} \right). \quad (7.3.8)$$

The reason why this method is called the stationary phase approximation is because the main contribution to this integral is from a region about c at which $g(t)$ is stationary. Further details on the stationary phase approximation can be found in [58, 180–183]. Figure 7.2 shows an example of a slow oscillating function $g(x)$ and fast oscillating function $f(x)$ about a stationary point.

The Bessel function of the first type has the form,

$$J_n(\lambda) = \int_0^1 \cos(n\pi t - \lambda \sin(\pi t)) dt, \quad (7.3.9)$$

$$= \Re \left[\int_0^1 \exp(n\pi i t) \exp(-i\lambda \sin(\pi t)) dt \right]. \quad (7.3.10)$$

Within interval $[0, 1]$, $g(t) = -\sin(\pi t)$ is stationary at $c = 1/2$, with $g(c) = -1$, $g''(c) = \pi^2$, $\mu = 1$. We set $f(t) = \exp(n\pi i t)$ and $f(c) = \exp(n\pi i/2)$. Now the leading order becomes,

$$J_n(\lambda \gg 1) \approx \Re \left[\exp\left(\frac{n\pi i}{2}\right) \exp(-i\lambda) \exp\left(\frac{i\pi}{4}\right) \sqrt{\frac{2}{\pi\lambda}} \right], \quad (7.3.11)$$

$$= \sqrt{\frac{2}{\pi\lambda}} \cos\left(\lambda - \frac{n\pi}{2} - \frac{\pi}{4}\right). \quad (7.3.12)$$

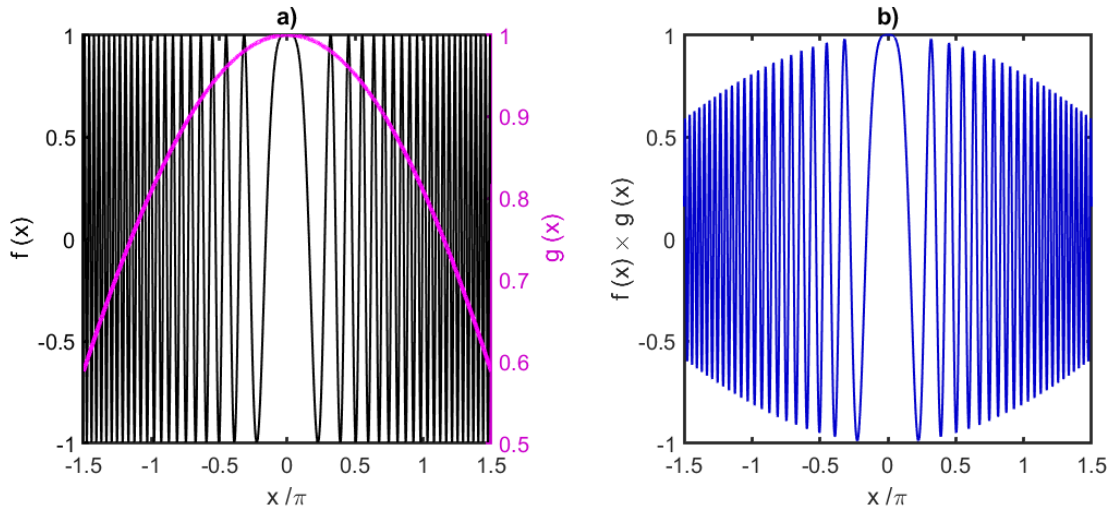


Figure 7.2: Stationary phase approximation example for very slowly oscillating $g(x)$ and quickly oscillating $f(x)$. $d(f(x)g(x)) / d(x) \approx 0$ about $x = 0$.

$$f(x) = \text{Re}\{\exp[2\pi i x^2]\}, g(x) = \cos(x/5).$$

Bibliography

- [1] Dubey A.K. and Yadava V. Laser beam machining - a review. *International Journal of Machine Tools and Manufacture*, 48(6):609–628, 2008.
- [2] Riker J.F. Active tracking lasers for precision target stabilization. *Laser Systems Technology*, 2003.
- [3] Galloway B.R. *High-Order Harmonic Generation Driven by Mid-Infrared Laser Light*. PhD Thesis: University of Colorado, 2017.
- [4] Bastawrous A. et al. Laser refractive eye surgery. *BMJ*, page DOI:10.1136/bmj.d2345, 2011.
- [5] Ursescu D. et al. Extreme light infrastructure – nuclear physics. a new research infrastructure at the interface of laser and subatomic physics. *Laser review*, 42(2):123–126, 2014.
- [6] Maiman T. Simulated optical radiation in ruby. *Nature*, 187(6):493–494, 1960.
- [7] Townes C. The first laser. press.uchicago.edu/Misc/Chicago/284158_townes.html, Accessed 1st Oct 2021.
- [8] Thyagarajan K. *Lasers, fundamentals and applications*. Springer, ISBN: 9781441964410, 2010.
- [9] Optics. Laser 2017: photonics now worth £12.9bn to UK economy. optics.org/news/8/6/39, Accessed 1st Oct 2021.
- [10] Peng Q. et al. Lasers in medicine. *Reports on Progress in Physics*, 71(5):DOI: doi:10.1088/0034-4885/71/5/056701, 2008.
- [11] Stanford magazine. The man who stopped time. stanfordmag.org/contents/the-man-who-stopped-time, Accessed 1st Sep 2021.

-
- [12] Harvey A. *Electron re-scattering from aligned linear molecules using the R-matrix method*. PhD Thesis: University College London, 2010.
- [13] McClung F. and Hellwarth R.W. Giant optical pulsations from ruby. *Journal of applied physics*, 33(3):828–829, 1962.
- [14] RP Photonics Encyclopedia. Q switching. www.rp-photonics.com/q-switching.html, Accessed 7th Mar 2021.
- [15] Orfanos I. Attosecond pulse metrology. *APL Photonics*, 4(8), 2019.
- [16] Calvert J.E. *Ionisation of metastable neon with few cycle laser pulses*. PhD Thesis: University of Griffith, 2016.
- [17] Willis E. et al. Theory of an optical maser. *Physical review*, 134(6):1429, 1964.
- [18] Hargrove L. Locking of he–ne laser modes induced by synchronous intracavity modulation. *Applied physics letters*, 5(1):4–5, 1964.
- [19] Cheriaux G. et al. Aberration-free stretcher design for ultrashort-pulse amplification. *Optics letters*, 21(6):414–416, 1996.
- [20] Fork R.L. et al. Negative dispersion using pairs of prisms. *Optics letters*, 9(5):150–152, 1984.
- [21] Lage E.W.. *Study of high-order harmonic generation effects under variations of focusing conditions of few cycle laser pulses*. PhD Thesis: Universidad de Salamanca, 2016.
- [22] Yakovelv I.V. Stretchers and compressors for ultra-high power laser systems. *Quantum electronics*, 44(5):393–414, 2014.
- [23] Zeitoun P. et al. X-ray chirped pulse amplification: Towards GW soft X-ray lasers. *Applied Sciences*, 3(3):581–592, 2013.
- [24] Levesque J. and Corkum P. Attosecond science and technology. *Canadian Journal of Physics*, 84(1):1–18, 2006.

-
- [25] Hentschel M. et al. Attosecond metrology. *Nature*, 414:509–513, 2001.
- [26] Robinson T. *Quasi-Phase-Matching of High-Harmonic Generation*. PhD Thesis, University of Oxford, 2009.
- [27] Siegman A.E. *Lasers*. University Science Books, ISBN: 0-935702-11-5, 1986.
- [28] Burnett N. et al. Harmonic generation in CO₂ laser target interaction. *Applied Physics Letters*, 31(3):172–174, 1977.
- [29] Corkum P.b. Plasma perspective on strong-field multiphoton ionization. *Physical Review Letters*, 71(13):1994–1997, 1993.
- [30] Kulander C. et al. High-order harmonic generation from atoms and ions in the high intensity regime. *Physical Review Letters*, 68(24):3535–3538, 1992.
- [31] Schultz T. and Vrakking M. *Attosecond and XUV Physics : Ultrafast Dynamics and Spectroscopy*. Wiley Sons, 2014.
- [32] Calegari F. et al. Advances in attosecond science. *Journal of Physics B: Atomic, Molecular and Optical Physics*, 49(6), 2016.
- [33] Nisoli M. et al. Attosecond electron dynamics in molecules. *Chemical reviews*, 117(16):10760–10825, 2017.
- [34] Tobey R. et al. Ultrafast extreme ultraviolet holography: dynamic monitoring of surface deformation. *Optics Letters*, 32(3):286–288, 2007.
- [35] Addanki S. et al. Review of optical fibers-introduction and applications in fiber lasers. *Results in Physics*, 10:743–750, 2018.
- [36] Mitchell K.J. *Laser beam shaping : properties and applications*. PhD Thesis: University Griffith, 2020.
- [37] Ashkin A. Optical trapping and manipulation of neutral particles using lasers. *Proceedings of the national academy of sciences of the United States of America*, 94(10):4853–4860, 1997.

-
- [38] Ashkin A. et al. Observation of a single-beam gradient force optical trap for dielectric particles. *Optics letters*, 11(5):196–198, 1986.
- [39] Chu S. Arthur ashkin (1922–2020). *Nature*, 588:29, 2020.
- [40] Lundh O. Control of laser focusing using a deformable mirror and a genetic algorithm. *Lund Reports on Atomic Physics*, pages Thesis, Lund University, 2003.
- [41] Sun L. et al. Intracavity deformable mirror for beam quality improvement and power enhancement of a passively q-switched laser. *Optics Express*, 26(7), 2018.
- [42] Frassetto S. et al. Optimization of low-order harmonic generation by exploitation of a resistive deformable mirror. *Applied Physics B: Lasers and Optics*, 106:905–909, 2012.
- [43] Yang P. et al. Adaptive laser beam shaping using a genetic algorithm. *Chinese Optics Letters*, 5(9):2906–2910, 2007.
- [44] El-Agmy R. et al. Adaptive beam profile control using a simulated annealing algorithm. *Optics Express*, 13(16):6085–6091, 2005.
- [45] Villorosi P. et al. Optimization of high-order harmonic generation by adaptive control of a sub-10-fs pulse wave front. *Optics Letters*, 29(2):207–209, 2004.
- [46] Bonora S. et al. Optimization of low-order harmonic generation by exploitation of a resistive deformable mirror. *Appl Phys B*, pages 106(905–909), 2011.
- [47] Gkortsas V. M. et al. Interplay of multiphoton and tunneling ionization in short-wavelength-driven high-order harmonic generation. *Physical review A - atomic, molecular, and optical physics*, 84(1), 2011.
- [48] Treacher D. *XUV lensless imaging with spatially shaped high-harmonic beams*. PhD Thesis: University of Oxford, 2019.

-
- [49] Constant E. et al. Spatial shaping of intense femtosecond beams for the generation of high-energy attosecond pulses. *Journal of Physics B: Atomic, Molecular and Optical Physics*, 45(7), 2012.
- [50] Treacher D. et al. Increasing the brightness of harmonic XUV radiation with spatially-tailored driver beams. *Journal of optics*, 23(1), 2020.
- [51] Hoffnagle J. Jefferson C. Design and performance of a refractive optical system that converts a gaussian to a flattop beam. *Applied Optics*, 39(30):5488–5499, 2000.
- [52] Gillen-Christandl K. et al. Comparison of gaussian and super gaussian laser beams for addressing atomic qubits. *Applied Physics B: Lasers and Optics*, 122(5):122–131, 2016.
- [53] ISO International Organisation for Standardization. Optics and photonics — lasers and laser-related equipment — test methods for laser beam power (energy) density distribution, ©2018. <https://www.iso.org/obp/ui/#iso:std:iso:13694:ed-3:v1:en>, Accessed 31st January 2020.
- [54] Siegman A.E. How to (maybe) measure laser beam quality: Tutorial presented at optical society of america annual meeting, long beach, california, 1997. <http://citeseerx.ist.psu.edu/viewdoc/download?doi=10.1.1.177.3400&rep=rep1&type=pdf>, Accessed 31st January 2020.
- [55] Evaluation of measurement data — guide to the expression of uncertainty in measurement. *International organization for standardization*, 2008.
- [56] Mekid S. Vaja D. Propagation of uncertainty: Expressions of second and third order uncertainty with third and fourth moments. *Measurement: Journal of the international measurement confederation*, 41(6):600–609, 2008.
- [57] Alda J. Laser and gaussian beam propagation and transformtion. *Encyclopedia of optical engineering*, pages 999–2013, 2003.

-
- [58] Goodman J.W. *Introduction to Fourier optics third edition*. W.H. Freeman, ISBN: 9780974707723, 2005.
- [59] Voelz D. *Computational Fourier optics, a MATLAB tutorial*. SPIE, ISBN: 9780819482044, 2011.
- [60] Poon T. Liu J. *Introduction to modern digital holography with matlab*. Cambridge university press, ISBN: 978-1-107-01670-5, 2014.
- [61] Hansen E.W. Fast hankel transform algorithm. *IEEE*, 33(3):666–671, 1985.
- [62] Bor Z. Distortion of femtosecond laser pulses in lenses and lens systems. *Journal of modern optics*, 35(12):1907–1918, 1988.
- [63] Ibragimov I. Focusing of ultrashort laser pulses by the combination of diffractive and refractive elements. *Optical society of America*, 34(11):7280–7285, 1995.
- [64] Kuo C.H. Sonic crystal lenses that obey the lensmaker’s formula. *Journal of physics D: applied physics*, 37(15):2155–2159, 2004.
- [65] Born M. and Wolf E. *Principles of optics sixth edition*. Pergamon press, 1980.
- [66] Sun B. et al. Pulse front adaptive optics: a new method for control of ultrashort laser pulses. *Optics express*, 23(15):19348–19357, 2015.
- [67] Midorikawa K. High-order harmonic generation and attosecond science. *Japanese journal of applied physics*, 50(9), 2011.
- [68] Keldysh L.V. et al. Ionization in the field of a strong electromagnetic wave. *Soviet Physics JETP*, 20:1307–1314, 1965.
- [69] Haessler S. et al. Self-probing of molecules with high harmonic generation. *Journal of physics B: atomic, molecular and optical physics*, 44(20):249–264, 2011.

-
- [70] Amini K. et al. Symphony on strong field approximation. *Reports on Progress in Physics*, 82(1):DOI: doi.org/10.1088/1361-6633/ab2bb1, 2018.
- [71] Dashcasan M. and Barati E. Coherent contribution of consecutive electron rescatterings in the extreme ultraviolet supercontinuum. *Physical review A - atomic, molecular, and optical physics*, 89(4), 2014.
- [72] Shan B. et al. High-order harmonic cutoff extension of the O₂ molecule due to ionization suppression. *Physical review A - atomic, molecular, and optical physics*, 66(6), 2002.
- [73] Spielmann C. et al. Near-key coherent X-ray generation with sub-10-fs lasers. *IEEE journal on selected topics in quantum electronics*, 4(2):249–264, 1998.
- [74] Shiner A. D. et al. High harmonic cutoff energy scaling and laser intensity measurement with a 1.8 μ m laser source. *Journal of modern optics*, 60(17):1458–1465, 2013.
- [75] Catoire F. et al. Complex structure of spatially resolved high-order-harmonic spectra. *Physical Review A*, 94(6), 2016.
- [76] Constant E. et al. Optimizing high harmonic generation in absorbing gases: Model and experiment. *Physical Review Letters*, 82(8):1668–1671, 1999.
- [77] Zabinsky Z. et al. Random search algorithms. *Wiley Encyclopedia of Operations Research and Management Science*, page DOI: 10.1002/9780470400531.eorms0704, 2011.
- [78] Schrack G. et al. An experimental comparison of three random searches. *Numerical methods for linear optimisation*, pages 137–147, 1972.
- [79] Zabinsky Z. et al. Improving hit-and-run for global optimisation. *Journal of global optimisation*, 3(2):171–192, 1993.
- [80] Mehta P. et al. A high-bias, low-variance introduction to machine learning for physicists. (arXiv:1803.08823v2):13–18, 2019.

-
- [81] Yang X.S. *Optimization and metaheuristic algorithms in engineering*. Chapter 1. DOI: 10.1016/B978-0-12-398296-4.00001-5, 2013.
- [82] James K. et al. *Swarm Intelligence*. Morgan Kaufmann publishers, ISBN: 1558605959, 2001.
- [83] Kennedy J. et al. Particle swarm optimization. (DOI: 10.1002/9780470612163):1942–1949, 2010.
- [84] Zhang Y. et al. New advances in machine learning. (DOI: 10.5772/225), 2012.
- [85] RF Wireless World. Advantages of deep learning, disadvantages of deep learning. www.rfwireless-world.com/Terminology/Advantages-and-Disadvantages-of-Deep-Learning.html, Accessed 15nd Jun 2021.
- [86] Coley D.A. *An Introduction to Genetic Algorithms for Scientists and Engineers*. World Scientific Publishing Co. Pte. Ltd, Singapore, 1999.
- [87] Dianati M. et al. An introduction to genetic algorithms and evolution strategies. <https://citeseerx.ist.psu.edu/viewdoc/download?doi=10.1.1.92.6910&rep=rep1&type=pdf>, Accessed 7th May 2021.
- [88] Senaratna N. Genetic algorithms: The crossover-mutation debate. 2005.
- [89] Goldberg D. Genetic algorithms in search optimization and machine learning. 1988.
- [90] Whitley D. A genetic algorithm tutorial. *Statistics and Computing*, 4, 10 1998.
- [91] Eglese R.W. Simulated annealing: A tool for operational research. *European Journal of Operational Research*, 46(3):271–281, 1990.
- [92] Kirkpatrick S. et al. Optimization by simulated annealing. *Science*, 220(4598):671–680, 1983.

-
- [93] Henderson D. et al. *Handbook of Metaheuristics, Chapter 10, The Theory and Practice of Simulated Annealing*. Springer, Boston, MA, Kluwer Academic Publishers, ISBN: 978-1-4020-7263-5, 2003.
- [94] Cerny V. Thermodynamical approach to the traveling salesman problem: An efficient simulation algorithm. *Journal of optimized theory and applications*, 45(1):41–51, 1985.
- [95] Aarts E. et al. *Simulated Annealing and Boltzmann Machines: A Stochastic Approach to Combinatorial Optimization and Neural Computing*. Wiley Series in Discrete Mathematics and Optimization, 1991.
- [96] Oysu C. et al. Application of heuristic and hybrid-GASA algorithms to tool-path optimization problem for minimizing airtime during machining. *Engineering Applications of Artificial Intelligence*, 22(3):389–396, 2009.
- [97] Alfarisy G. et al. Hybrid genetic algorithm and simulated annealing for function optimization. *Journal of Information Technology and Computer Science*, 1(2):81–97, 2017.
- [98] Babcock H.W. et al. The possibility of compensating astronomical seeing. *Astronomical Society of the Pacific*, 65(386):229–236, 1953.
- [99] Madec P.Y. et al. Overview of deformable mirror technologies for adaptive optics and astronomy. *Adaptive Optics Systems 3 - International Society for Optics and Photonics*, find volume, 2012.
- [100] RP Photonics. Deformable mirrors. https://www.rp-photonics.com/deformable_mirrors.html, Accessed 22nd Jan 2021.
- [101] Song H. et al. Model-based aberration correction in a closed-loop wavefront-sensor-less adaptive optics system. *Optical Society of America*, 18(23), 2010.
- [102] Bonora S. et al. Design of deformable mirrors for high power lasers. *High Power Laser Science and Engineering*, 4(16):DOI:10.1017/hpl.2016.14, 2016.

-
- [103] Bonora S. et al. Innovative membrane deformable mirrors. *Topics in Adaptive Optics*, page 231, 2012.
- [104] ONI. Storm microscopy. <https://oni.bio/storm-microscopy/>, Accessed 22nd Jan 2021.
- [105] Nikon Instruments. Single-molecule super-resolution imaging. <https://www.microscopyu.com/techniques/super-resolution/single-molecule-super-resolution-imaging>, Accessed 22nd Jan 2021.
- [106] Tehrani K.F. et al. Adaptive optics stochastic optical reconstruction microscopy (AO-STORM) by particle swarm optimization. *Biomedical Optics Express*, 8(11), 2017.
- [107] Bonora S. et al. Ultrabroadband pulse shaping with a push-pull deformable mirror. *Optics Express*, 18(22):23147–23152, 2010.
- [108] Treacy E.B. Optical pulse compression with diffraction gratings. *IEEE Journal of Quantum Electronics*, 5(9):454, 1969.
- [109] Fork R.L. et al. Negative dispersion using pairs of prisms. *Optics Letters*, 9(5):150, 1984.
- [110] Zeek E. et al. Pulse compression by use of deformable mirrors. *Optics Letters*, 24(7):493–495, 1999.
- [111] Farfan C.A. et al. Femtosecond pulse compression using a neural-network algorithm. *Optics Letters*, 43(20):5166–5169, 2018.
- [112] Bartels R. et al. Attosecond time-scale feedback control of coherent X-ray generation. *Chemical Physics*, 267:277–289, 2000.
- [113] Bartels R. et al. Shaped-pulse optimization of coherent emission of high-harmonic soft X-rays. *Letters to Nature*, 406:164–166, 2000.

-
- [114] Matsui F. et al. Genetic-algorithm-based method to optimize spatial profile utilizing characteristics of electrostatic actuator deformable mirror. *Optical Review*, 15(3):156–161, 2008.
- [115] Frazier B.W Tyson R.K. *Field Guide to Adaptive Optics, Second Edition*. SPIE Press, Washington USA, ISBN: 9781439808597, 1991.
- [116] Fayyaz Z. et al. A comparative study of optimization algorithms for wavefront shaping. *Journal of innovative optical health sciences*, 12(4), 2019.
- [117] Jullien A. Spatial light modulators. <https://hal.archives-ouvertes.fr/hal-02558771>, Accessed 21st May 2021.
- [118] HOLOEYE. Spatial light modulators. <https://holoeye.com/spatial-light-modulators/>, Accessed 21st May 2021.
- [119] Andrienko D. Introduction to liquid crystals. *Journal of molecular liquids*, 267(1):520–541, 2018.
- [120] Beeckman J. et al. Liquid-crystal photonic applications. *Optical engineering*, 50(8), 2011.
- [121] Jullien A. Spatial light modulators. www.photoniques.com/articles/photon/pdf/2020/02/photon2020101p59.pdf, Accessed 4th Dec 2021.
- [122] Zhao Z. An interferometric method for local phase modulation calibration of LC-SLM using self-generated phase grating. *Review of scientific instruments*, 89(8), 2018.
- [123] Love G. Wave-front correction and production of zernike modes with a liquid-crystal spatial light modulator. *Applied optics*, 36(7):1517–1524, 1997.
- [124] Thunnissen R.T. Beam steering with spatial light modulators: Quantisation effects. dipotit.ub.edu/dspace/bitstream/2445/59950/1/TFG-Ribot-Thunnissen-Astrid.pdf, Accessed 6th Nov 2021.

-
- [125] Lenton I. et al. Optical tweezers exploring neuroscience. *Frontiers in Bioengineering and Biotechnology*, page DOI: doi.org/10.3389/fbioe.2020.602797, 2020.
- [126] Greulich K.O. Manipulation of cells with laser microbeam scissors and optical tweezers: a review. *Reports on Progress in Physics*, 80(2):DOI: doi:10.1088/1361-6633/80/2/026601, 2016.
- [127] Bowman R. An SLM-based shack-hartmann wavefront sensor for aberration correction in optical tweezers. *Journal of optics*, 12:DOI: 10.1088/2040-8978/12/12/124004, 2010.
- [128] Wulff K. Aberration correction in holographic optical tweezers. *Optics express*, 14(9):4169–4174, 2006.
- [129] Eriksen R. Fully dynamic multiple-beam optical tweezers. *Optics express*, 10(14):597–602, 2002.
- [130] Kuga T. et al. Novel optical trap of atoms with a doughnut beam. *Physical review letters*, 78(25):4713–4716, 1997.
- [131] Liu Z. et al. Generation of hollow gaussian beams by spatial filtering. *Optics letters*, 32(15):2076–2078, 2007.
- [132] Lee K. et al. Atom guiding and cooling by a dark hollow laser beam. *The American physical society*, 3(1):509–513, 1999.
- [133] Yongming N. et al. Hollow gaussian beam generated by beam shaping with phase-only liquid crystal spatial light modulator. *Optics and laser technology*, 44(2):384–389, 2012.
- [134] Narupon C. et al. Generation of non-diffracting bessel beams by use of a spatial light modulator. *Optics letters*, 28(22):2183–2185, 2003.

-
- [135] ALPAO. Datasheet: high-speed deformable mirrors. http://yiqi-oss.oss-cn-hangzhou.aliyuncs.com/aliyun/900102831/technical_file/file_545283.pdf, Accessed 25th May 2021.
- [136] Weiner A. Femtosecond pulse shaping using spatial light modulators. *Review of scientific instruments*, 71(5):1929–1960, 2000.
- [137] Treacher D. et al. Optimised XUV holography using spatially shaped high harmonic beams. *Optics express*, 27(20):29016–29025, 2019.
- [138] Eyring S. et al. Improving high-order harmonic yield using wavefront-controlled ultrashort laser pulses. *Optics express*, 20(5):5061–5066, 2012.
- [139] Walter D. et al. Adaptive spatial control of fiber modes and their excitation for high-harmonic generation. *Optics express*, 14(8):3433–3442, 2006.
- [140] MIT. The ideal thin lens as a fourier transform engine fresnel diffraction. <http://web.mit.edu/2.710/Fall106/2.710-wk10-a-s1.pdf>, Accessed 25th May 2021.
- [141] Tyson R. and Frazier B. *Field guide to adaptive optics second edition*. SPIE, ISBN:9781439808597, 2012.
- [142] Zawadzki R. et al. Performance of a 97-element ALPAO membrane magnetic deformable mirror in an adaptive optics - optical coherence tomography system for in vivo imaging of the human retina. *Photonics letters of Poland*, 3(4):147–149, 2011.
- [143] Lei X. et al. Double-deformable-mirror adaptive optics system for laser beam cleanup using blind optimization. *Optics express*, 20(20):22143–22157, 2012.
- [144] Mahajan V. Strehl ratio for primary aberrations in terms of their aberration variance. *Journal of the optical society of America*, 73(6):860–861, 1983.

-
- [145] Nei Y. et al. Ultrafast optical signal pulse descending time controlling with deformable mirror and spatial light modulators. *Journal of Physics: Conference series*, 679(1), 2016.
- [146] Kelly T. et al. Phase-aberration correction with dual liquid-crystal spatial light modulators. *Applied optics*, 37(22):5184–5189, 1998.
- [147] Ma H. Adaptive correction of vortex laser beam in a closed-loop system with phase only liquid crystal spatial light modulator. *Optics communications*, 285(6):859–863, 2012.
- [148] Ma H. Simultaneous adaptive control of dual deformable mirrors for full-field beam shaping with the improved stochastic parallel gradient descent algorithm. *Optics letters*, 38(3):326–328, 2013.
- [149] Ma H. et al. Adaptive conversion of multimode beam to near-diffraction-limited flattop beam based on dual-phase-only liquid-crystal spatial light modulators. *Optics express*, 18(26):27723–27730, 2010.
- [150] Ma H. et al. Adaptive generation of a near-diffraction-limited square flattop beam with dual phase only liquid crystal spatial light modulators. *Journal of optics*, 13, 2011.
- [151] Ma H. et al. Near-diffraction-limited annular flattop beam shaping with dual phase only liquid crystal spatial light modulators. *Optics express*, 18(8):8251–8260, 2010.
- [152] Ma H. et al. Generation of flat-top beam with phase-only liquid crystal spatial light modulators. *Journal of optics*, 12(4), 2010.
- [153] Gerchberg R.W. and Saxton W.O. A practical algorithm for the determination of phase from image and diffraction plane pictures. *Optik*, 35(2):237–246, 1972.

-
- [154] Sinclair G. et al. Interactive application in holographic optical tweezers of a multi-plane gerchberg-saxton algorithm for three-dimensional light shaping. *Optics Express*, 12(8):1665–1670, 2004.
- [155] Lloyd D. *Characterizing the Spatial Properties of High Harmonic Generation*. PhD Thesis: Oxford University, 2014.
- [156] Mehrabkhani S. and Küster M. Optimization of phase retrieval in the fresnel domain by the modified gerchberg-saxton algorithm. arxiv.org/ftp/arxiv/papers/1711/1711.01176.pdf, Accessed 2nd Nov 2021.
- [157] KSU. Atomic units. www.phys.ksu.edu/personal/cdlin/class/class11a-am02/atomic_units.pdf, Accessed 20th September 2021.
- [158] NIST. Fundamental physics constants. physics.nist.gov/cgi-bin/cuu/Results?search_for=atomic+units, Accessed 20th September 2021.
- [159] Lewenstein M. et al. Theory of high-harmonic generation by low-frequency laser fields. *Phys. Rev. A*, 49:2117–2132, 1994.
- [160] Lewenstein M. et al. Phase of the atomic polarization in high-order harmonic generation. *Phys. Rev. A*, 52(6):4747–4754, 1995.
- [161] Lewenstein M. et al. Theory of high-order harmonic generation by an elliptically polarized laser field. *Phys. Rev. A*, 53(3):1725–1745, 1995.
- [162] Hawkins P. *High harmonic generation in periodic systems*. PhD Thesis, Imperial College London, 2016.
- [163] Lytle A. *Phase patching and coherence of high-order harmonic generation in hollow waveguides*. PhD Thesis, University of Colorado, 2001.
- [164] Jin C. *Theory of nonlinear propagation of high harmonics generated in a gaseous medium*. PhD Thesis, University of Kansas State University, 2012.

-
- [165] Holzner K. *High harmonic generation from combined femtosecond laser fields*. PhD Thesis, Imperial College London, 2017.
- [166] Ivanov M. and Smirnova O. Ionization in strong low-frequency fields: from quantum s-matrix to classical pictures. <https://www.pks.mpg.de/~corinf12/lectures/ivanov.pdf>, Accessed 1st October 2021.
- [167] Ammosov M.V. et al. Tunnel ionization of complex atoms and of atomic ions in an alternating electromagnetic field. *Soviet Physics - JETP*, 64(6):1191–1194, 1986.
- [168] Schafer K. et al. High harmonic generation from ultrafast pump lasers. *Physical Review Letters*, 78(4):638–641, 1996.
- [169] Abanador P. et al. Wavelength and intensity dependence of recollision-enhanced multielectron effects in high-order harmonic generation. *Physical Review A*, 97(4), 2018.
- [170] Quintard L. et al. Optics-less focusing of XUV high-order harmonics. *Science Advances*, 2019.
- [171] Chang K.Y. et al. High-order nonlinear dipole response characterized by extreme ultraviolet ellipsometry. *Optica*, 8(4):484–492, 2021.
- [172] Mang M. et al. Spatially resolved common-path high-orderharmonic interferometry. *Optics Letters*, 43(21):5275–5278, 2018.
- [173] NIST. Nist atomic spectra database ionization energies form. physics.nist.gov/PhysRefData/ASD/ionEnergy.html, Accessed 1st Oct 2021.
- [174] Sandberg R. *Closing the Gap to the Diffraction Limit: Near Wavelength Limited Tabletop Soft X-Ray Coherent Diffractive Imaging*. PhD Thesis: University of Colorado, 2009.
- [175] Hecht E. *Optics Fifth Edition*. Pearson Education, ISBN:9780133977226, 2017.

-
- [176] Yan A. et al. Predicting visibility of interference fringes in X-ray grating interferometry. *Optics Express*, 24(14):15927–15939, 2016.
- [177] Greivenkamp J. E. Interference. www.hep.manchester.ac.uk/u/xiaguo/waveoptics/Interference_supplement.pdf, Accessed 5th Jan 2022.
- [178] Wyant J. C. Coherence. wp.optics.arizona.edu/jcwyant/wp-content/uploads/sites/13/2016/08/3Coherence.pdf, Accessed 5th Jan 2022.
- [179] Fricker P. Zernike polynomials. www.mathworks.com/matlabcentral/fileexchange/7687-zernike-polynomials, Accessed 4th Aug 2021.
- [180] Department of mathematics University of Nebraska. Integral asymptotics 3: Stationary phase. www.math.unl.edu/~scohn1/8423/intasym4.pdf, Accessed 5th Aug 2021.
- [181] Marenduzzo D. Section 5: The saddle-point method a.k.a. ‘method of steepest descents’. www2.ph.ed.ac.uk/~dmarendu/MOMP/lecture05.pdf, Accessed 5th Aug 2021.
- [182] Weber H.J. Arfken G.B. *Mathematical methods for physicists, 5th edition*. Academic press, ISBN: 0-12-059826-4, 2001.
- [183] Nayak A. et al. Saddle point approaches in strong field physics and generation of attosecond pulses. *Physics reports*, 833:1–52, 2019.